# REPORT DOCUMENTATION PAGE

| 1. Recipient's Reference | 2. Originator's Reference | 3. Further Reference | 4. Security Classification of Document |
|---|---|---|---|
| | AGARD-AG-302 | ISBN 92-835-0438-0 | UNCLASSIFIED |

**5. Originator**  Advisory Group for Aerospace Research and Development
North Atlantic Treaty Organization
7 rue Ancelle, 92200 Neuilly sur Seine, France

**6. Title**  TECHNIQUES OF FLOW VISUALIZATION

**7. Presented at**

| 8. Author(s)/Editor(s) | 9. Date |
|---|---|
| By W.Merzkirch — Edited by K.Gersten | December 1987 |

| 10. Author's/Editor's Address | 11. Pages |
|---|---|
| See flyleaf. | 98 |

**12. Distribution Statement**   This document is distributed in accordance with AGARD policies and regulations, which are outlined on the Outside Back Covers of all AGARD publications.

**13. Keywords/Descriptors**

Flow visualization          Propulsion
Wind tunnels                Evaluation
Water flow

**14. Abstract**

The techniques of flow visualization and their application in wind tunnels, water channels, and experiments related to propulsion research are reviewed. These techniques can be classified roughly into three major groups: Surface flow visualization, scattering from flow tracers, and density sensitive flow visualization. The progress in laser optics and the wide-spread use of computers has led to the development of novel techniques and evaluation procedures, which are included in the review; e.g. laser-induced fluorescence, speckle photography, image processing, and optical tomography. Emphasis is given to the discussion of the physical background of the methods. Information on technical details is provided by means of a number of sample photographs and by respective references.

This AGARDograph has been produced at the request of the Fluid Dynamics Panel of AGARD.

AGARD-AG-302

# AGARD

## ADVISORY GROUP FOR AEROSPACE RESEARCH & DEVELOPMENT

### 7 RUE ANCELLE  92200  NEUILLY SUR SEINE  FRANCE

AGARDograph No.302

# Techniques of Flow
# Visualization

## NORTH  ATLANTIC  TREATY  ORGANIZATION

**DISTRIBUTION AND AVAILABILITY
ON BACK COVER**

NORTH ATLANTIC TREATY ORGANIZATION

ADVISORY GROUP FOR AEROSPACE RESEARCH AND DEVELOPMENT, Paris .

(ORGANISATION DU TRAITE DE L'ATLANTIQUE NORD)

AGARDograph No.302

## TECHNIQUES OF FLOW VISUALIZATION

by

W.Merzkirch
Universität Essen
Postfach 103764
4300 Essen 1
Federal Republic of Germany

Edited by

K.Gersten
Institut für Thermo und Fluiddynamik
Ruhr-Universität Bochum
Postfach 10 21 48
D-4630 Bochum 1
Federal Republic of Germany

December 1987

# THE MISSION OF AGARD

According to its Charter, the mission of AGARD is to bring together the leading personalities of the NATO nations in the fields of science and technology relating to aerospace for the following purposes:

— Recommending effective ways for the member nations to use their research and development capabilities for the common benefit of the NATO community;

— Providing scientific and technical advice and assistance to the Military Committee in the field of aerospace research and development (with particular regard to its military application);

— Continuously stimulating advances in the aerospace sciences relevant to strengthening the common defence posture;

— Improving the co-operation among member nations in aerospace research and development;

— Exchange of scientific and technical information;

— Providing assistance to member nations for the purpose of increasing their scientific and technical potential;

— Rendering scientific and technical assistance, as requested, to other NATO bodies and to member nations in connection with research and development problems in the aerospace field.

The highest authority within AGARD is the National Delegates Board consisting of officially appointed senior representatives from each member nation. The mission of AGARD is carried out through the Panels which are composed of experts appointed by the National Delegates, the Consultant and Exchange Programme and the Aerospace Applications Studies Programme. The results of AGARD work are reported to the member nations and the NATO Authorities through the AGARD series of publications of which this is one.

Participation in AGARD activities is by invitation only and is normally limited to citizens of the NATO nations.

The content of this publication has been reproduced
directly from material supplied by AGARD or the authors.

Published December 1987

Copyright © AGARD 1987
All Rights Reserved

ISBN 92-835-0438-0

SPS

*Printed by Specialised Printing Services Limited*
*40 Chigwell Lane, Loughton, Essex IG10 3TZ*

# PREFACE

Reviews of experimental techniques are necessary from time to time due to the rapid development of the hardware and software of the respective methods. Flow visualization is an important diagnostic tool for wind tunnels, water tunnels, and other facilities, since it provides an over-all view of the flow in a whole field, sometimes even allowing for taking quantitative data. Flow visualization has had a considerable benefit from the development of laser optics and computational methods. This development is reviewed together with a presentation of the physical background of the existing, sometimes "classical" methods and principles. Very essential in such a review is the presentation of examples. I am grateful to all authors and institutions who have provided sample photographs to this report and thereby helped to facilitate the understanding of the particular techniques. I am also thankful to Mrs H.Müller who has typed the manuscript.

Essen, May 1987
W.Merzkirch

\*  \*  \*

Les matériels et logiciels auxquels font appel les techniques expérimentales évoluent à un rythme tel qu'il est indispensable de faire périodiquement le point de la situation. Que ce soit en soufflerie aérodynamique ou hydraulique, ou toute autre installation similaire, la visualisation des écoulements constitue un outil essentiel de diagnostic car elle procure une vue globale d'un écoulement complet et permet même parfois de recueillir des données quantitatives.

Le développement de l'optique laser et des méthodes de calcul a grandement contribué à l'amélioration de la visualisation des écoulements. L'étude présentée porte sur ce développement et recense les fondements physiques des méthodes et principes existants, fussent-ils "classiques". Elle inclut nombre d'exemples sans lesquels elle ne saurait être complète, c'est pourquoi je remercie tous les auteurs et organismes dont les photographies illustrent cette étude et facilitent la compréhension des techniques particulières auxquelles elles se rapportent.

Essen, mai 1987
W.Merzkirch

# CONTENTS

# 1. INTRODUCTION

The role of flow visualization in experimental fluid-mechanical research has been appraised many times, and a number of reviews or comprehensive descriptions, either of the whole field or particular applications, are available; see, e.g., [1.1-1.8]. The development of new techniques and instruments make it necessary to revise the visualization methods from time to time. The majority of the recent technical developments in this area result from the progress made in laser optics and the wide-spread use of computers for analyzing experimental data. Laser-induced fluorescence, speckle photography, image processing, and optical tomography are examples of such modern developments.

The application of novel techniques can provide new insight into existing problems in fluid mechanics. As an example, two references are quoted which discuss the state of the art of research in turbulence: "Flow visualization ... appears to have found a kind of rebirth in recent years. ... Flow visualization is essential not only in obtaining a clear perception of the flow ... but also in planning sophisticated measurements. ... Still another facet of the second revolution (i.e.: in turbulence research) in which flow visualization plays the central role is image processing" [1.9], and: "It is ironical that coherent structures ..., the Brown-Roshko vortices, and longitudinal vortices in the sublayer of a turbulent boundary layer were all found by the most primitive of experimental methods, flow visualization" [1.10].

The latter reference brings up the question on what kind of information is available from a flow photograph, and how does this compare with data from different experimental sources. Again, this problem has been the subject of extensive discussions and reviews, and the situation may well be illustrated by quoting Hussain [1.9]: "Flow visualization presents excessive information but very little hard data, and hot-wires or LDAs give some hard data but very little flow physics".

This report reviews the methods of flow visualization with particular emphasis on their application in wind tunnels, water tunnels, and experiments related to propulsion research. The definition of a method to be included is that it provides a visual pattern of the flow in form of a whole-field record, e.g., a photograph. It will be shown that, in contrast to the references quoted previously, some of the newly developed techniques are not really primitive and involve complicated optical instruments, and they may even provide "hard data" on the flow field.

The subject of many flow studies is the interaction of a solid body with a fluid flow. Therefore, the discussion of methods starts with those that visualize the flow pattern on a solid surface. The following chapters deal with methods visualizing the whole field, either by introducing a foreign substance (smoke, dye) or by making use of refractive index changes in the flowing fluid (optical methods). Emphasis is placed on the discussion of the physical background of a method rather than on technical details. The latter may be found, e.g., in laboratory reports some of which are referred to in the cited bibliography of each chapter.

## References

1.1. Merzkirch, W.: Flow Visualization. New York, Academic Press, 1974.

1.2. Merzkirch, W.: Making fluid flows visible. American Scientist 67 (1979), 330-336.

1.3. Asanuma, T. (editor): Flow Visualization (Proceedings of the First International Symposium on Flow Visualization). Washington, Hemisphere, 1979.

1.4. Van Dyke, M. (editor): An Album of Fluid Motion. Stanford, Parabolic Press, 1982.

1.5.  Merzkirch, W. (editor):  Flow Visualization II. Washington, Hemisphere, 1982.

1.6.  Yang, W.J. (editor):  Flow Visualization III. Washington, Hemisphere, 1985.

1.7.  Mueller, T.J.:  The role of flow visualization in the study of afterbody and base flows. Exp. Fluids 3 (1985), 61-70.

1.8.  Settles, G.S.:  Modern developments in flow visualization. AIAA J. 24 (1986), 1313-1323.

1.9.  Hussain, A.K.M.F.:  Role of coherent structures in turbulent shear flows. Proc. Indian Acad. Sci. (Engng. Sci.) 4 (1981), 129-175.

1.10. Liepmann, H.W.:  The rise and fall of ideas in turbulence. American Scientist 67 (1979), 221-228.

## 2.   SURFACE FLOW PATTERNS

The rates of shear forces, pressure forces, and heating loads excerted by a fluid flow to the wall of a solid body are subject of many studies. Visualization of the flow pattern very close to or at the body surface can be helpful for such studies. Many methods of surface flow visualization are making use of a coating of the surface with a material that interacts with the flow and thereby produces a visible information. Depending on whether the interaction is mechanical, chemical, or thermal, information on the following quantities might be derived:

- wall pressure, skin friction, or simply flow direction;
- mass transfer to the wall;
- wall heat transfer or wall temperature.

In the following paragraphs, the methods for visualizing surface flow patterns will be discussed in the indicated order of sequence. The physical processes on which these methods depend: transfer of momentum, mass, and heat, are strongly influenced by the circumstances whether the flow is laminar or turbulent, attached or separated. Therefore, in the simplest way of their application, the methods just serve to detect the locations of transition, separation, or attachment.

### 2.1  OIL FILM VISUALIZATION

Since several decades of wind tunnel practice oil film visualization has become a standard wind tunnel technique. A number of reviews with many practical advices are available, e.g., Maltby [2.1] or Settles and Teng [2.2]. The surface of interest is coated with a thin layer of oil in which a finely powdered pigment is solved. When the wind tunnel is turned on, the oil is carried away with the air stream, and the dry pigment remains on the surface where it forms a streaky pattern indicating the direction of the flow close to the surface. Particular phenomena in the remaining pattern are attributed to flow separation from the surface or flow reattachment. A test model to which the mixture of oil and pigment was applied can be taken out of the test section, after the tunnel has been stopped, and the pattern on the model surface can be inspected outside the wind tunnel (Fig. 2.1).

Many instructions have been given in the literature on how to prepare an oil/pigment mixture appropriate for a specific test condition; e.g., [2.2] to [2.4]. A large amount of practical experience is collected and described in unpublished laboratory reports or manuals. The reader might find as many different recipees as he consults reports. The object is to prepare a mixture of such a consistency that it will run easily under the given test conditions and leave behind the desired streaks of the pigment. Ideally, the mixture should not begin to run until the selected wind speed is reached, and after an appropriate time of running, the pattern should be sufficiently dry to be unaffected by the unsteady air flow when the tunnel is stopped.
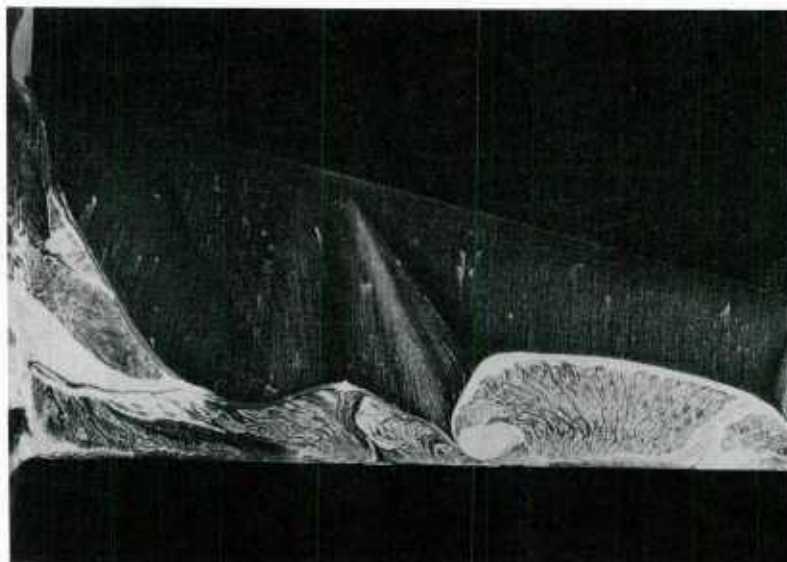
Fig. 2.1:  Oil film pattern on the upper surface of the right wing of an orbiter model
at M = 7.4 wind tunnel flow and 18° angle of attack. Attached flow in the
front part of the surface. Contour lines indicate the formation of a conical
trailing vortex and its interaction with the separated flow on the rear side
of the wing (NASA Ames Research Center, Moffett Field, CA).

From the latter it follows, that the lower the air velocity, the lower should be
the viscosity of the oil. Liquids, that have been used als solvents or carriers for the
pigment, are, in ascending order of viscosity: alcohol, kerosene, light Diesel oil,
light transformer oil. Viscosity and surface tension of these liquids can be adjusted by
additives. Two special situations for modern wind tunnel testing should be mentioned:
The low freestream pressures associated with high-speed wind tunnels are unfavorable for
using standard oils, because these oils are characterized by high vapor pressures; then,
vacuum-pump oil is the right choice. Propane ($C_3H_8$), which has a low melting point, has
been employed in a cryogenic wind tunnel [2.5] where the mentioned standard oils would
freeze.

The pigment in the mixture should provide a clear pattern against the model sur-
face as the background. A white powder like titanium dioxide ($TiO_2$) or china clay can
be used on a dark model (Fig. 2.2). Lampblack, a fine powder that mixes well with oil
is most suitable on a light model surface; see, e.g., Meznarsic and Gross [2.6], or
Sparrow and Comb [2.7]. The dispersion of the pigment in oil may be improved by adding
a few drops of oleic acid, see Keener [2.8]. Fluorescent pigments, when illuminated
with ultraviolet light, can provide a very brillant surface pattern; only the surface
pattern to be visualized is seen, whereas model and background remain invisible. This is
of particular interest if the model geometry is complex; see, e.g., Gessner  and Chan
[2.9].

The pigment pattern remaining on the model surface can be photographed for the pur-
pose of recording it. If the model surface is curved, a problem comes up in relating the
plane record of the curved surface pattern to a surface coordinate system. As a solution
to this problem, Sparrow and Comb [2.7] cover the model surface with white, plasticized,
self-adhering contact paper, and they apply the oil-pigment (lampblack) mixture to the
paper. After the visible pattern is formed, the paper is separated from the wall and
laid flat for being photographed. For the same purpose, i.e. for eliminating camera
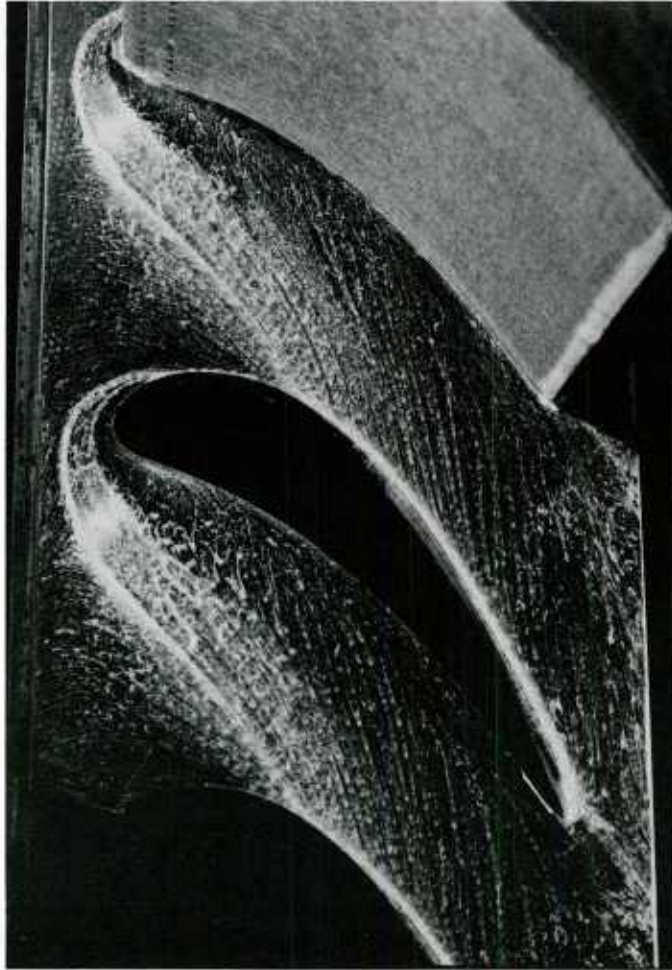
4



Fig. 2.2:  Oil film pattern on the plane side walls of a cascade wind tunnel at Mach
number M = 0.4 and with weak blowing at the front edge of the blades (DFVLR-
Institut für Antriebstechnik, Köln, F.R.Germany).

parallax when photographing the surface pattern, Settles and Teng [2.6] apply transparent adhesive tapes to the model after the wind tunnel experiment. The very thin coating of pigment remaining on the surface is lifted off and preserved for taking a record.

The interpretation of the observed pattern is, of course, strongly related to the question on how the pattern is formed. Several explanations have been given; but the problem has never been investigated systematically. It has been said that the fine particles of the pigment coagulate, and that the striations are caused by the wake behind such coagulations in the flowing oil film. Hornung [2.10] observed that the flowing oil film becomes unstable, breaks up to form droplets which, due to their large resistance, shoot at high speed across the oil film, thus producing the striations. Murai et al. [2.11] verified longitudinal instabilities in the thin oil film which could be responsible for the observed pattern.

Information on the accuracy of the oil film technique can be obtained if one analyzes the flow pattern in the oil film. The only available analysis has been developed by Squire [2.12]. He investigates the problem of how the air flow close to the wall is disturbed due to the presence of the oil film. The boundary conditions for the air flow now have to be fulfilled at the oil/air interface where the velocity of the two fluids

is the same and not zero. The velocity u at this interface is

$$u(y=h) = \frac{\mu_{air}}{\mu_{oil}} \cdot \left\{ - \frac{h^2}{2} \cdot \left( \frac{1}{\mu_{air}} \cdot \frac{dp}{dx} + h \cdot \left( \frac{\partial u_{air}}{\partial y} \right)_{y=h} \right) \right\} \quad , \tag{2.1}$$

where x is the streamwise coordinate in the plane of the wall, y is the coordinate normal to the wall, h is the oil film thickness, $\mu$ viscosity, and p pressure. Since the ratio $\mu_{air}/\mu_{oil}$ is of the order $10^{-2}$ to $10^{-4}$, u(y=h) is normally a very small quantity, i.e., the change in the conditions for the air flow can be neglected, with the exception of one situation, namely, when the pressure change in streamwise direction, dp/dx, becomes very large. This, however, is the case at the location of flow separation or attachment, particularly if the separation is enforced by a shock wave. Squire's analysis gives no information on how big the error in the measurement will be, e.g. in terms of the difference between the indicated and the real location of separation. But, since many oil film experiments are used for visualizing the positions of flow separation and attachment, Squire's results are a strong warning that such measurements must be carefully interpreted.

The applications of the oil film technique for aerodynamic testing are so numerous, that only a few references can be listed, which are representative for many others. Fow low-speed flows, see George [2.13]; high-speed configurations: Reding and Ericsson [2.14]; separation by shock impingement: Settles et al. [2.15].

## 2.2 OIL FILM SKIN FRICTION MEASUREMENTS

In various publications, e.g., [2.16-2.18], Tanner demonstrates that it is possible to relate the height of the oil film, h, to the skin friction or the wall shear stress of the air flow, $\tau_w$. Suppose that the oil has been deposited on the body surface in form of a small drop or along a straight line normal to the main flow direction. The air flow is started at time t = 0, the oil drop develops into a thin film whose thickness h varies with position x and time t according to (see Fig. 2.3)
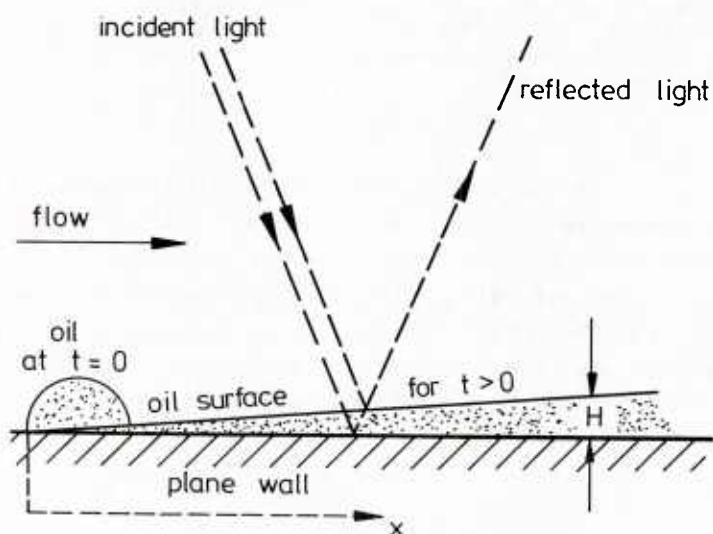


Fig. 2.3:
Measurement of the oil film thickness h at time t > 0 by means of optical interference of two reflected light rays (according to [2.16]).

6

$$h(x,t) = \frac{\mu_{oil}}{t \cdot \tau_w^{1/2}} \cdot \int_0^x \frac{dx}{\tau_w^{1/2}} \qquad . \qquad (2.2)$$

With known value of the viscosity of the oil, $\mu_{oil}$, it is possible to determine the skin friction $\tau_w$, once the oil film thickness can be measured. Since the film is very thin, Tanner measures h by interferometric means (Fig. 2.3). Interference is generated between light rays reflecting from the surface of the oil film and from the body surface, respectively. With the surface being plane and flat, it is possible to take an interferogram of the whole surface for one particular instant of time, $t_1 > 0$ (Fig. 2.4). The visible interference fringes are curves of equal height h, and the photograph includes information on the distribution of the wall shear stress, $\tau_w$, in the observed surface.
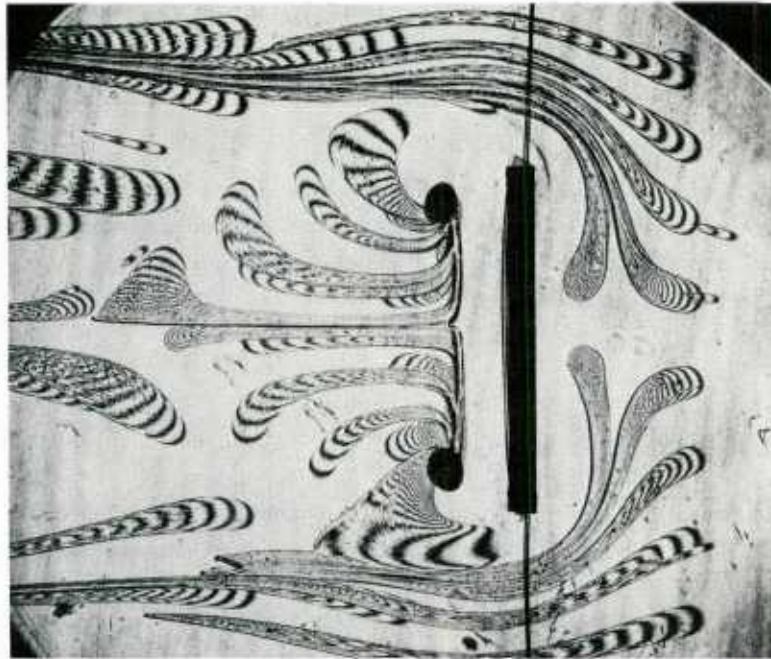


Fig. 2.4: Curves of equal height visualized by optical interferometry in the oil film traces that have developed from a number of oil drops on a plane surface (planview). Main flow direction of the air is from left to right. The air is forced to flow around a vertical wedge. The oil is collected in the center of two vortices behind the wedge, as indicated by the dark spots (L.H. Tanner, Brighton Polytechnic, England).

For the application to curved body surfaces, Tanner describes a modification, which no longer delivers information on a whole field, but measures the oil film thickness at a point and as a function of time. Two focused laser beams that are reflected from the solid surface and from the oil surface, respectively, interfere with oneanother, as indicated in Fig. 2.3. A photodiode records the interference, i.e., alternate bright and dark signals, according to the variation with time of the film thickness h at a given position x. Wall shear stress measurements have been performed with this "skin friction probe" in supersonic flow, [2.19,2.20].

## 2.3 WALL TUFTS

A relatively simple means for obtaining an idea on the direction of flow close to a solid wall is to attach one end of short tufts to the body surface. In laminar, attached
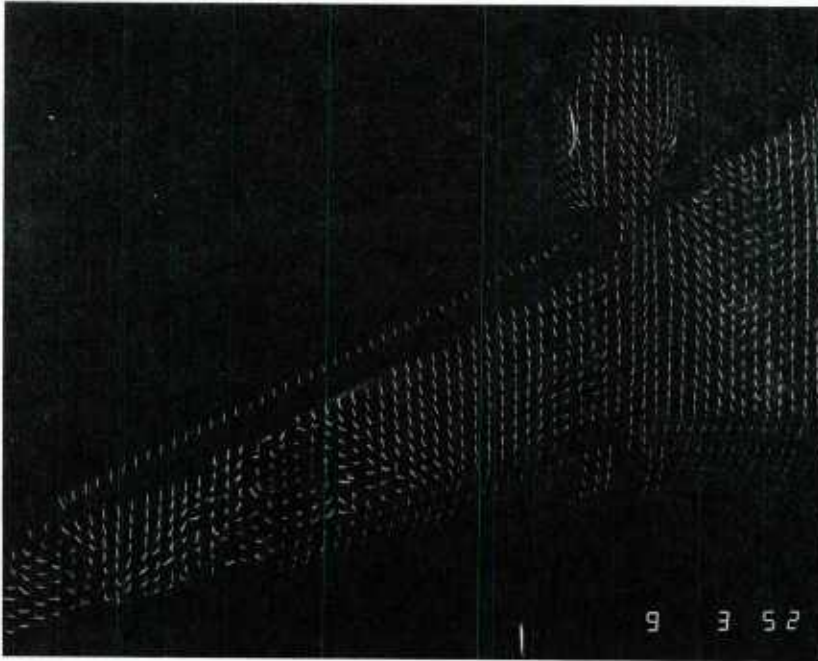
Fig. 2.5:   Fluorescent minitufts on the model of a transport airplane in a wind tunnel
            (J.P. Crowder, Boeing Aero Laboratories).

flow, these tufts may well indicate the local flow direction. When the flow becomes un-
steady or turbulent, the tufts perform a certain unsteady motion, and this may be taken
as an indication that the wall boundary layer has become turbulent. A more violent mo-
tion of the tufts, or a tendency to lift from the surface, may indicate a separated flow
regime.

The choice of tuft size and material depends on the flow conditions and the size of
the model to be tested. Tufts of ordinary yarn and several centimeters long have been
used on full-scale car models in a wind tunnel, and on full-scale airplanes in flight.
It is obvious that tufts of this size and the corrugation caused by the glue or the
device fixing the tufts affect the surface conditions of the flow. Furthermore, it has
been observed that, due to instabilities induced at particular wind speeds, the tufts
may perform a self-excited flagging motion, which obscures the indication of flow sepa-
ration. For in-flight tests, Crowder and Robertson [2.21] use light, rigid, narrow, co-
nical elements, which are attached to the wind surface with a short string at their
apex. In contrast to the tufts, these elements, several centimeters long, behave stable
in attached flow.

In order to minimize interference between tufts and flow, Crowder [2.22] has de-
veloped "minitufts" made from thin nylon monofilament, with a diameter of about 20 μm.
In order to enhance the visibility, the nylon is treated with fluorescent dye, and the
tufts are observed or photographed with UV illumination (Fig. 2.5). The surface flow
pattern on rotating propellers [2.23] as well on models in a water tunnel [2.24] has
been successfully visualized with these minitufts.


2.4   SURFACE FLOW VISUALIZATION DEPENDING ON MASS TRANSFER

Sublimation evaporation of a coating material into the adjacent air flow is a
means for visualizing the mass transfer between the solid surface and the flowing gas.
Use of this effect is made by the surface techniques employing coatings of either
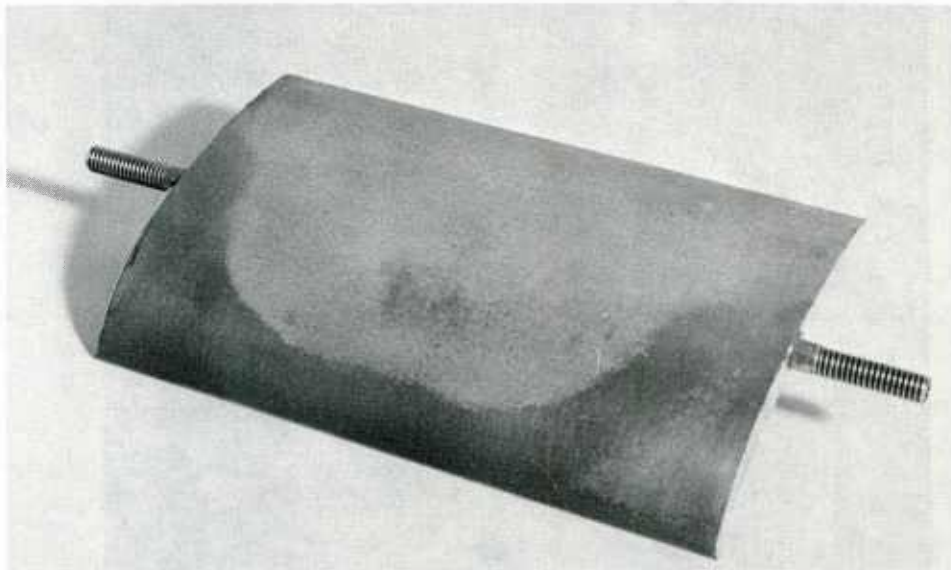
Fig. 2.6: Visualization of the location of laminar-to-turbulent transition on the low pressure surface of a turbine blade model. Visualization is by means of azobenzene whose sublimation is more rapid in the turbulent boundary layer, this region now appearing dark (DFVLR-Institut für Antriebstechnik, Köln, F.R.Germany).

naphtalene (see several publications by Sparrow et al., e.g., [2.25]), or azobenzene [2.26]. The rates of sublimation or mass transfer are different depending on whether the flow is laminar or turbulent, so that the location of transition can be made visible (Fig. 2.6). The naphtalene technique can even provide some degree of quantitative information: The surface is coated with a layer of dense naphtalene, the outer surface of the layer being smooth. Naphtalene sublimates into the outer air flow, and the resulting profile of the originally smooth surfaces reflects low and high mass transfer rates. A measurement of the naphtalene profile allows for obtaining values of the local mass transfer coefficient.

A very distinct surface visualization is achieved with methods in which the mass transfer results in a chemical reaction causing a color change on the body surface. For the technique described by Kottke [2.27,2.28], the wall is coated with a thin wet layer (filter paper or gel) containing an aqueous solution of $MnCl_2$ and $H_2O_2$. A reacting gas, $NH_3$, is added in form of a short pulse and at low concentration to the main airstream. $NH_3$ is adsorbed, according to the local partial concentration differences, by the wet layer, and a reaction takes place in which $MnO_2$ is formed as an end product. While the original coating is bright, $MnO_2$ is dark, so that the observed color intensity of $MnO_2$ is a measure of the local mass transfer rate (Fig. 2.7). Kottke performed quantitative measurements by photometric means. He observerd that the measured position of maximum mass transfer in a reattaching flow is not consistent with the expected line of flow attachment. This is just another indication of the difficulties that arise in interpreting surface patterns produced by separating flows.

## 2.5  VISUALIZATION OF WALL TEMPERATURE

The derivation of aerodynamic heat transfer coefficients requires the recording of the time history of a number of isotherms on the surface under study. Such isotherms can be visualized by means of surface coatings whose pattern or color reacts to changes of the surface temperature. Two coatings of this kind will be discussed here: tempera-
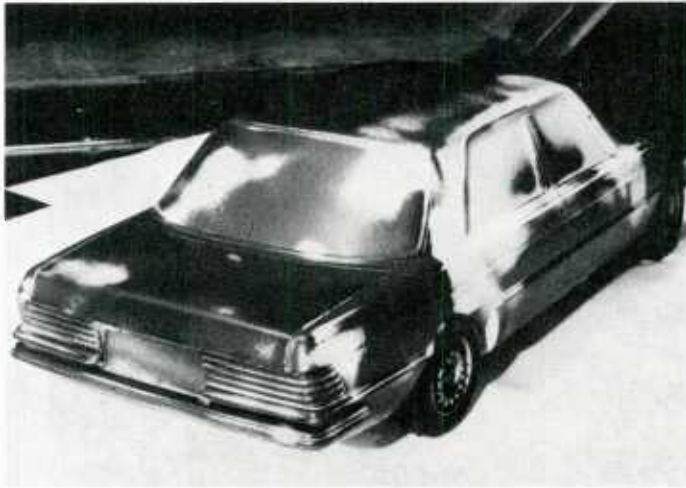
Fig. 2.7: Visualization of mass transfer to the surface of a car model in a wind tun-
nel. White areas indicate separated flow regimes with low mass transfer
rate (V. Kottke, Universität Stuttgart, F.R.Germany).

ture sensitive paints and liquid crystals, in addition to a method that does not rely on
a coating: infrared photography. The three methods have different ranges of application
and sensitivity. The paints are used at temperatures of several hundred Kelvin in high-
enthalpy flow facilities. Liquid crystals are sensitive in a range of only a few Kelvin,
and their application is at temperatures not too far from room temperature. Applicabili-
ty and sensitivity of the infrared camera is somewhere between the two former methods.

Temperature-sensitive paints have been used since many years of high-speed wind
tunnel testing, [2.29,2.30]. These paints consist of several components each of which
undergoes a visible change of its internal structure or phase at a specific temperature.
The edge between two colors is a curve of constant surface temperature. If the model is
made of a material with low thermal conductivity, the indicated temperature may be taken
as the adiabatic wall temperature. The edges between colors move on the body surface in
downstream direction with increasing time, until the whole body surface might have
reached a uniform temperature. A number of different paints are commercially available.

The edge between two colors of the paint is to a certain degree diffusive, so re-
ducing the local resolution of the mapping. More accurate in this respect is a one-com-
ponent paint ("phase change paint") which changes from solid to liquid at a precise sur-
face temperature [2.31-2.34]. Wax can be the major component of such coating. The ob-
served melt line is an isotherm. Keyes [2.35] reports that the coating can be blown off
due to high shear rates in the flow, and this phenomena could be misinterpreted to be a
phase change. In the cases of both temperature sensitive paint and phase change paint,
the process causing the visible color change is not reversible, so that this coating of
the surface can be used only once.

A reversible color change as a function of the surface temperature can be obtained
with a coating of liquid crystals. Klein [2.36] gave a first description of the use of
liquid crystals for the study of aerodynamic surface heating. Temperature changes in
such crystals disturb the intermolecular forces and generate a shift in the molecular
structure, thus causing a shift in wavelength of the light scattered from the crystals.
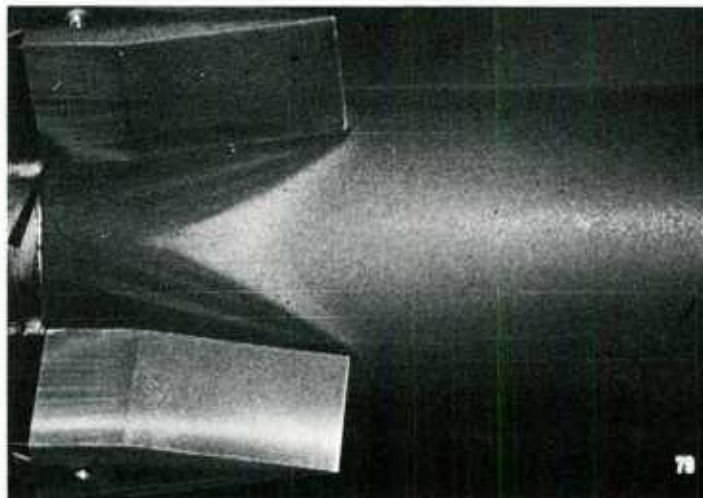
Fig. 2.8:    Surface temperature mapping by liquid crystals in a hypersonic wind tunnel.
Fins on a cylindrical body whose axis is in the flow direction produce ob-
lique shock waves: The intersection of these shock waves with the cylindri-
cal surface is visible due to the temperature rise through the shock (H.
Schöler, DFVLR-Institut für Experimentelle Strömungsmechanik, Göttingen,
F.R.Germany).

An extensive literature is available on liquid crystals and their application in differ-
ent fields. Among the various types, cholesteric liquid crystals have been proven to be
most suitable for studies in fluid mechanics and convective heat transfer. Unlike tem-
perature sensitive paints, cholesteric liquid crystals react to changes of temperatures
only within a few degrees Kelvin. The crystals are commercially available, for a great
range of both bandwidth and mean temperature at which they are sensitive. Within the
bandwidth of their sensitivity, up to ten color hues may be discriminated by the eye.
The visible edge between two colors is a curve of constant temperature (Fig. 2.8). The
value of the temperature must be found by calibration for constant viewing direction.

A thin sheet of liquid crystals on a solid surface might be affected by shear
forces or, if the coating is used in water, by contamination. In order to protect the
crystals, they can be made available in the form of sheets consisting of the liquid
crystals laid on plastic material and covered by a transparent protecting layer [2.37,
2.38], or they are "microencapsulated", i.e., enclosed in plastic spheres of 10 to 50 μm
in diameter [2.39]. Dispersing the encapsulated liquid crystals in water gives an emul-
sion which can be brushed or sprayed on the model surface. Cholesteric liquid crystals
have been applied to the flow in wind tunnels [2.39,2.40] and in water tunnels [2.41,
2.42].

The surface of a solid body emits infrared (IR) radiation whose intensity is a
function of the surface temperature. This radiation can be received with an IR camera,
which, in connection with appropriate computer hardware and software, converts the
signal into a visual pattern. Several successful attempts have been made for mapping
the surface temperature distribution of models in wind tunnels or in other flow en-
vironments by means of an IR camera; see, e.g. [2.43,2.44]. Most of the reported experi-
ments have been performed with an IR camera which is commercially available; it employs
a detector sensitive to the wavelength range between 3 and 5.8 μm. The detector, which
must be cooled by liquid nitrogen, produces an electric signal proportional to the re-
ceived total energy. The total radiant energy emitted by the surface under investigation
is, according to the Stefan-Boltzmann law for a gray body, proportional to the 4th power
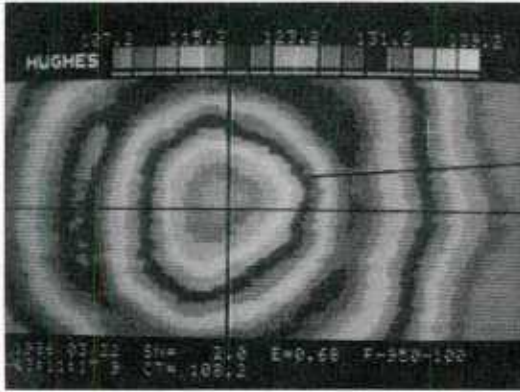
Fig. 2.9:
Infrared (IR) camera display of the temperature distribution on a surface on which a gas jet is impinging. The visible pattern are surface temperature contours. Mean jet flow velocity is 45 m/s (R.H. Page, C. Ostowari, Texas A&M University).

of the absolute temperature. Gauffre and Fontanella [2.45] give an overview on IR cameras used for aerodynamic experiments, while Boylan et al. [2.43] describe ways of calibration of the system. The surface temperature pattern can be displayed in real time on a monitor (Fig. 2.9).

A way for determining the aerodynamic heat transfer coefficient h has been devised by Jones and Hunt [2.31]. For this purpose, it is necessary to record the isotherms as a function of time, e.g., by taking a movie film. The method is based on the transient, one-dimensional analysis of heat flow from the model surface into the body. The differential equation

$$\frac{\partial T}{\partial t} = \alpha \cdot \frac{\partial^2 T}{\partial y^2}$$ (2.3)

(with T = absolute temperature, t = time, y = coordinate normal to the model surface, $\alpha = k/\rho c_p$ = thermal diffusivity of the model material, k = thermal conductivity, $\rho$ = density of model material, and $c_p$ its specific heat) is solved for the following initial and boundary conditions:

- $T(y,0) = T_i$ is the initial temperature of the model. In practice, t = 0 is the instant at which the model is injected into the wind tunnel.

- $T(\infty,t) = T_i$: thermal diffusion within the model material is slow.

- $\frac{\partial T(0,t)}{\partial x} = \frac{h}{k} \cdot (T_{aw} - T(0,t))$, with $T_{aw}$ = adiabatic wall temperature, h = aerodynamic heat transfer coefficient. This condition describes the development of the surface temperature (at y = 0) due to aerodynamic heating.

With a number of additional simplifying assumptions, Jones and Hunt develop the following solution for the heat flow equation (2.3):

$$T^* = 1 - \exp(\beta^2) \cdot \text{erfc } \beta$$ (2.4)

with the abbreviations

$$T^* = \frac{T_{ind} - T_i}{T_{aw} - T_i} \quad , \quad \beta = \frac{h}{k} \cdot \sqrt{\alpha \cdot t} \quad , \quad \text{erfc } \beta = \frac{2}{\pi} \int_{\beta}^{\infty} e^{-\lambda^2} d\lambda \quad .$$

$T_{ind}$ is the temperature of an isotherm indicated by the specific coating. The determination of h is as follows: With given $T_{ind}$ for a specific indicator one determines the value of T* and, from a plot T* versus β [2.31], the corresponding value of β. With known values k, α and measured time t (for the isotherm to appear at a specific position on the surface, as measured from the movie film), one determines $h = k \cdot \beta/\sqrt{\alpha t}$. The time required for the isotherms to move over the model surface should be large compared with the time necessary for establishing a steady flow around the model, and it must be short compared with the thermal diffusion time of the model material. Segletes [2.32] points out that the one-dimensional heat transfer model used in the above analysis may, in some cases, lead to large errors. He presents correction factors that improve the results of the 1-D analysis for particular corner flows.

## References

2.1.    Maltby, R.L. (editor):  Flow Visualization in Wind Tunnels Using Indicators. AGARDograph no. 70, 1962.

2.2.    Settles, G.S.; Teng, H.-Y.:  Flow visualization methods for separated three-dimensional shock wave/turbulent boundary layer interactions. AIAA J. 21 (1983), 390-397.

2.3.    Maltby, R.L.; Keating, R.F.A.:  The surface oil flow technique for use in low speed wind tunnels. In [2.1], pp. 29-38, 1962.

2.4.    Stanbrook, A.:  The surface oil flow technique for use in high speed wind tunnels. In [2.1], pp. 39-49, 1962.

2.5.    Kell, D.M.:  A surface flow visualization technique for use in cryogenic wind tunnels. Aeronaut. J. (1978), 484-487.

2.6.    Meznarsic, V.F.; Gross, L.W.:  Experimental investigation of a wing with controlled midspan flow separation. J. Aircraft 19 (1982), 435-441.

2.7.    Sparrow, E.M.; Comb, J.W.:  Effect of interwall spacing and fluid flow inlet conditions on a corrugated-wall heat exchanger. Int. J. Heat Mass Transfer 26 (1983), 993-1005.

2.8.    Keener, E.R.:  Oil flow separation patterns on an ogive forebody. AIAA J. 21 (1983), 550-556.

2.9.    Gessner, F.B.; Chan, Y.L.:  Flow in a rectangular diffuser with local flow detachment in the corner region. J. Fluids Eng. 105 (1983), 204-211.

2.10. Hornung, H.:  Die Entwicklung eines Anstrichbilds bei Windkanalversuchen. In: Ernst-Becker-Gedächtnis-Kolloquium, Vol.28 of THD-Schriftenreihe Wissenschaft und Technik, pp. 113-123, Techn. Hochschule Darmstadt, 1986.

2.11. Murai, H.; Ihara, A.; Narasaka, T.:  Visual investigation of formation process of oil-flow pattern. In [1.5], pp. 629-633, 1982.

2.12. Squire, L.C.:  The motion of a thin oil sheet under the boundary layer on a body. In [2.1], pp. 7-28, 1962.

2.13. George, A.R.:  Aerodynamic effects of shape, camber, pitch, and ground proximity on idealized ground-vehicle bodies. J. Fluids Eng. 103 (1981), 631-638.

2.14. Reding, J.P.; Ericsson, L.E.:  Flow visualization reveals causes of shuttle nonlinear aerodynamics. J. Aircraft 19 (1982), 928-933.

2.15. Settles, G.S.; Perkins, J.J.; Bogdonoff, S.M.:  Investigation of three-dimensional shock/boundary layer interactions at swept compression corners. AIAA J. 18 (1980), 779-785.

2.16. Tanner, L.H.; Blows, L.G.:  A study of the motion of oil films on surface in air flow, with application to the measurement of skin friction. J. Phys. E: Sci. Instrum. 9 (1976), 194-202.

2.17. Tanner, L.H.:  Skin friction measurements by viscosity balance in air and water flows. J. Phys. E: Sci. Instrum. 12 (1979), 610-619.

2.18. Tanner, L.H.:  Surface flow visualization and measurement by oil film interferometry. In [1.5], pp. 613-617, 1982.

2.19. Szodruch, J.; Monson, D.J.:  Messung und Sichtbarmachung der lee-seitigen Wandschubspannung bei Deltaflügeln im Überschall. Z. Flugwiss. Weltraumforsch. 6 (1982), 279-283.

2.20. Monson, D.K.:  A nonintrusive laser interferometer method for measurement of skin friction. Exp. Fluids 1 (1983), 15-22.

2.21. Crowder, J.P.; Robertson, P.E.:  Flow cones for airplane flight test flow visualization. In [1.6], pp. 60-64, 1985.

2.22. Crowder, J.P.: Fluorescent minitufts for nonintrusive flow visualization. In [1.5], pp. 663-667, 1982.

2.23. Crowder, J.P.: Fluorescent minitufts for flow visualization of rotating surfaces. In [1.6], pp. 55-59, 1985.

2.24. Stinebring, D.R.; Treaster, A.L.: Water tunnel flow visualization by the use of fluorescent mini-tufts. In [1.6], pp. 65-70, 1985.

2.25. Sparrow, E.M.; Vemuri, S.B.; Kadle, D.S.: Enhanced and local heat transfer, pressure drop, and flow visualization for arrays of block-like electronic components. Int. J. Heat Mass Transfer 26 (1983), 689-699.

2.26. Heilmann, W.: Experimentelle und grenzschichttheoretische Untersuchungen an ebenen Verzögerungsgittern bei kompressibler Strömung, insbesondere bei Änderung des axialen Stromdichteverhältnisses und der Zuströmbilanz. DLR FB 67-88, 1967.

2.27. Kottke, V.; Blenke, H.; Schmidt, H.G.: Eine remissionsfotometrische Meßmethode zur Bestimmung örtlicher Stoffübertragungskoeffizienten bei Zwangskonvektion in Luft. Wärme- und Stoffübertragung 10 (1977), 9-21.

2.28. Kottke, V.: A chemical method for flow visualization and determination of local mass transfer. In [1.5], pp. 657-661, 1982.

2.29. Cérésuela, R.; Bétremieux, A.; Cadars, J.: Mesure de l'échauffement cinétique dans les souffleries hypersoniques à moyen de peintures thermosensibles. Rech. Aérosp. No. 109 (1965), 13-19.

2.30. Kafka, G.; Gaz, J.; Yee, W.T.: Measurement of aerodynamic heating of wind-tunnel models by means of temperature sensitive paint. J. Spacecraft 2 (1965), 475-477.

2.31. Jones, R.A.; Hunt, J.L.: Use of fusible temperature indicators for obtaining quantitative aerodynamic heat transfer data. NASA TR R-230, 1966.

2.32. Segletes, J.A.: Errors in aerodynamic heat transfer measurements when using phase change coating techniques, J. Spacecraft 12 (1975), 124-126.

2.33. Drummond, J.P.; Jones, R.A.; Ash, R.L.: Effective thermal property improves phase change paint data. AIAA J. 14 (1976), 1476-1478.

2.34. Maegly, W.J.; Carroll, H.R.: MX missile thermal mapping and surface flow results. J. Spacecraft Rockets 19 (1982), 199-204.

2.35. Keyes, J.W.: Shock interference peak heating measurements using phase change coatings. J. Spacecraft Rockets 13 (1976), 61-63.

2.36. Klein, E.J.: Application of liquid cystals to boundary layer visualization. AIAA Paper 68-376, 1968.

2.37. Hippensteel, S.A.; Russel, L.M.; Stepka, F.S.: Evaluation of a method for heat transfer measurements and thermal visualization using a composite of heater elements and liquid crystals. J. Heat Transfer 105 (1983), 184-189.

2.38. Kitamura, K.; Koike, M.; Fukuoka, I.; Saito, T.: Large eddy structure and heat transfer of turbulent natural convection along a vertical flat plate. Int. J. Heat Mass Transfer 28 (1985), 837-850.

2.39. Schöler, H.: Liquid crystals for remote surface temperature and heat transfer measurement. DFVLR IB 222-81 A 23, 1981.

2.40. Schöler, H.: Application of encapsulated liquid crystals on heat transfer measurements in the fin-body interaction region at hypersonic speed. AIAA Paper 78-777, 1978.

2.41. Ogden, T.R.; Hendricks, E.W.: Liquid crystal thermography in water tunnels. Exp. Fluids 2 (1984), 65-66.

2.42. Simonich, J.C.; Moffat, R.J.: New techniques for mapping heat transfer coefficient contours. Rev. Sci. Instrum. 53 (1982), 678-683.

2.43. Boylan, D.E.; Carver, D.B.; Stallings, D.W.; Trimmer, L.L.: Measurement and mapping of aerodynamic heating using a remote infrared scanning camera in continuous flow wind tunnels. AIAA Paper 78-799, 1978.

2.44. Bandettini, A.; Peake, D.J.: Diagnosis of separated flow regions on wind-tunnel models using an infrared camera. ICIASF '79 Record (IEEE Publ. 79CH1500-8AES), pp. 171-185, 1979.

2.45. Gauffre, G.; Fontanella, J.C.: Les caméras infrarouges: principes, caractérisation, utilisation. Rech. Aérosp. No. 1980-4, 259-269.

## 3. DIRECT INJECTION METHODS

The injection of a foreign, visible material is a traditional means of flow visualization. Most commonly, dyes are used in water, and smoke in air flows. The material is released from a particular position, thus marking a specific line in the flow downstream of that

position; or, the material is filling a complete regime in the flow, and it marks the boundary and therefore the geometric extension of such a regime, provided that there is little mass exchange across the boundary. The latter is of interest for visualizing separated flow regimes.

The particles of the injected material are required to be small so that they can well follow the flow. However, the motion of individual particles is not studied here. The number density of the particles in the fluid is so high, that the individual particles lose their identity in the observations, and instead, one observes a continuous ensemble of the "marked" fluid, e.g. in the form of the aforementioned lines. In steady flow the line is a streamline, and the interpretation of a pattern of such lines is straightforward. For an unsteady flow field, the marked contours are named "streaklines", defined as the instantaneous locus of all fluid elements having passed a specific position, i.e., the position where the dye or smoke is injected. Difficulties can arise in the interpretation of the streakline patterns of an unsteady flow; see, e.g., [3.1].

## 3.1   SMOKE FLOW VISUALIZATION

The visualization of the flow in wind tunnels by means of smoke is now a standard experimental tool for the work in these facilities. The advancement of this technique is closely related to the development and the history of wind tunnels [3.2]. An essential portion of the progress and refinement of the smoke technique is due to the work of Brown [3.3] at the University of Notre Dame. He systematically developed the generation of appropriate smokes as well as the performance of suitable wind tunnels, later referred to as "smoke tunnels". Reviews of this visualization method have been given by Maltby and Keating [3.4] and by Mueller [3.5].

The term "smoke" is used here in a wide sense, not only restricted to combustion products, and the discussion will include steam, vapor, mist, and aerosols. From the usual requirement that one wants a tracer material to fulfill, namely

- being neutrally buoyant,
- being non-toxic, and
- having low mixing rates with the main fluid,

smoke fulfills none of these. The use of smoke is therefore a compromise, and no better technical solution has been found yet.

The basic types of producing smoke are: burning or smoldering tobacco, wood or straw; vaporizing mineral oils; producing mist as the result of the reaction of various chemical  substances; and condensing steam to form a visible fog. Except of the latter, all these substances are toxic to some degree. The density of these tracer materials is much larger than the density of air, but since the particle size of the tracers is very small, mostly below 1 m$\mu$, sedimentation effects are minimized. Diffusion of the various types of smoke into the ambient air is much higher than diffusion of dye into water, so that streaklines can be identified over a reasonable distance only in laminar flow (Fig. 3.1).

A number of possible smokes and ways of their generation (often called smoke-generators), together with relevant references are listed in Table 3.1. Cigarette smoke has the finest tracer particles among all smokes. Kerosene mist probably is the most frequently used "smoke" for wind tunnel studies. The generation of $TiO_2$ mist from $TiCl_4$ droplets deposited on the surface of a test model is not a direct injection method, but rather a method of chemical controlled production of the trace material (see also
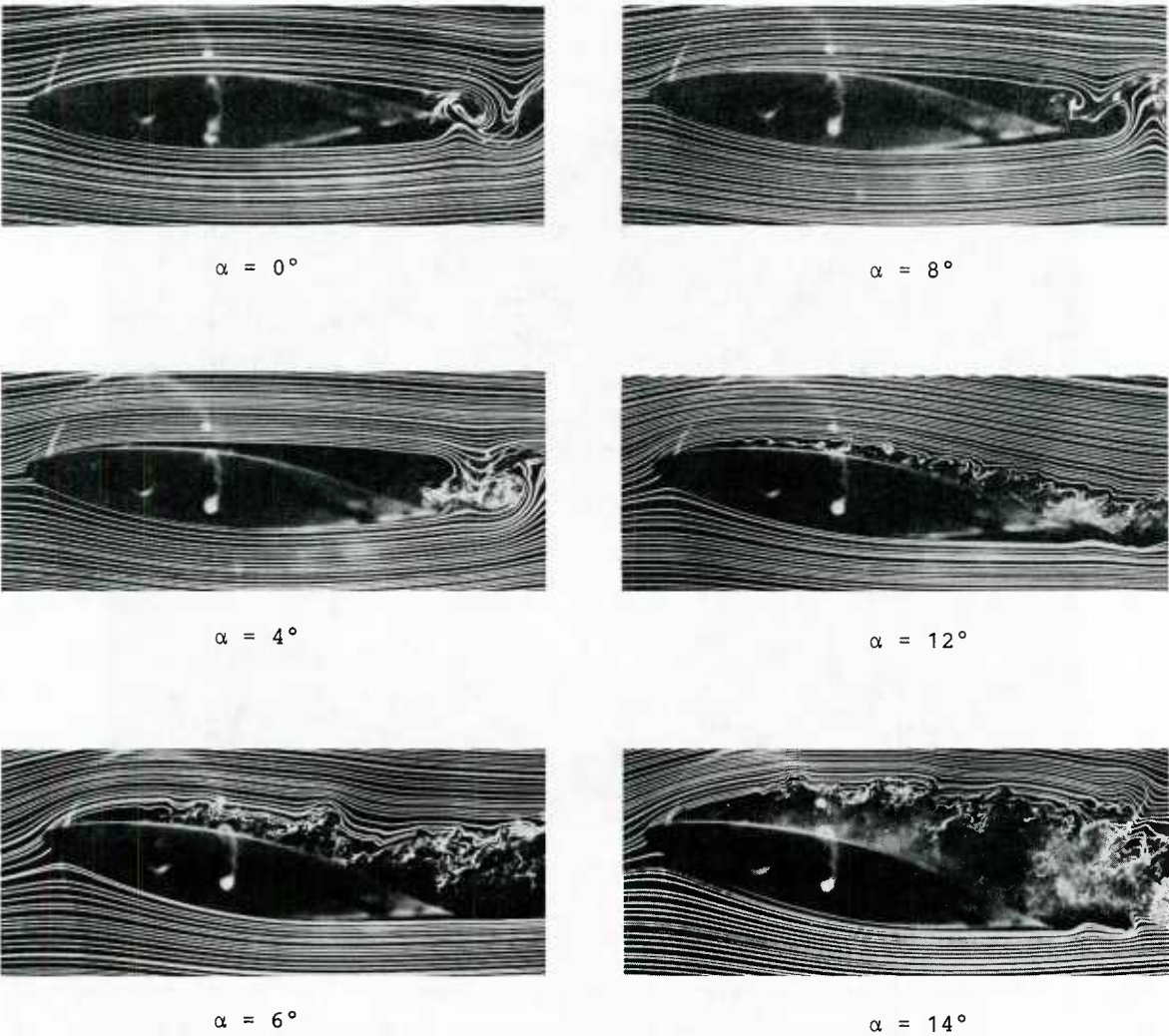
$$\alpha = 0°$$

$$\alpha = 8°$$

$$\alpha = 4°$$

$$\alpha = 12°$$

$$\alpha = 6°$$

$$\alpha = 14°$$

Fig. 3.1: Smoke-line visualization of the flow over an airfoil at Re=4o.ooo and various angles of attack, $\alpha$ (T.J. Mueller, University of Notre Dame, Indiana, USA).

Table 3.1

Smokes and methods of their generation

| | |
|---|---|
| cigarette smoke | properties see [3.6] |
| burning pine wood | smoke generator see [3.8] |
| kerosene mist | Preston-Sweeting smoke generator [3.], |
| | see also [3.4], [3.9]; |
| | University of Notre Dame smoke generator [3.5] |
| | smoke wire, see chapter 5 |
| | |
| $TiO_2$ mist | generator based on the reaction $TiCl_4 + 2 H_2O$, see [3.10]; |
| water fog | injection of steam and liquid nitrogen, see [3.14 - 3.16]; |
| | by dropping $CO_2$ pellets in hot water; generator see [3.17]. |

chapter 4). The smoke wire, an electrically controlled device (see chapter 5), allows for the generation of very fine smoke lines. Direct injection of the smoke is performed by means of a smoke pipe (Fig. 3.2) or a system of such pipes ("rake").
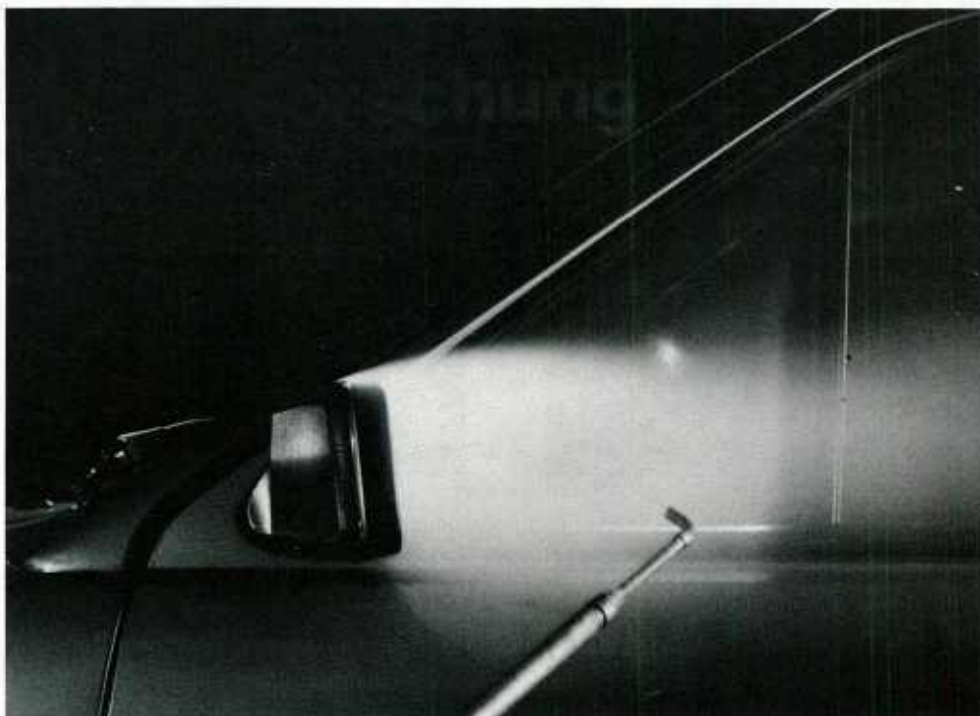


Fig. 3.2:   Smoke is injected with a smoke pipe into the separated flow behind an external mirror at the front door of a car. The smoke fills the entire separated flow regime. The experiment has been performed in a full-scale windtunnel (Volkswagenwerk AG, Wolfsburg, F.R. Germany).

The application of smoke to a recirculating wind tunnel creates the problem that, after a certain time of operation, the tunnel is completely filled with smoke. For this reason, and also because any smoke or aerosol is toxic to some extent, there is an interest in using steam or water fog as the trace material. Steam in combination with a cooling agent can be introduced in the air flow where a visible fog is produced [3.14]. After heat exchange with the surrounding air, the fog disappears, leaving the main air stream clean in the recirculating system. An air drying device might be needed. Liquid nitrogen may serve as the cooling agent, so that steam and liquid nitrogen are expelled together into the air stream through a mixing nozzle [3.14, 3.16]. From preliminary experiments performed in relatively small wind tunnels, it has been reported that the visibility of such fog compares with that of $TiO_2$ mist or cigarette smoke; but the fog "particles" are larger than the particles of the two former materials.

For the reasons discussed in the latter paragraph, many smoke flow experiments are performed in wind tunnels exhausting directly into the atmosphere. Injection of the smoke ahead of the contraction and a large contraction ratio serve to stabilize the smoke lines. In principle, there is no  upper limit in air speed for the application of smoke, and smoke lines have been generated even in supersonic flow [3.18]. Illumination in the smoke experiments is mostly conventional, i.e., front light illumination under a certain angle with respect to the viewing direction with conventional sources, e.g., mercury lamps, halogen lamps, spot lights. More recently, illumination in form of a plane, thin light sheet is applied in order to visualize flow structures in a certain cross section of the flow field (see chapter 5).

Beyond the use in wind tunnels, smoke flow visualization has been applied in any kind of air flows, even for large scale, outdoor experiments or studies. Its special role for detecting separated flow regimes (Fig. 3.3), vortices, and coherent structures in shear layers (Fig. 3.4) should be emphasized.
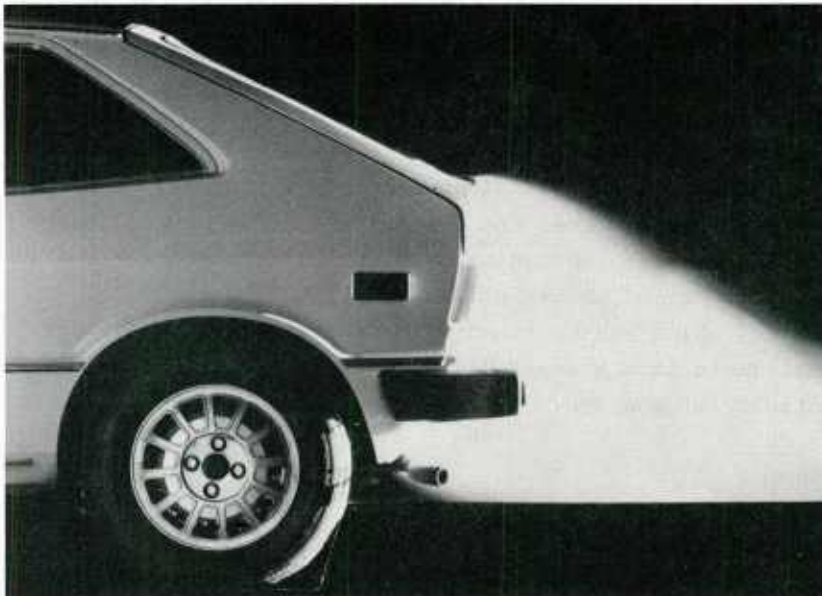
Fig. 3.3:  Smoke is introduced into the attached boundary layer of the inclined back of
a car. It separates with the boundary layer and fills the entire wake (Volks-
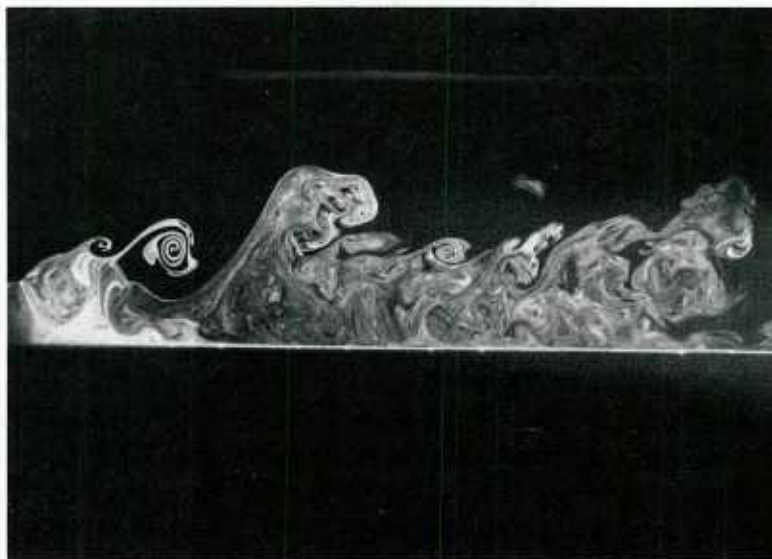wagenwerk AG, Wolfsburg, F.R. Germany).



Fig. 3.4:  Smoke in the separated flow regime behind a vertical fence visualizes coherent
structures in the separated shear layer. Reynolds number based on the fence
height is $1.5 \times 10^3$ (H.H. Fernholz, Technische Universität Berlin, R.F.Germany).

## 3.2   VISUALIZATION BY DYE IN WATER

The visualization of water flows by means of dye is as popular as the use of smoke
in air flows. The various dye techniques have been reviewed by Clayton and Massey [3.19],
and by Werlé [3.20]. The particular situation of dye visualization in towing tanks has
been described by Gad-el-Hak [3.21]. Unlike smoke, appropriate dyes can fulfill almost
any requirements of an ideal tracer,

- neutral buoyancy,
- high stability against mixing
- good visibility.

Most materials are non-toxic, and even if they are not so, the toxicity is kept within the liquid flow system and will have little exchange with the environment. As the name says, dye visualization includes colour as an additional dimension for discrimination. Neutral buoyancy can be attained by mixing the dye material with a fluid whose specific weight is lower than that of water, e.g., alcohol. The mixture normally is not a true solution, and, under the action of inertial or centrifugal forces, which act in different ways on the components of the mixture, the dye tracers might not indicate the true flow direction. Such a discrepancy is avoided by complete dilution of the dye in the water (food coloring, ink). A number of possible dyes are listed in Table 3.2, together with relevant references. Milk, which can be mixed with certain dyes, particularly food coloring, preserves the dye filaments from a rapid diffusion into the water. At the same time, milk improves the reflectivity of the dye.

Table 3.2

Dyes for water flow visualization and respective references

| food coloring | [3.22 - 3.26] |
| food coloring and milk | [3.21; 3.27; 3.28] |
| ink | [3.29] |
| potassium permanganate | [3.30] |
| fluorescent ink | [3.31] |
| Rhodamine | [3.32 - 3.34] |
| Fluoresceine | [3.33 - 3.35] |

As in the case of smoke tracers, dye is released from small ejector tubes or from small orifices in the wall of a test model. Hypodermic tubes or syringes, or small Pitot tubes can serve as dye ejectors. Conventional front light illumination is sufficient in most cases.

Special lighting devices are necessary for fluorescing dyes. These dyes must be excited by a light source which radiates in the spectral range of greatest fluorescence of the dye, e.g., a mercury lamp or an Argon ion laser. The exciting illumination should be normal or oblique to the direction of observation, because one records the scattered fluorescent radiation. Table 3.2 includes two trademarks of fluorescing dyes. Rhodamine-6G, the most frequently employed material of this type, emits a yellow radiation, when excited by an $Ar^+$ laser, Rhodamine-B radiates dark-red, Fluoresceine green. Rhodamine is soluble in methanol, which might be of interest for adjusting the specific weight of the tracer material. Recent developments in laser-induced fluorescence allow for determining the concentration of the dyed fluid from the measurement of radiation intensity [3.35].

The flow phenomena visualized by means of dye in water tunnels are the same as those studied by smoke visualization in air (Figs.3.5, 3.6). The simulation of aerodynamic flow problems in water tunnels has a specific experimental advantage, see, e.g.,[3.26; 3.36]: For the same unit Reynolds number and model scale, the velocity in water is 1/15 of that in air, so that these phenomena can be observed at a relatively low speed.

A special visualization technique has been developed for towing tanks [3.21; 3.32]. Thin, horizontal dye layers are produced in the water before the model is set into motion. The flow around the model displaces the colored layers whose movement can be observed and recorded. The dye layers can be stabilized by a weak saline stratification in the tank. The time scale for diffusion of the dye layers into the stratified salt-water is large compared to the time needed for one test run, so that the system of horizontal dye layers can be used for several experiments.
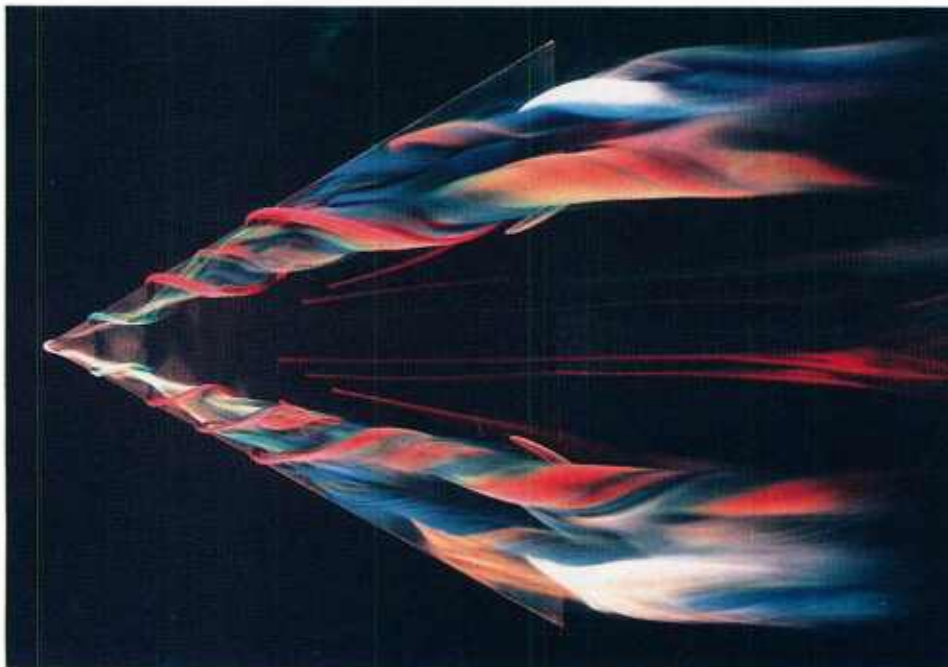
Fig. 3.5: Dye line visualization of trailing vortices separating from a delta shaped wing in a water tunnel. (H.Werlé, ONERA, France)
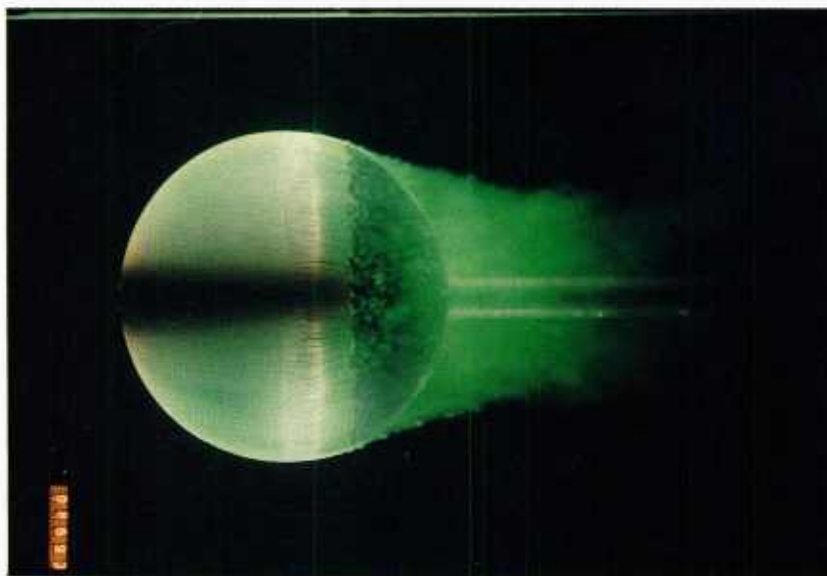


Fig. 3.6: Dye visualization of boundary layer transition and separation on a sphere in a water tunnel at $Re = 3 \cdot 10^5$. (H. Werlé, ONERA, France)

## References

3.1. Kurosaka, M.; Sundaram, P.: Illustrative examples of streaklines in unsteady vortices: Interpretational difficulties revisited.Phys. Fluids 29 (1986), 3474-3477.

3.2. Mueller, T.J.: On the historical development of apparatus and techniques for smoke visualization of subsonic and supersonic flow. AIAA Paper 80-0430-CP, 1980.

3.3. Brown, F.N.M.: A photographic technique for the mensuration and evaluation of aerodynamic patterns. Phot. Eng. 4 (1953), 146-156.

3.4. Maltby, R.L.; Keating, R.F.A.: Smoke techniques for use in low speed wind tunnels. In [2.1], pp. 87-109, 1962.

3.5 Mueller, T.J.: Flow visualization by direct injection. In: Fluid Mechanics Measurements (ed. R.J. Goldstein), pp. 307-375, Hemisphere, Washington, 1983.

20

3.6. Kerker, M.; Sculley, M.J.; Farone, W.A.; Kassman, A.J.: Optical properties of cigarette smoke aerosols. Appl. Opt. 17 (1978), 3030-3031.

3.7. Yu, J.P.; Sparrow, E.M.; Ecker, E.R.G.: A smoke generator for use in fluid flow visualization. Int. J. Heat Mass Transfer 15 (1972), 557-558.

3.8. Preston, J.; Sweeting, N.E.: An improved smoke generator for use at high Reynolds numbers. ARC R & M 2023, 1943.

3.9. Warpinski, N.R.; Nagib, H.M.; Lavan, Z.: Experimental inverstigation of recirculating cells in laminar coaxial jets. AIAA J. 10 (1972), 1204-1210.

3.1o. Hussain, A.K.M.F.; Clark, A.R.: On the coherent structure of the axisymmetric mixing layer: a flow-visualization study. J. Fluid Mech. 104 (1981), 263-294.

3.11. Freymuth, P.; Bank, W.; Palmer, M.: Visualization of accelerating flow around an airfoil at high angles of attack. Z. Flugwiss. Weltraumforsch. 7 (1983), 392-400.

3.12. Griffin, O.M.; Votaw, C.W.: The use of aerosols for the visualization of flow phenomena. Int. J. Heat Mass Transfer 16 (1973), 217-219.

3.13. Griffin, O.M.; Ramberg, S.E.: Vortex shedding from a cylinder vibrating in line with an incident uniform flow. J. Fluid Mech. 75 (1976), 257-271.

3.14. Prentice, C.J.; Hurley, F.X.: Subsonic flow visualization using steam. J. Aircraft 7 (1970), 380.

3.15. Bisplinghoff, R.L.; Coffing, J.B.; Haldeman, C.W.: Water fog generation system for subsonic flow visualization. AIAA J. 14 (1976), 1133-1135.

3.16. Parker, A.G.; Brusse, J.C.: Noew smoke generator for flow visualization in low speed wind tunnels. J. Aircraft 13 (1976), 57-58.

3.17. Bouchez, J.P.; Goldstein, R.J.: Impingement cooling from a circular jet in a cross flow. Int. J. Heat Mass Transfer 18 (1975), 719-730.

3.18. Batill, S.M.; Nelson, R.C.; Mueller, T.J.; Wells, W.C.: Smoke visualization at transonic and supersonic Mach numbers. AIAA Paper 82-0188, 1982.

3.19. Clayton, B.R.; Massey, B.S.: Flow visualization in water: A review of techniques. J. Sci. Instrum. 44 (1967), 2-11.

3.20. Werlê, H.: Hydrodynamic flow visualization. Ann. Rev. Fluid Mech. 5 (1973), 361-382.

3.21. Gad-el-Hak, M.: The water towing tank as an experimental facility. - A review. Exp. Fluids 5 (1987), 289-297.

3.22. Sarpkaya, T.: On stationary and travelling vortex breakdowns. J. Fluid Mech. 45 (1972), 545-559.

3.23. Maxworthy, T.: The structure and stability of vortex rings. J. Fluid Mech. 51 (1972), 15-32.

3.24. Offen, G.R.; Kline, S.J.: Combined dye-streak and hydrogen bubble visual observations of a turbulent boundary layer. J. Fluid Mech. 62 (1974), 223-239.

3.25. Pullin, D.I.; Perry, A.E.: Some flow visualization experiments on the starting vortex. J. Fluid Mech. 97 (1980), 239-255.

3.26. Werlê, H.: Transition et décollement: Visualisations au tunnel hydrodynamiques de l'ONERA. Rechn. Aérosp. 1980-5, 331-345.

3.27. Werlê, H.: Hydrodynamic visualization on streamlined bodies of vortex flows particular to higher angles of attack. In [1.5], pp. 373-378, 1982.

3.28. Faler, J.H.; Leibovich, S.: Disrupted states of vortex flow and vortex breakdown. Phys. Fluids 2o (1977), 1385-1400.

3.29. Kotas, T.J.: Streamline pattern in a confined vortex flow. J. Mech. Eng. Sci. 19 (1977), 38-41.

3.3o. Masliyah, J.H.: On laminar flow in curved semicircular ducts. J. Fluid Mech. 99 (1980), 469-479.

3.31. Lynch, W.H.; Brown, A.E.: Flow measurement by fluorescing dye dilution techniques. In: Flow - Its Measurement and Control in Science and Industry (ed. R.B. Dowdell), pp. 781-785, ISA, Pittsburgh, 1974.

3.32. Gad-el-Hak, M.; Blackwelder, R.F.; Riley, J.J.: On the growth of turbulent regions in laminar boundary layers. J. Fluid Mech. 11o (1981), 73-95.

3.33. Dumas, R.; Domptail, C.; Daien, E.: Hydrodynamic visualization of some turbulent flow structures. In [1.5], pp. 393-397, 1982.

3.34. Thomas, A.S.W.; Cornelius, K.C.: Investigation of a laminar boundary-layer suction slot. AIAA J. 2o (1982), 790-796.

3.35. Koochesfahani, M.M.; Dimotakis, P.E.: Laser-induced fluorescence measurements of mixed fluid concentration in a liquid plane shear layer. AIAA J. 23 (1985) 17oo - 17o7.

3.36. Erickson, G.E.: Water tunnel flow visualization: Insight into complex three-dimensional flow fields. AIAA Paper 79-153o, 1979.

## 4. ELECTRICAL, CHEMICAL AND OPTICAL CONTROL OF TRACER PRODUCTION

The release of smoke and dye from injection tubes suffers from the disturbance of the flow by these mechanical devices and a lack of control in time of tracer production. Another shortcoming is that these devices are only point sources of the trace material. It would be advantageous if the material could be produced along a prescribed curve in the flow at the same instant of time, i.e. released from a line source. Orientation of the line source normal to the main flow direction would result in the visualization of velocity profiles. It will be shown that such arrangements can be realized for both air and water flows. The line source is either defined by a thin wire, and the tracer production is controlled by an electric signal along the wire; or, the reaction generating the tracer material is controlled without the need of a wire by a thin optical or electromagnetic beam which propagates along a straight line through the fluid. Table 4.1 gives a survey of these methods which will be discussed in the following subsections.

### Table 4.1

Survey of methods for the visualization of velocity profiles

| fluid | method | tracer | tracer generated by | general properties |
|-------|--------|--------|---------------------|--------------------|
| water | tellurium method | tellurium cloud | wire electrode | non-reversible tracer production (contamination of fluid); not neutrally buoyant |
| water | hydrogen bubble method | hydrogen bubbles | wire electrode | no contamination of fluid; not neutrally buoyant |
| water | thymol blue method | pH indicator | wire electrode | true solution (neutrally buoyant); reversible reaction (no contamination) |
| organic fluid | photochromism | photochromic dye | UV laser beam | neutrally buoyant; reversible reaction (no contamination); optical control (no wire needed) |
| air | smoke wire | smoke | pulse-heated wire | contamination by smoke |
| air | spark tracer method | line of ionized (luminous) air | electric discharge | no contamination; tracer lighter than working fluid: large errors possible in accelarated flow |

### 4.1 HYDROGEN BUBBLE METHOD

Electrolysis of water is the basic principle of this method. It is known that hydrogen bubbles are formed at the cathode and oxygen bubbles at the anode, when a DC voltage is applied between two electrodes in water. The hydrogen bubbles develop with much smaller size than the oxygen bubbles, and only the hydrogen bubbles are used as flow tracers. A thin wire normal to the mean flow direction usually serves as the cathode. A short electric pulse in the electrolytic circuit generates a line of hydrogen bubbles along the wire. This line or row is carried away with the flow, and it deforms according to the local velocity profile, which becomes visible when the bubble line is seen from the side (Fig. 4.1). By pulsing the voltage at a constant frequency, one produces several successive bubble lines. The correspondingly marked flow curves are separated by a constant time interval, and they are called "time lines".

The hydrogen bubble flow visualization apparatus is commercially available. Platinum or stainless steel wires with diameters of the order of 0.01 to 0.02 mm are used as the cathode. The anode of arbitrary shape is placed at some other location in the flow channel. The diameter of the wire determines the bubble size. A rule of thumb is that the bubble diameter is of the order of the cathode wire's diameter. The bubble size depends
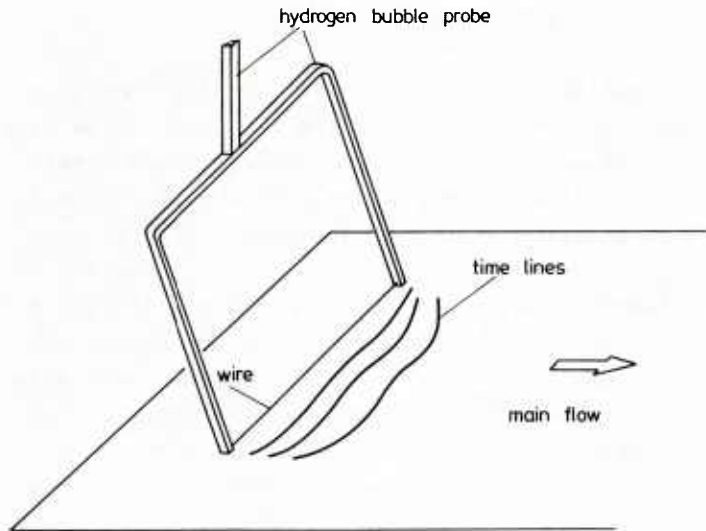
hydrogen bubble probe

time lines

wire

main flow

Fig. 4.1 a:  Generation of hydro-
gen bubble time lines
in the boundary layer
on a flat plate (adop-
ted from Smith and
Paxson [4.1]).

platinum wire
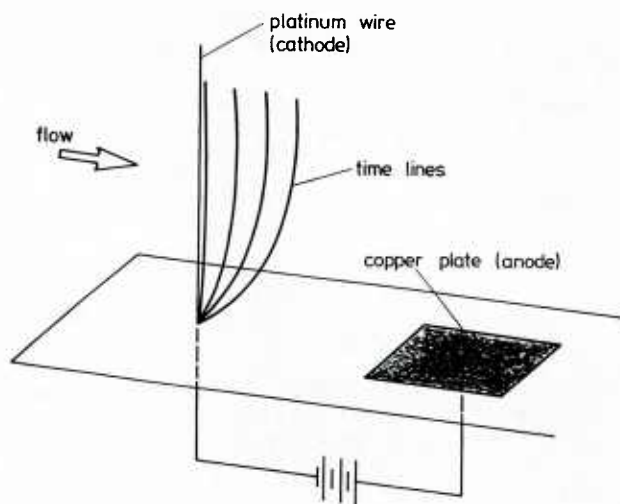(cathode)

flow

time lines

copper plate (anode)

Fig. 4.1 b:  Operation of the
system with a verti-
cal wire.

also, but to a minor extent, on the conductivity of the liquid and on the applied voltage.
Normal tap water is sufficient for the electrolytic process; values of 100 to 2oo V are
typical for the applied voltage. It is desirable to have the bubbles as small as possible.
Then, the Reynolds number associated with the rising motion (buoyancy) of the bubbles is
very low, and the rise velocity determined from Stokes' law is very small, thus minimizing
the error due to buoyancy.

In the "time line" operation, one marks a line of fluid elements whose position co-
incided at a given instant with the position of the wire. A system of time lines does not
provide information on the particle trajectories. These trajectories can be made visible
by insulating short sections of the wire. The lime lines are then interrupted at the re-
spective positions, and connecting these interruptions yields the direction of the flow.
If one uses a kinked wire, the bubbles will only develop from the kinks; and with a conti-
nuous operation of the electric system one may thus visualize streaklines (or streamlines)
instead of velocity profiles.

From several sources it follows that an angle of 65° between the illumination system

and the direction of observation is most suitable. This might have to do with the scattering characteristics of the hydrogen bubbles. Recording can be performed with conventional photography or cinematography. Video recording is of advantage for the further processing of the flow pictures, particularly if the flow pictures consist of such well defined structures like the time lines, which can easily by recognized and analyzed in respective image processing systems [4.1, 4.2]. The period of time during which the bubbles persist and can be observed in the flow is limited by the dissolution of the hydrogen bubbles in the fluid. Diffusion of the bubbles increases with Reynolds number and is very rapid in turbulent flows. The application of the method is therefore restricted to low-speed flows, maximum velocities being of the order of 20 to 30 cm/s.

The hydrogen bubble method has been developed in the early sixties [4.3 - 4.5] from an earlier technique, Wortmann's tellurium method [4.6], which uses almost the same apparatus, but with a cloud of tellurium as the tracer separating in the electrolytic reaction from a tellurium wire electrode. The disadvantage of the tellurium is that it does not dissolve in the water and, after a certain time of operation, will contaminate the water in a recirculating system. Recent progress on the hydrogen bubble method has been summarized by Matsui et al. [4.7]. The method has become a standard experimental tool for water tunnels and towing tanks, and its applications are widespread. It has enabled experimentalists to make considerable progress in studying boundary layer instabilities and in recognizing the structure of turbulent flows, see, e.g. [4.8 - 4.13] and Fig. 4.2.



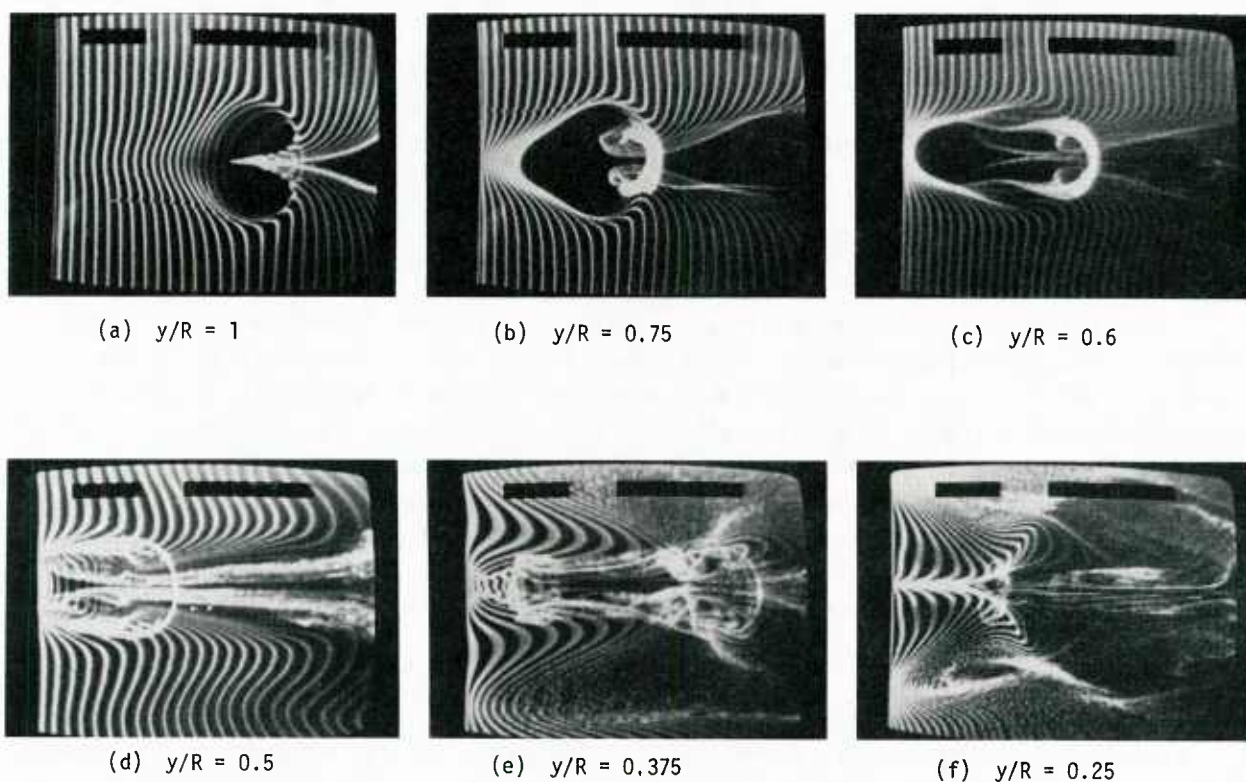| (a) y/R = 1 | (b) y/R = 0.75 | (c) y/R = 0.6 |
| (d) y/R = 0.5 | (e) y/R = 0.375 | (f) y/R = 0.25 |

Fig. 4.2: Time-line visualization of the vortex system developing from a hemisphere (of radius R) set onto a flat plate. Photographs are top views with the horizontal cathode wire at different heights y above the plate. Flow is from left to right (C.R. Smith, Lehigh University, Bethlehem, PA, USA.)

Schraub et al. [4.4] presented an extensiv discussion of the error sources when velocity fields are mapped with the hydrogen bubble method. The most significant error sources are, in brief:

- uncertainties in measuring the distance Δx between the time lines;
- averaging the velocity over the distance Δx;

- velocity defect of the bubbles due to buoyancy, particularly in accelerated flows;
- velocity defect in the fluid as caused by the wake of the cathode wire.

## 4.2   DYE PRODUCTION BY pH-INDICATORS

An electrolytic reaction may change the pH-value of the fluid in the vicinity of the electrodes. Due to the migration of positive hydrogen ions to the cathode and the formation of $H_2$ gas, the liquid becomes basic near the cathode and consequently acidic near the anode (positive electrode). A number of pH-indicators are known that can be solved in water and change color upon a specific change of the pH-value, see [4.14] and Table 4.2. For the methods discussed here, indicators are of interest that produce a visible dye for the range of pH-values reached near the cathode. With a thin cathode wire, visible time lines (see subsection 4.1) can be produced by pulsing the voltage between the electrodes. In order to avoid the simultaneous production of hydrogen bubbles at the cathode, the applied voltage must be sufficently low.

Table 4.2

pH-indicators and range of color change (data taken from [4.14] and [4.17]

| indicator | pH(1)/color | pH(2)/color |
|---|---|---|
| bromo cresol green | 4.0/yellow | 5.4/blue |
| bromo phenol red | 5.2/yellow | 7.0/red |
| bromo thymol blue | 6.0/yellow | 7.6/blue |
| meta cresol purple | 7.6/yellow | 9.2/purple |
| thymol blue | 8.0/yellow | 9.6/blue |
| phenolphtalein | 8.3/clear | 1o /red |

The indicator most commonly used in this application is thymol blue. Its use for flow visualization and the measurement of velocity profiles have been described by Baker [4.15]. The working fluid is an aqueous solution of thymol blue which is orange-yellow in an acidic environment (pH < 8.0) and turns its color to blue if the solution becomes basic (pH > 9.6). The working fluid is prepared by solving 0.01 to 0.04 % by weight of thymol blue in distilled water. A few drops of an acid, e.g. HCl, are added so that the solution is close to the point of becoming basic. The electrode system is similar to that used for the hydrogen bubble method. Applied voltages are of the order of 10 V at currents of about 1o mA or less. The optical contrast between the orange-yellow liquid and the blue dye produced at the cathode can be enhanced by employing yellow-light illumination from a sodium lamp.

The aqueous solution of thymol blue is a true solution, and the marked fluid elements are neutrally buoyant. The technique is therefore used with preference for flows that are dominated or driven by mass forces, e.g. thermal convection, stratified flows, and flows in rotating systems. Since it is costly to fill a water tunnel or towing tank with distilled water, and because it is difficult to control the pH-value in such large reservoirs, the applications are restricted to relatively small volumes of the working fluid. Another limitation is the maximum velocity or Reynolds number, because the diffusion of the dye into the surrounding fluid increases with increasing Reynolds number. The reported maximum velocity for the production and identification of time lines is about 4 cm/s.

Variations of the pH-value take place in the mixing region of two fluid flows that were given different pH-values before they mix. Color changes of a pH-indicator solved in the fluid may occur in the mixing region. This technique enabled Breidenthal [4.16] to visualize the structure of the mixing layer between two parallel fluid flows of different value of the initial velocity (Fig. 4.3). Extinction measurements allow for determining the fluid concentration in the mixing layer. Gardner [4.17] showed that the use of color is another means for such concentration measurements in mixing problems. He uses two pH-indicators (thymol blue, bromocresol green) simultaneously, so that several color changes can be observed over a wide range of the pH-value.
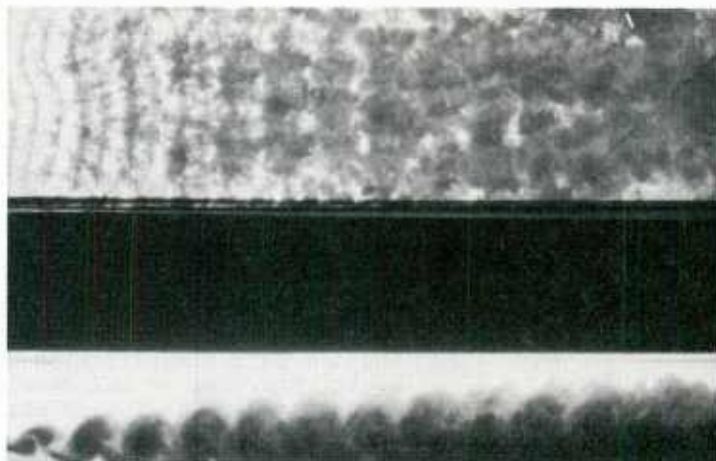


Fig. 4.3: Development of instabilities in the mixing of two fluid flows of different mean velocities, visualized by a pH-indicator. Bottom: side view; top: plan view (R. Breidenthal, University of Washington, Seattle, WA, USA).

## 4.3 PHOTOCHROMIC DYE PRODUCTION

Popovich and Hummel [4.18] reported on the use of photochromic materials in liquid solution for the production of dye by irradiation of appropriate light. The dye can be produced along a straigt line, e.g. by using a respective laser source, and the dye producing light beam can be controlled externally in time and position, so that no disturbing mechanical element has to be introduced in the flow. Photochromism is defined as the reversible transition of a chemical substance between two states, A and B, exhibiting noticeably different absorption spectra. The usual situation is that state A has high absorption rates in the ultraviolet (UV), while B is highly absorbing in the visible range of wavelengths. Therefore, the substance is invisible (transparent) in A and visible (opaque) in B. The transition $A \to B$ is stimulated by UV radiation, and it is desired that the reverse transition $B \to A$ is also possible; for the substances which are of interest here, the reverse transition is spontaneous and can be enhanced by thermal energy.
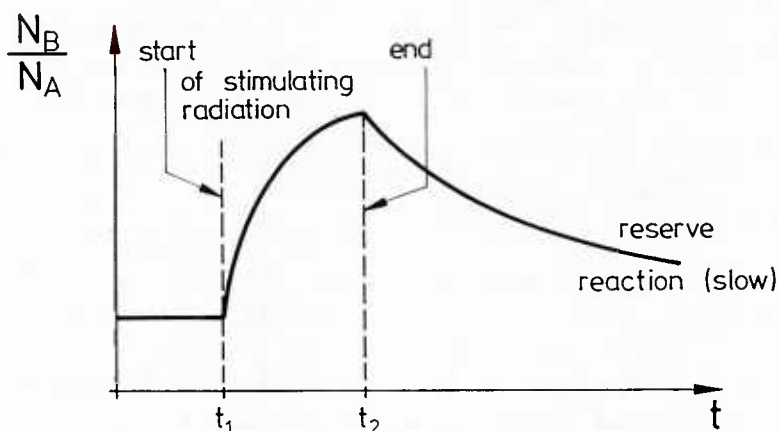


Fig. 4.4: Principle of the transition of the photochromic material between two states of different absorption, A and B. $N_A$, $N_B$ = Number of molecules in states A and B, respectively; t = time

The principle of the photochromic transition process is shown in Fig. 4.4, where the ratio of the numbers of the molecules in the two states A and B, $N_B/N_A$, is plotted as a function of time. The value of this ratio increases rapidly during the short period of incidence of the stimulating UV radiation, and it decreases slowly during the reverse

transition when the fluid regains its initial transparency. Substances exhibiting the described behaviour are components known as "pyridines", e.g. [4.18 - 4.20], and "spyranes", e.g. [4.21 - 4.24]. These substances are unsoluble in water. Solutions can be prepared with a number of organic liquids, e.g. ethanol, toluol, kerosene. Concentration of the photochromic substance should be between 0.1 and 0.2 % by weight and must be chosen accordingly to the special experimental conditions: Too low a concentration results in a weak dye production; too high a concentration can cause an unwanted temperature increase in the fluid, because only a fraction of the incident energy is used for the stimulation of state B, while the major portion of this energy is converted into heat.

Most suitable as a source for the stimulating UV radiation are a ruby laser equiped with a frequency doubler, or a $N_2$ laser which can be built at relatively low cost [4.25]. The photochromic dye, i.e., the opaque state B, is produced along the laser beam. When the laser is pulsed at equally separated time intervals, a system of time lines can be made visible (Fig. 4.5). The flow channel must be equipped with quartz windows, because normal glass is not transparent for the UV radiation.
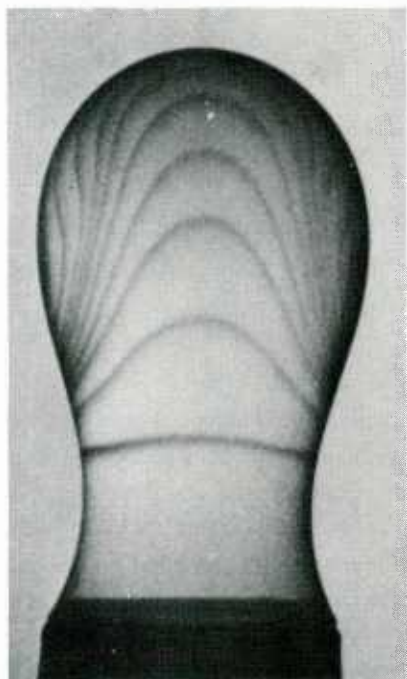


Fig. 4.5: Photochromic visualization of velocity profiles in the development of a drop (E. Marschall, University of California, Santa Barbara, CA, USA).

Experiments performed with photochromic dye are restricted by the particular properties of the solving liquid. One consequence is the limitation of the volume of the flow facility. Reported applications concern the study of the near wall region in boundary layers [4.18, 4.22], or the measurement of velocity in the interior of growing drops [4.24]. D'Arco et al. [4.23] produce in the interior of the fluid a rectangular grid by means of an appropriate illumination pattern, and they observe the deformation of this grid due to the flow; this allows for determining shear stresses in the observed plane.

## 4.4. · SMOKE WIRE

The hydrogen bubble method has its equivalent counterpart for air flows in form of the smoke wire, which has been proposed first by Yamada [4.26], and then refined and developed further by several investigators [4.27 - 4.30]. Not really smoke but oil fog is evaporated from an electrically heated wire that serves as the line source of the tracer material, like the electrode wires as described in the subsections 4.1 and 4.2. A stainless steel wire, approximately 0.1 mm in diameter, is oriented vertically or horizontally and normal to the main flow. It can be mounted on a probe or span the whole cross-section of a wind tunnel. The wire is coated with a very thin layer of kerosene. The coating is done manually by wiping the wire with a fine, small brush or a cotton-tipped app-

licator. Corke et at. [4.27] report on a device with which a drop of oil is forced down the wire by applying pressure to a small oil reservoir.
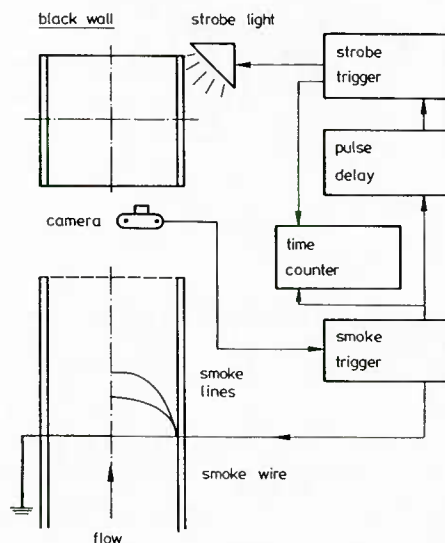


Fig. 4.6:   Schematic diagram of a smoke wire system with synchronized strobe light illumination and camera. The system is operated by pushing the camera button (after [4.29]).

With a uniform, fine coating and with the application of an equally spaced, pulsed electric heating it is possible to generate time lines equivalent to those obtained with the hydrogen bubble or thymol blue method. This is indicated in Fig. 4.6, where a schematic block diagram of such a system with synchronized strobe lieght illumination and camera is shown. The applications of the smoke wire for generating time lines, however, are rare due to the rapid diffusion of the smoke into an air stream. More frequent is the use of the wire for producing very fine smoke lines with exact spatial and temporal control. Then, the smoke line is either observed from a direction parallel to the wire; or the coating is done a little thicker, so that small oil beads or minute droplets form along the wire, and at each of the beads a smoke filament originates when the wire is heated. The spacing between such lines is influenced by the wire size, the amount of oil in the coating, and the oil surface tension.

The smoke wire is a device for introducing smoke into an air stream with much greater precision than with an injection tube, and it has already found a wide application; see, e.g. [4.31]. The smoke wire also allowed for the (so far only reported) generation of colored smoke [4.32].

## 4.5.   SPARK TRACER TECHNIQUE

The application of the smoke wire is restricted to low air velocities. At higher velocities, a mapping of the velocity field is possible by making use of an electric discharge in the air flow. The principle of the method is explained with the aid of Fig. 4.7. An electric spark discharge is generated between the two electrodes upon the application of a high voltage (several kV). The spark creates in the gas an ionized, luminous air column (plasma),whose luminosity persists for a period of time of up to 1oo $\mu$sec, depending on the discharge conditions. The plasma column can be observed while it is swept downstream by the main flow. A series of time lines can be produced by repeating the spark discharge: Since the luminous column has a smaller electric resistance than the surrounding neutral gas, a second spark produced during the lifetime of the plasma column will rather follow this preionized path than take the shortest (straight) way between the electrodes. In a series of sparks, each spark will follow and thereby re-illuminate the column,
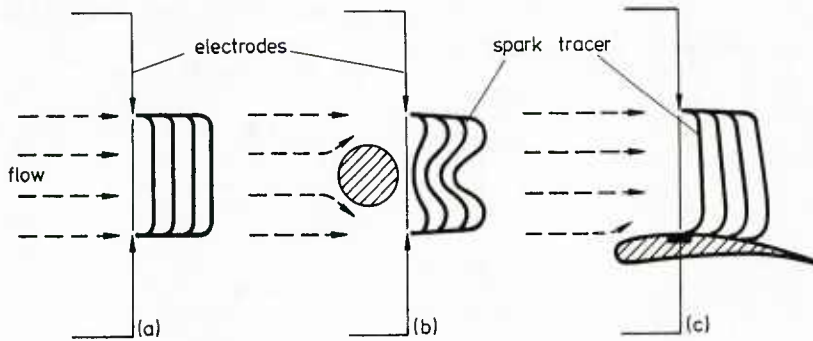
Fig. 4.7:   Principle of spark-tracer technique with spiked electrodes, applied to three
            different flows: uniform, parallel flow (a); wake flow behind sphere (b);
            flow over an airfoil profile (c).

which was generated by the first spark and swept downstream by the air flow. Photogra-
phing the series of discharge with an open-shutter  camera results in the visualization
of a system of time lines. From the known frequency of the spark series and the measured
displacement one may derive the local velocity field.

The form of the electrodes must be such that it fulfills two requirements: It should
cause a minimum of interference with the flow, and it should provide the first spark a
straight path between the electrodes, normal to the main flow. The result is a compromise
in form of electrode rods, and the discharge of each spark starts from a different point
along the rod, according to the instantaneous position of the preionized gas column. The
possible distance between the rods is several cm, with the maximum distance depending on
the air pressure and the value of the applied voltage. The appropriate spark frequency de-
pends on the mean flow velocity. It can be up to 1oo kHz. The problem then is to recharge
the high-voltage capacitors within the intervals of a few micro-seconds each. The value
of the lower limit of the spark frequency is determined by the diffusion of the ionized
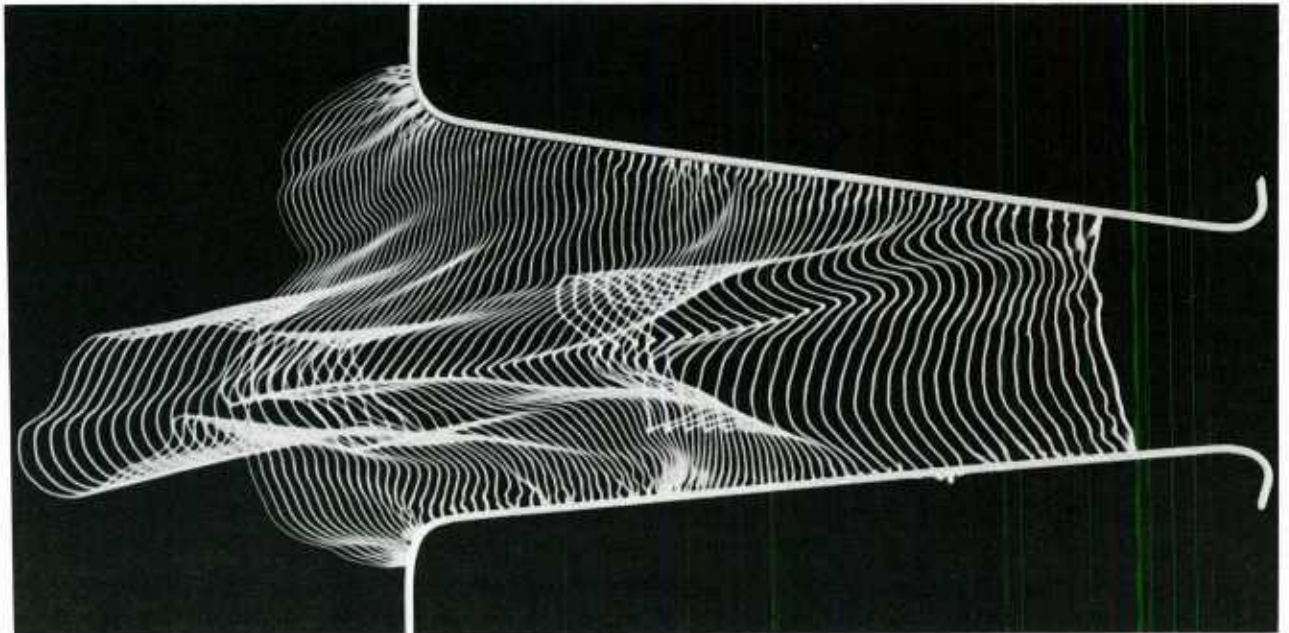gas into the ambient gas.



Fig. 4.8:   Spark-tracer technique with rod electrodes, applied to an air flow with
            strong disturbances (Impulsphysik GmbH, Hamburg, F.R. Germany).

The spark tracer technique has been developed and adapted to the study of boundary layer flow by Bomelburg et al. [4.33]. Improvements of the system are due mainly to the work of Früngel and his co-workers; see, e.g. [4.34, 4.35]. It has been used for measuring gas velocities in high-Mach number flow facilities; see, e.g. [4.38, 4.39], in model studies of turbo-machines [4.40, 4.41] and other flow machinery with swirling flow [4.42]; see also Fig. 4.8.

The application of the spark tracer method may suffer from a number of error sources, particularly in accelerated flow fields. These errors have been discussed extensively by Rudinger and Somers [4.43] and by Matsuo et al. [4.44]. The plasma column as the tracer is lighter than the working fluid (air) and therefore has a different inertia. A relative motion of the ionized column with respect to the mean flow transforms the tracer into a vortex. This vortex consumes energy from the main flow and it may induce an additional velocity component to the tracer. The velocity lag between tracer and flow increases with the magnitude of the acceleration and with the density difference between tracer and fluid. In both references it is found that the relative errors, in extreme situations, can exceed 5o %.

## References

4.1.  Smith, C.R.; Paxson, R.D.: A technique for evaluation of three-dimensional behaviour in turbulent boundary layers using computer augmented  hydrogen bubble-wire flow visualization. Exp. Fluids 1 (1983), 43-49.

4.2.  Lu, L.J.; Smith, C.R.: Image processing of hydrogen bubble flow visualization for determination of turbulence statistics and bursting characteristics. Exp. Fluids 3 (1985), 349-356.

4.3.  Clutter, D.W.; Smith, A.M.O.: Flow visualization by electrolysis of water. Aerospace Eng. 2o (1961), 24-27, 74-76.

4.4.  Schraub, F.A.; Kline, S.J.; Henry, J.; Runstadler, P.W., Jr.; Littell, A.: Use of hydrogen bubbles for quantitative determination of time-dependent velocity fields in low-speed water flows. J. Basic Eng. 87 (1965), 429-444.

4.5.  Davis, W.; Fox, R.W.: An evaluation of the hydrogen bubble technique for the quantitative determination of fluid velocities within clear tubes. J. Basic Eng. 89 (1967), 771-781.

4.6.  Wortmann, F.X.: Eine Methode zur Beobachtung und Messung von Wasserströmungen mit Tellur. Z.f. Angew. Physik 5 (1953), 2o1-2o6.

4.7.  Matsui, T.; Nagata, H.; Yasuda, H.: Some remarks on hydrogen bubble technique for low speed water flows. In [1.3], pp. 215-220, 1979.

4.8.  Kim, H.T.; Kline, S.J.: Reynolds, W.C.: The production of turbulence near a smooth wall in a turbulent boundary layer. J. Fluid Mech. 5o (1971), 133-16o.

4.9.  Bippes, H.; Görtler, H.: Dreidimensionale Strömungen in der Grenzschicht an einer konkaven Wand. Acta Mech. 14 (1972), 251-267.

4.1o.  Offen, G.R.; Kline, S.J.: Combined dye-streak and hydrogen bubble visual observation of a turbulent boundary layer. J. Fluid Mech. 62 (1974), 223-239.

4.11.  Rockwell, D.; Kniseley, C.: The organized nature of flow impingement upon a corner. J. Fluid Mech. 93 (1979), 413-432.

4.12.  Kasagi, N.; Hirata, M.; Nishino, K.: Streamwise pseudo-vortical structures and associated vorticity in the near-wall region of a wall-bounded turbulent shear flow. Exp. Fluids 4 (1986), 3o9-318.

4.13.  Acarlar, M.S.; Smith, C.R.: A study of hairpin vortices in a laminar boundary layer. Part 1 and 2. J. Fluid Mech. 175 (1987), 1-83.

4.14.  Quraishi, M.S.; Fahidi, T.Z.: A flow visualization technique using analytical indicators: theory and some applications. Chem. Eng. Sci. 37 (1982), 775-78o.

4.15.  Baker, D.J.: A technique for precise measurement of small fluid velocities. J. Fluid Mech. 26 (1966), 573-575.

4.16.  Breidenthal, R.: Structure in turbulent mixing layers and wakes using a chemical reaction. J. Fluid Mech. 1o9 (1981), 1-24.

30

4.17. Gardner, R.A.: Colometric flow visualization. Exp. Fluids 3 (1985), 33-34.

4.18. Popovich, A.T.; Hummel, R.L.: A new method for non-disturbing turbulent flow measurements very close to a wall. Chem. Eng. Sci. 22 (1967), 21-25.

4.19. Iribarne, A.; Frantisak, F.; Hummel, R.L.; Smith, J.W.: An experimental study of instabilities and other properties of a laminar pipe jet. AIChE J. 18 (1972) 689-698.

4.20. Lavallee, H.C.; Popovich, A.T.: Fluid flow near roughness elements investigated by photolysis method. Chem. Eng. Sci. 29 (1974), 49-59.

4.21. Humphrey, J.A.; Smith, J.W.; Davey, B.; Hummel, R.L.: Light-induced disturbances in photochromic flow visualization. Chem. Eng. Sci. 29 (1974), 3o8-312.

4.22. Kondratas, H.M.; Hummel, R.L.: Application of the photochromic tracer technique for flow visualization near the wall region. In [1.5], pp. 387-391, 1982.

4.23. D'Arco, A.; Charmet, J.C.; Cloitre, M.: Nouvelle technique de marquage d'écoulement par utilisation de molécules photochromes. Revue Phys. Appl. 17 (1982), 89-93.

4.24. Hutchins, J.; Johnson, G.; Marschall, E.: Flow visualization in two-phase flow. In: Measuring Techniques in Gas-Liquid Two-Phase Flows (eds. J.M. Delhaye, G. Cognet), pp. 91-1o2, Springer-Verlag, Berlin, 1984.

4.25. Bergmann, E.E.: Compact TEA $N_2$ laser. Rev. Sci. Instrum. 48 (1977), 545-546.

4.26. Yamada, H.: Instantaneous measurement of air flows by smoke wire technique. (in Japanese). Nippon Kikai Gakkai Ronbunshu 39 (1973), 726-729.

4.27. Corke, T.; Koga, D.; Drubka, R.; Nagib, H.: A new technique for introducing controlled sheets of smoke streaklines in wind tunnels. ICIASF '77 Record (1977), 74-8o.

4.28. Nagib, H.M.: Visualization of turbulent and complex flows using controlled sheets of smoke streaklines. In [1.3], pp. 257-263, 1979.

4.29. Torii, K.: Flow visualization by smoke wire technique. In [1.3], pp. 251-256,1779.

4.3o. Yamada, H.: Use of smoke wire technique in measuring velocity profiles of oscillating laminar air flows. In [1.3], pp. 265-27o, 1979.

4.31. Mueller, T.J.; Batill, S.M.: Experimental study of separation on a two-dimensional airfoil at low Reynolds numbers. AIAA J. 2o (1982), 457-463.

4.32. Sieverding, C.H.; Van den Bosche, P.: The use of colored smoke to visualize secondary flows in a turbine-blade cascade. J. Fluid Mech. 134 (1983), 85-89.

4.33. Bomelburg, H.J.; Herzog, J.R.; Weske, J.R.: The electric spark method for quantitative measurements in flowing gases. Z. Flugwiss. 7 (1959), 322-329.

4.34. Früngel, F.; Thorwart, W.: Spark tracing method progress in the analysis of gaseous flows. In: Proceed. 9th Int. Congess on High-Speed Photography (eds. W.H. Hyzer, W.G. Chace), pp. 166-17o, SMPTE, New York, 197o.

4.35. Früngel, F.: High-frequency spark tracing and application in engineering and aerodynamics. In: Proceed. 12th Int. Congress on High-Speed Photography, SPIE Vol. 97, 291-3o1, 1977.

4.36. Asanuma, T.; Tanida, Y.; Kurihara, K.: On the measurement of flow velocity by means of spark tracing method. In [1.3], pp. 227-232, 1979.

4.37. Nakayama, Y.: Okitsu, S.; Aoki, K.; Ohta, H.: Flow direction detectable spark method. In [1.3], 239-244 1979.

4.38. Kimura, T.; Nishio, M.; Fugita, T.; Maeno, R.: Visualization of shock wave by electric discharge. AIAA J. 15 (1977), 611-612.

4.39. Matsuo, K.; Ikui, T.; Yamamoto, Y.; Setoguchi, T.: Measurements of shock tube flows using a spark tracer method. In [1.3] pp. 233-238, 1979.

4.4o. Fister, W.; Eickelmann, J.; Witzel, U.: Expanded application programs of the spark tracer method with regard to centrifugal compressor impellers. In [1.5], 1o7-12o, 1982.

4.41. Ohki, H.; Yoshinaga, Y.; Tsutsumi, Y.: Visualization of relative flow patterns in centrifugal impellers. In [1.6], pp. 723-727, 1985.

4.42. Nakayama, Y.; Aoki, K.; Ohta, H.; Wakatsuki, M.: Spark method visualization of the swirling flow mixing process. In [1.6], pp. 7o7-711, 1985.

4.43. Rudinger, G.; Somers, L.M.: Behaviour of small regions of different gases carried in accelerated gas flows. J. Fluid Mech. 7 (196o), 161-176.

4.44. Matsuo, K.; Setoguchi, T.; Yamamoto, Y.: The error in measuring an accelerated flow velocity by a spark tracer method. Bull. JSME 24 (1981), 1168-1175.

## 5.  LIGHT SHEET METHODS

In the previous chapters, no particular requirements were made with respect to the illumination system. In this chapter, methods are discussed for which the illumination is provided in form of a plane, thin sheet, so that only the tracer material within thin sheet or slice is illuminated. Illumination in form of such a sheet can be applied to the methods already discussed, but it also allowed for the development of new techniques, e.g. speckle velocimetry and laser-induced fluorescence, both of which are included in this chapter.

### 5.1.  GENERATION OF A LIGHT SHEET

A light sheet can be produced with a conventional lamp (mercury lamp, halogen lamp, spot light). A much better way is to expand the beam from a powerful laser by means of a cylindric lens in one plane. The thickness of such a sheet can be made much smaller than 1 mm. Observation of the flow pattern in the illuminated plane is normal to this sheet or under a certain angle to it (Fig. 5.1). Illumination by a light sheet can be applied to both dye and smoke visualization, and it is most appropriate for recognizing vortical structures in these flows (Fig. 5.2). The light sheet technique and its use in convential
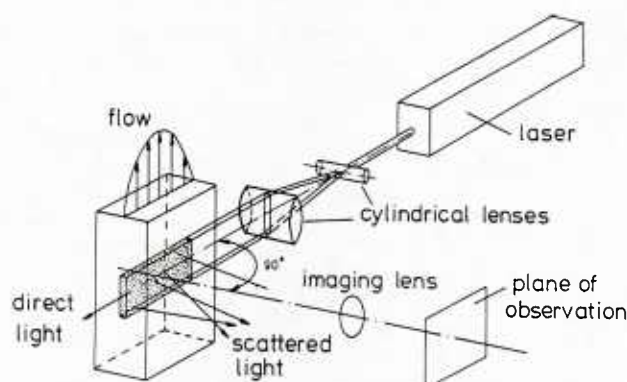


Fig. 5.1:  Generation of a light sheet in a flow by expanding a laser beam in one plane by means of cylindrical lenses.

visualization systems have been reviewed, e.g., by Véret [5.1], and the reported applications are numerous. Koga et al. [5.2] describe how the laser light for the sheet can be directed to the appropriate position by a fiber optics.

Flow facilities have been designed particularly for the application of a light sheet normal to the main flow direction. These special wind tunnels are, to a certain degree, filled with either smoke or vapor, and the technique is called a smoke screen or vapor screen, respectively. They allow, e.g., for the visualization of trailing vortices, which separate from test models. A schematic view of the test section, light source, vapor (or smoke) screen, and recording camera is shown in Fig. 5.3.

While the application of smoke tunnels is restricted to subsonic flow [3.4], vapor screens are very often produced to observe supersonic flows. The supersonic tunnel must be run with moist air; the air cools as it expands through the nozzle, and the moisture condenses to form a fog in the test section. The uniform distribution of fog in a cross section normal to the tunnel axis is disturbed due to the wake from a test model. McGre-

gor [5.5] has investigated the rate of humidity required to produce a satisfactory screen at Mach numbers up to M = 2, and as a function of tunnel pressure and temperature. Snow and Morris [5.6] systematically investigated the operational conditions of the vapor screen. They also describe a periscope system for observation so that it is not necessary to have the camera inside the tunnel.
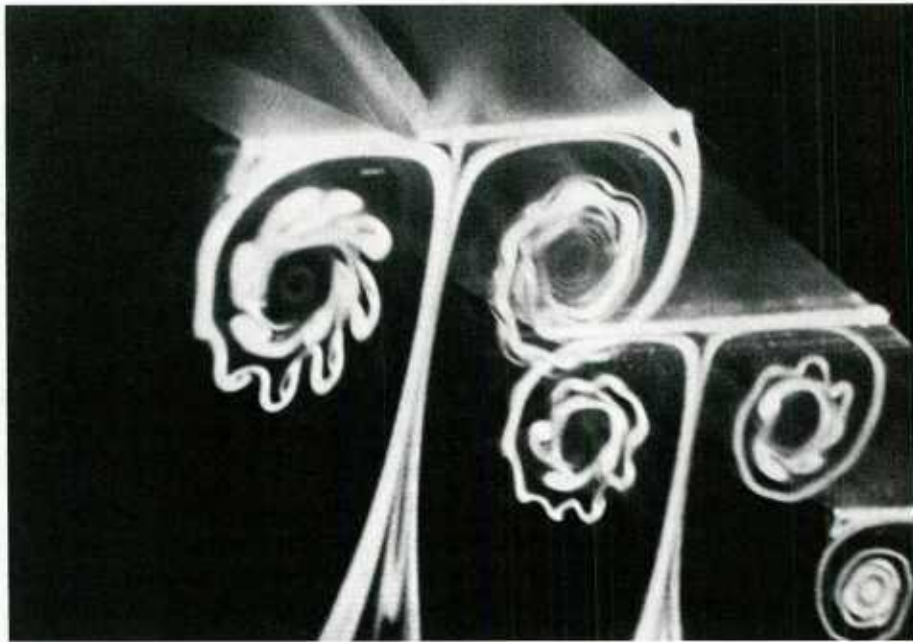


Fig. 5.2:   Smoke visualization of leading-edge vortices on a swept delta wing; illumination by light sheet (R.C. Nelson, University of Notre Dame, IN, USA [5.4]).
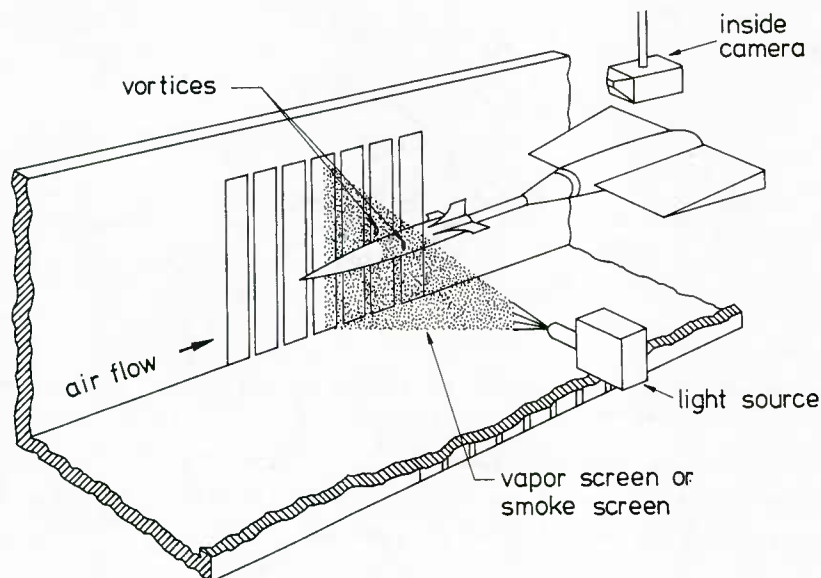


Fig. 5.3:   Illumination by light sheet in a vapor tunnel or smoke tunnel (adopted from Snow and Morris [5.6]).

The light sheet plays an important role in measuring the velocity of tracer particles in a flow from a photographic record. In this case it is mandatory to use a pulsed light source (flash lamp, electric spark, ruby laser) with a definite pulse length, and, if needed, with the possibility of generating a series of such pulses (stroboscope). With the light sheet, one visualizes the two velocity components in the plane of the sheet. Emrich [5.7] calls the record of such a plane a "time window", within which the velocity can be determined simultaneously for many points (this is also called a whole-field record). Shifting the sheet in a direction normal to its plane enables one to scan a three-dimensional flow, provided that the flow is stationary over the test period. The third

velocity component, normal to that plane, is not recovered in this way. This would need to illuminate light sheets perpendicular to the first set of sheets.

The tracer particles in the light sheet are observed or photographed in a direction approximately normal to the illuminated plane. If one takes a time exposure, each particle appears in the image plane as a streak whose length is proportional to the average local velocity (Fig. 5.4). This simple way of measuring a velocity vector is associated to a number of technical shortcomings and possible errors, e.g., precision and control of the exposure time; optical parallax and distortion in viewing the illuminated plane; inability to determine the flow direction. Stroboscopic illumination results in a series of particle images, usually three or four [5.7, 5.8], indicating the particle velocity by magnitude and direction.

A new means for improved data evaluation is image processing of the particle-streak record. Dimotakis et al. [5.1o] have scanned and digitized the particle-streak pattern from the photographic negative so that this pattern can be reproduced as a digital image. It is then possible to apply special computer programs for displaying the velocity distribution, or for manipulating the data, e.g. superimposing a constant velocity, deriving stream function, vorticity, or other flow parameters, see, e.g. [5.11 - 5.13].



Fig. 5.4: Time exposure of the vortex formation in the water flow around a rotating cylinder. The arrow indicates the direction of rotation. Tracer particles: lycopodium; Re = 1o$^3$ (M. Coutanceau, University of Poitiers, France).

5.2  SPECKLE VELOCIMETRY

The techniques of speckle photography, which are used in solid state mechanics for measuring surface deformations, have been adopted to the measurement of flow velocity in fluids seeded with tracer particles. This particular application of speckle photography requires, in most cases, the use of a light sheet. The technique is a special recording method, rather than a direct visualization method. It allows for both quantitative measurement of the two velocity components in the illuminated plane, and the generation of a visual pattern in form of iso-velocity contours. This method has been developed in a number of laboratories, and it is interesting to note that the first results from the different groups have been reported apparently all in the same year [5.14 - 5.17].
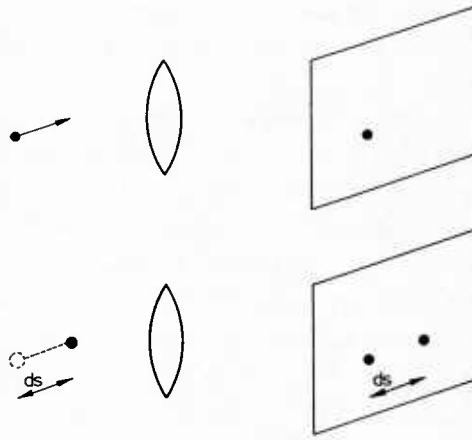
Fig. 5.5: Displacement of an object point by amount ds and recording by a photographic double exposure.

The principle of the method is explained by considering an object point which is imaged onto a recording plane (Fig. 5.5). The object point is displaced by a small distance ds and, under the assumption of an imaging ratio of 1:1, the image point is displaced in the same direction and by the same amount ds. In a photographic double exposure, one exposure taken before and the second after the displacement, the image point appears twice, separated by ds as shown in Fig. 5.5. In the application to a fluid flow, the object point represents a single tracer particle moving along the flow with the velocity w. The displacement of the particle between the two photographic exposures is ds = w · dt, where dt is the time interval separating the two exposures. With known time interval dt, the determination of the velocity w requires the measurement of the distance ds. Speckle photography is a means for measuring both direction and magnitude of small in-plane displacements for a whole field of view. The principle of such measurement will be explained next.
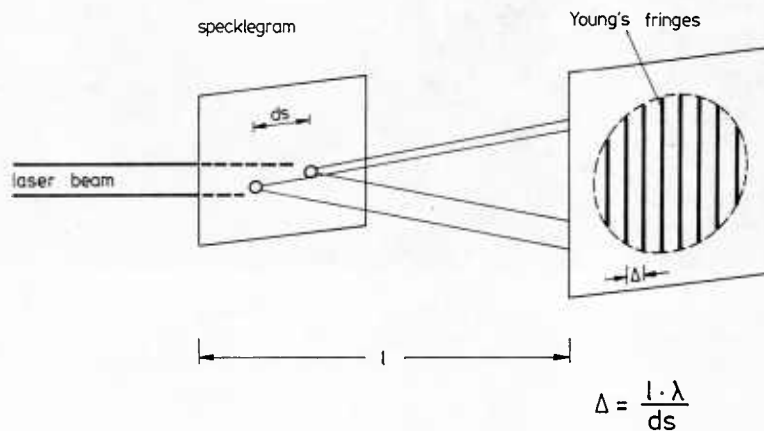


$$\Delta = \frac{l \cdot \lambda}{ds}$$

Fig. 5.6: Illumination of the photographic double exposure of Fig. 5.5 ("specklegram") by a thin laser beam and formation of Young's fringes in a plane of observation.

After development of the double exposure the two image points appear on the plate as two bright spots on a dark background. These two points are illuminated from behind with a thin laser beam (Fig. 5.6). For the propagation of the light in the space to the right of the plate, the two illuminated spots can be considered as two point sources; they emit light into two cones ("halo"). In the overlapping regime of the two cones the light from the two sources can interfere. Parallel and equally spaced interference fringes ("Young's

fringes") can be observed in a plane normal to the optical axis and at a distance $\ell$ from the two sources. The fringes are normal to the direction of ds and separated by the spacing $\Delta$:

$$\Delta = \frac{\ell \cdot \lambda}{ds} \qquad .$$

$\lambda$ is the laser wave length. The measurement of the vector $\vec{ds}$ is thereby reduced to the measurement of the fringe direction and fringe spacing in a system of Young's interference fringes.

The laser beam in the set-up of Fig. 5.6 illuminates on the developed plate a small circular area of diameter $\leq$ 1 mm. If, as it has been assumed here, only one pair of particle images is present in that circular area, the flow has been seeded obviously at a low seeding rate so that it is possible to identify or to image individual tracer particles. This is not a common situation. At higher seeding rates the circular area may include a number of pairs of particle images. The recording by the double exposure might not even be an imaging process, but a process of multiple-interference caused by the scattering of light from the tracer particles. Then, the result of the recording is a real speckle pattern, a granular structure consisting of a distribution of "speckles". In the following, the term "speckle" is used, and it is understood that the speckle is a particle image when the seeding rate was low.

Hence, the small circular area illuminated by the laser beam includes a number of pairs of speckles which are distributed randomly in that area (Fig. 5.7). If all these speckles were displaced by the same amount and in the same direction, the resulting sys-
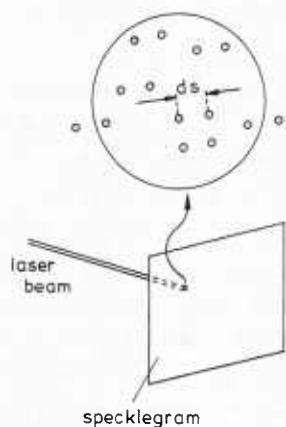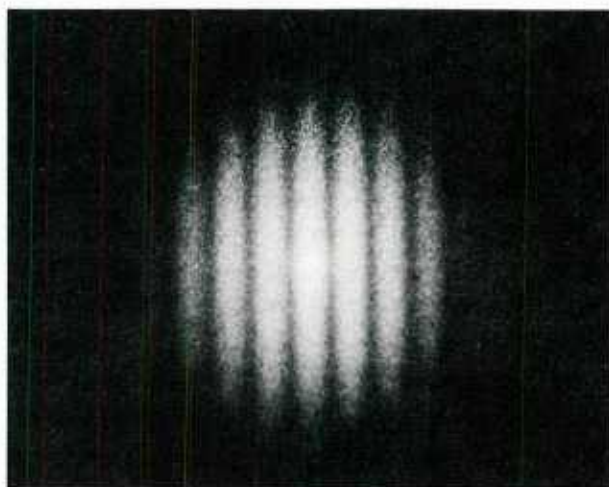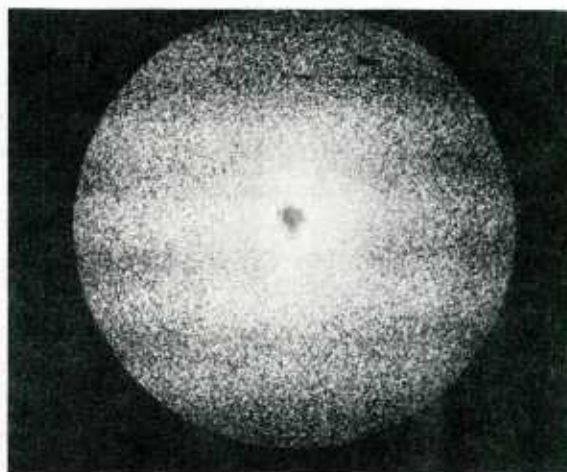


Fig. 5.7: Random distribution of speckle pairs in the specklegram. The circular area of diameter < 1 mm is illuminated by the scanning laser beam.



(a)　　　　　　　　　　　　　　　(b)

Fig. 5.8: Young's fringe pattern with high (a) and low (b) degree of correlation

tem of Young's fringes will be the same as if only one pair had been illuminated. But if the illuminated speckles have not all experienced the same displacement, different systems of Young's fringes will be generated, and they overlap each other. The pattern is to a certain degree decorrelated, the fringe system is of reduced contrast or visibility (Fig. 5.8). If it is still possible to identify a dominating frequency in the fringe pattern, i.e., to measure a mean value of the fringe spacing $\Delta$, then one attributes a mean value of the displacement ds to all speckles appearing in the circular area. A reduction in size of this area, e.g., by focusing the laser beam with a lens, is desirable for improving the local resolution.

Single speckles illuminated near the edge of the circular area (Fig. 5.7) contribute to the noise level of the signal, i.e., they reduce the fringe visibility.

The discussion of a single pair of speckles in the field can serve to explain some limitations of the method. Each speckle has a certain diameter $d_p$ whose value can be derived from diffraction theory (see e.g. Françon [5.18]). $d_p$ is equivalent to the particle image diameter when the method is explained in terms of an imaging process. The lower limit for the displacement ds that can be measured in this way is given by the requirement $ds \geq d_p$. There exists also an upper limit when the fringe spacing $\Delta$ becomes too small, i. e., when the fringe system becomes too narrow. A rule of thumb is that this upper limit is reached for $ds \approx 2o \cdot d_p$. From these two values follows the range of tracer velocities that can be measured in an experiment with given time interval of the double-exposure.

Most of the flow experiments are performed with a light sheet as shown in Fig. 5.1. Very suitable for taking the double exposure is the use of a double-pulsed ruby laser beam expanded in one plane by a cylindrical lens. The width of the single pulses as well as the time interval between pulses can be controlled short enough to allow for a tolerable value of the displacement to be measured. The concentration of tracer particles in the flow determines whether the method is working in the particle-image-mode (low concentration) or as real speckle photography (high concentration); see, e.g. [5.19]. Particle concentration and particle size have an essential influence on the amount of light available for taking the double exposure, and this problem is probably the most servere restriction for the application of speckle velocimetry. The light intensity distribution is quite different from laser Doppler velocimetry, where all the light is concentrated in the focal point, i.e. the measuring volume. Here, however, the laser light is expanded in a sheet, and the incident intensity which is then scattered from an individual particle is by orders of magnitude lower than in laser Doppler systems. The low sensitivity of photographic material to radiation in the red (particularly the ruby-laser wavelength!) contributes to this intensity problem. Consequently, the reported applications of speckle velocimetry were either cases with relatively large tracer particles, or flows of low velocity, so that the duration of each light pulse was relatively long.

Besides by using powerful laser sources, the intensity problem can be improved by taking multiple-exposures instead of a double-exposure [5.2o]. This is also of advantage for the clarity of the Young's fringes, but the method is then restricted to flow fields with smooth and moderate velocity changes. Another possibility is to operate the method in forward scattering [5.21], but this is a possible solution for plane flow fields only.

Illumination for the recording can be provided also with a white source [5.22,5.23]; since the use of such a source merely excludes the possibility of interference, the recording is then strictly a particle-image process.

The analysis of the developed double-exposure (which is called a "specklegram") with the method described in Fig. 5.6 is referred to as the "point-by-point" reconstruction of
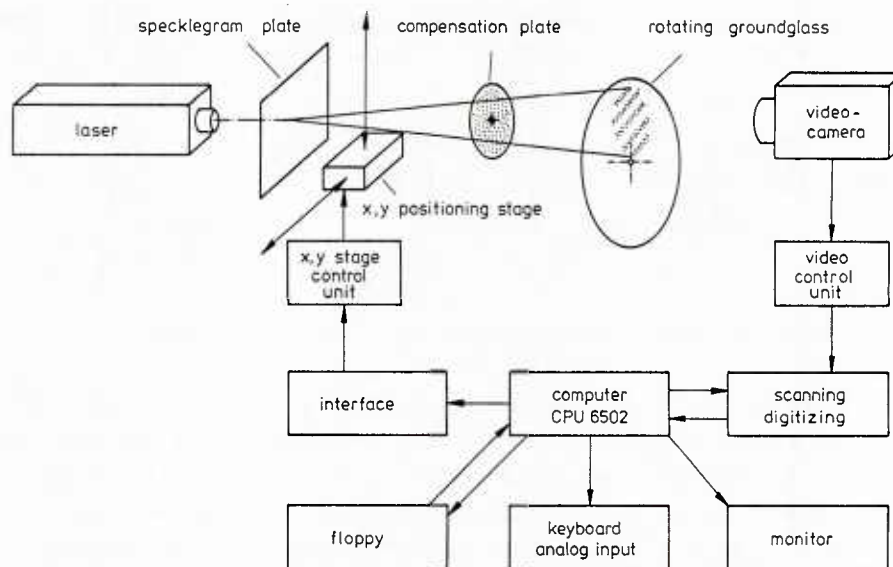
Fig. 5.9: System of fully automated evaluation of a specklegram (Erbeck [5.25]).

the plane velocity field. The specklegram is scanned point-by-point with the laser. For each illuminated point one obtains a pattern of Young's fringes. From the measured fringe spacing and fringe direction one determines the two velocity components in the respective point of the illuminated plane. The information stored in the specklegram is a very dense distribution of data on displacement vectors or velocity. The rational analysis of such an extended data field requires the use of an automated processing system. Meynart [5.24] describes an interactive system that needs the help of an operator. A fully automated system for the point-by-point scanning has been developed by Erbeck [5.25]: Each system of Young's fringes is digitized; fringe spacing and direction are determined by a computer which also controls the scanning by the laser beam (Fig. 5.9). In this system, optical elements are incorporated that compensate for the radial decrease of mean light intensity in the fringe system (halo) and for the formation of secondary speckles.

From the fringe pattern it is not possible to determine the particle direction (positive or negative). This difficulty is overcome by means of an additional displacement of the recording plate between the two exposures; see, e.g. [5.26]. This technique of image shifting is equivalent to the frequency shift in laser Doppler anemometry.

As for any light sheet method, the velocity component normal to the illuminated plane is not recovered. If a particle moving in this third direction is in the plane of the sheet at the instant of one of the two exposures, it will appear as a single image (or speckles in the double-exposure. The light scattered from such particles contributes to the ground noise and reduces the visibility of the fringes, like a speckle at the edge of the circular area in Fig. 5.7. Signal noise or decorrelation is also generated by turbulent fluctuations in the velocity vector, as well as by a nonuniform distribution in particle size and concentration. At the same time, this noise carries a certain information, and attempts have been made to decode this information for obtaining, additionally to the measurement of mean velocity, data on turbulence characteristics [5.27] or particle size distribution [5.28].

In addition to the measurement of the velocity vector, the speckle technique allows for a direct visualization of the velocity field. This analysis is performed by spatial filtering of the developed double-exposure ("specklegram"). A schematic representation of the set-up for this reconstruction process is shown in Fig. 5.10. The specklegram is illuminated with an expanded laser beam, and it is imaged by means of a lens in a plane ("Fourier plane") where, in the aforementioned point-by-point analysis, the pattern of
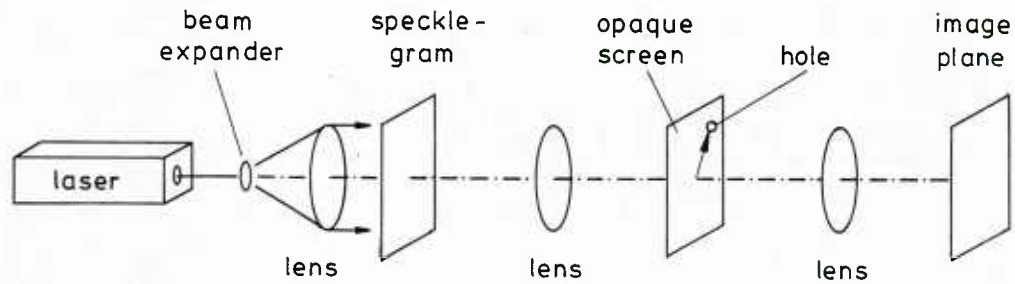
Fig. 5.1o:  Arrangement for the spatial filtering of a specklegram.

Young's fringes had been observed. An opaque screen is placed in this plane that has a transparent hole at an off-axis location. A small amount of the light can pass through the hole, and a second lens forms an image of the specklegram in the final image plane. Since every point of the specklegram is illuminated by the expanded laser light, the Fourier plane is covered by an infinite number of overlapping fringe systems. Light can pass through the hole if the hole, in the Fourier plane, is located on a bright interference fringe. It turns out that this requirement is met by such systems which are normal to the radius combining the hole and the axis, and for which the ratio of the distance from the hole to the optical axis and the fringe spacing is an integer number. As a consequence, only such points appear illuminated in the (final) image plane for which the flow velocity in the respective object points of the flow plane is of a certain value and direction. The points illuminated in the image plane lay on fringes or contours of equal velocity component. The velocity difference from fringe to fringe (not to confuse with the Young's fringes!) is constant. The amount and the direction of the velocity component, visualized by means of these "equi-velocity fringes" depends on the location of the hole in the Fourier plane, see, e.g. [5.21, 5.23, 5.29].
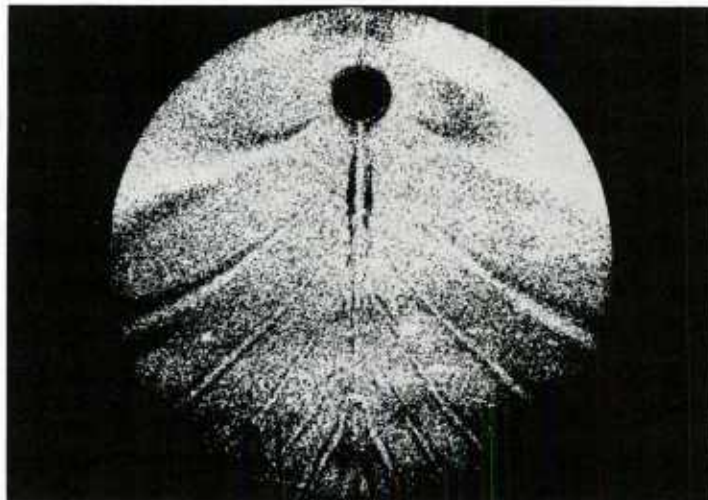


Fig. 5.11:  Equi-velocity fringes in the field of an internal gravity wave behind a cylinder moving vertically through stratified saltwater. Visualization by spatial filtering of the specklegram (Gärtner et al. [5.21]).

    Fig. 5.11 shows a system of equi-velocity fringes in the field of a plane internal gravity wave which has been produced by a cylinder moving upwards through density-stratified salt-water [5.21]. The observable velocity-fringes are at the same time curves of equal phase in the wave system. Locating the hole at a different position in the Fourier plane results in visualizing a different component. This reconstruction by spatial filtering suffers from the low light intensities that have to be managed.

Application of speckle photography for velocity measurements is not yet widespread.

An apparent limitation is the availability of an ultra-short and intensive light source for generating the double-exposure. This problem is the smaller the lower the flow velocity to be measured;this fact explains successful applications of the method to Bénard convection [5.29, 5.30] and the low-speed flow in a towing tank [5.31, 5.32].However, the general suitability of speckle velocimetry for gas flows with velocities being not very small has also been verified [5.33 - 5.35].

## 5.3   LASER INDUCED FLUORESCENCE

Fluorescent tracer materials have been used since quite a number of years for enhanced flow visualization. These materials emit a characteristic, fluorescent radiation upon excitation by light of an appropriate wavelength. The wavelength of fluorescence is different from the wavelength necessary for excitation, which is typical for inelastic scattering. The fluorescent radiation, when suitably analyzed, may contain information on the local density, species concentration, pressure, temperature, and even velocity (Doppler effect). When the exciting laser light is provided in form of a plane sheet, a selected plane in the flow can be visualized, and data on the two-dimensional (plane) distribution of one or several of the mentioned quantities can be generated. Taking records or photographs through a narrow optical filter that passes only the wavelengths of fluorescence allows for blocking off all the noise generated by the incident (exciting) light.

Laser-induced fluorescence measurements with a light sheet from an argon ion laser have been performed by Koochesfahani and Dimotakis [5.36] for determining local concentration values in the mixing of two liquid streams. However, the majority of applications of planar laser-induced fluorescence is in the field of compressible, usually supersonic gas flow at relatively low density levels. The fluorescing trace material, with which the gas is seeded, is either molecular iodine, $I_2$ [5.37 - 5.44], or atomic sodium, Na [5.45 - 5.47]. Under the assumption, that the tracer molecules are uniformly distributed in the flowing gas, one may conclude from the recorded light intensity onto the local value of the gas density in the thin volume of the light sheet.  McDaniel et al. [5.40] measured density fluctuations in a supersonic nozzle flow; Ackermann et al. [5.43] studied the possibility of measuring pressure fluctuations; the Doppler shift of the fluorescent signal has been used for velocity measurements, e.g., by Zimmerman and Miles [5.46], Hiller and Hanson [5.42], and Hassa et al. [5.44]. Temperatures have been measured in flames (see below).

Iodine is an aggressively reacting tracer material, incompatible with many metals, and it has been used as a tracer in supersonic flows of helium and nitrogen with which it can be mixed easily at room temperature. The emitted fluorescence is yellow and can be excited with the green (514.5 nm) line of an argon ion laser. The signal intensity is not uniquely dependent on the gas density (or number of $I_2$ molecules in the control volume), but it is also influenced by pressure and temperature. McDaniel [5.41] found that the latter dependence can be suppressed by detuning the laser from the absorption frequency, however with the disadvantage of decreasing the mean signal amplitude. Compared with iodine, sodium has a much higher signal intensity and the additional advantage, that the molecular mass of sodium vapor is approximately the same as that of the gases to which it is applied (nitrogen or helium). But the seeding of these working gases with sodium is a much more complicated procedure than the seeding with iodine [5.45]. In both cases, seeding rates in terms of mass concentration are in the order of $10^{-3}$ to $10^{-4}$.

The radical OH produced in many flames is a reactant which itself is fluorescent. A number of experiments have been reported in which OH has been excited with radiation wavelengths in the visible and near ultraviolet part of the spectrum [5.48 - 5.51]. Since the greatest interest is in turbulent flames, the excitation should be performed with a pulsed dye laser in order to freeze the turbulent fluctuations. The signal intensity of

the OH fluorescence is much lower than the intensity in the iodine or sodium experiments, and it is therefore necessary to apply an image intensifying system whose output can be digitized and displayed on a monitor (Fig. 5.12). Values of the relative OH-concentration can be extracted from such a display. Determination of the absolute concentration requires at least one single-point calibration with another method.
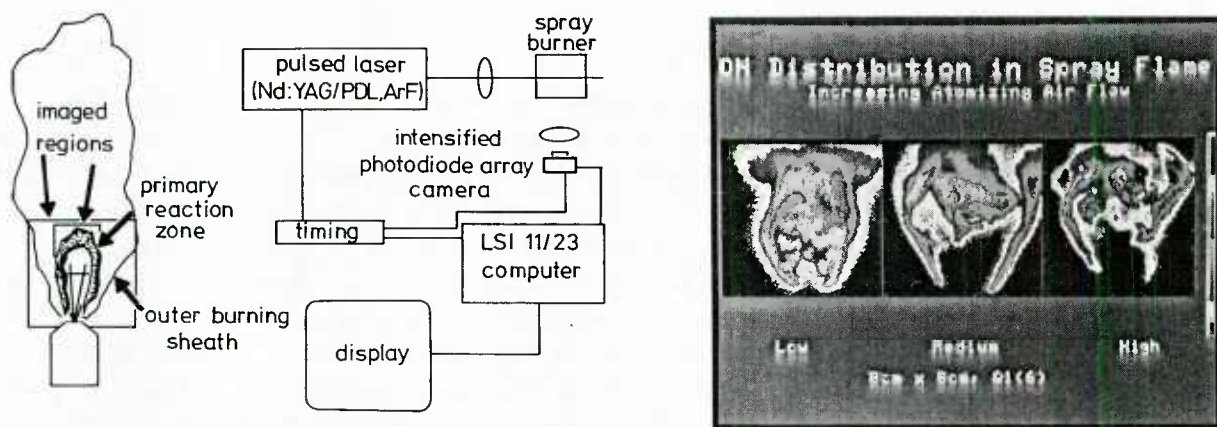


Fig. 5.12: Set-up for measuring a spray flame with laser-induced fluorescence (left). The beam from a pulsed Nd:YAG-laser is expanded in a plane. A photodiode array camera records the fluorescent scattered signal which is displayed on a monitor (right). (R.K. Hanson, Stanford University, Ca, USA)

Besides OH, fluorescence from nitric oxide [5.52] and the radical CH [5.53] have been used for concentration measurements.

## References

5.1.   Véret, C.: Flow visualization by light sheet. In [1.6], pp. 1o6-112, 1985.

5.2.   Koga, D.J.; Abrahamson, S.D.; Eaton, J.K.: Development of a portable laser sheet. Exp. Fluids 5 (1987), 215-216.

5.3.   Philbert, M.; Beaupoil,R.; Faleni, J.-P.: Application d'un dispositif d'éclairage laminaire à la visualization des écoulements aérodynamiques en soufflerie par émission de fumée. Rech. Aerosp. no. 1979-3 (1979), 173-179.

5.4.   Nelson, R.C.: The role of flow visualization in the study of high-angle-of-attack aerodynamics. Progress in Astronautics and Aeronautics 1o4 (1986), 43-88.

5.5.   McGregor, I.: The vapor-sceern method of flow visualization. J. Fluid Mech. 11 (1961), 481-511.

5.6.   Snow, W.L.; Morris, O.A.: Investigation of light source and scattering medium related to vapor-screen flow visualization in a supersonic wind tunnel. NASA TM 8629o, 1984.

5.7.   Emrich, R.J.: Flow field measurement by tracer photography. Exp. Fluids 1 (1983), 179-184.

5.8.   Weinert, W.; Heber, J.; Bayerer,R.: Laser Stroboskop-Anemometer (LSA) zur Bestimmung von Strömungsvektorfeldern im Hochgeschwindigkeitsbereich. Z. Flugwiss. Weltraumforsch. 4 (198o), 137-142.

5.9.   Coutanceau, M.; Texier, A.: Experimental investigation of the creeping motion of a drop in a vertical tube. Exp. Fluids 4 (1986), 241-246.

5.1o. Dimotakis, P.E.; Debussy, F.D.; Koochesfahani, M.M.: Particle streak velocity field measurements in a two-dimensional mixing layer. Phys. Fluids 24 (1981), 995-999.

5.11. Utami, T.; Ueno, T.: Visualization and picture processing of turbulent flow. Exp. Fluids 2 (1984), 25-32.

5.12. Kobayashi, T.; Ishihara, T.; Sasaki, N.: Automatic analysis of photographs of trace particles by microcomputer system. In [1.6], pp. 231-235, 1985.

5.13. Racca, R.G.; Dewey, J.M.: A method for automatic particle tracking in a three-dimensional flow field. Exp. Fluids 5 (1987).

5.14. Barker, D.B.; Fourney, M.E.: Measuring fluid velocity with speckle patterns. Opt. Lett. 1 (1977), 135-137.

5.15. Dudderar, T.D.; Simpkins, P.G.: Laser speckle photography in a fluid medium. Nature 27o (1977), 45-47.

5.16. Grousson, R.; Mallick, S.: Study of the distribution of velocities in a fluid by speckle photography. Proceed. SPIE 136 (1977), 266-269.

5.17. Lallement, J.P.; Desailly, R.; Froehly, C.: Mésure de vitesse dans un liquide par diffusion cohérente. Acta Astronaut. 4 (1977), 343-356.

5.18. Françon, M.: Laser speckle and applications in optics. Academic Press, New York, 1979.

5.19. Adrian, R.J.: Scattering particle characteristics and their effect on pulsed laser measurements of fluid flow: speckle velocimetry vs particle image velocimetry. Appl. Opt. 23 (1984), 1690-1691.

5.2o. Iwata, K.; Hakoshima, T.; Nagata, R.: Measurement of flow velocity distribution by multiple-exposure speckle photography. Opt. Commun. 25 (1978), 311-314.

5.21. Gärtner, U.; Wernekinck, U.; Merzkirch, W.: Velocity measurements in the field of an internal gravity wave by means of speckle photography. Exp. Fluids 4 (1986), 283-287.

5.22. Bernabeu, E.; Amare, J.C.; Arrojo, M.P.: White-light speckle method of measurement of flow velocity distribution. Appl. Opt. 21 (1982), 2583-2586.

5.23. Suzuki, M.; Hosoi, K.; Toyooka, S.; Kawahashi, M.: White-light speckle method for obtaining an equi-velocity map of a whole flow field. Exp. Fluids 1 (1983), 79-81.

5.24. Meynart, R.: Digital image processing for speckle flow velocimetry. Rev. Sci. Instrum. 53 (1980), 110-111.

5.25. Erbeck, R.: Fast image processing with a microcomputer applied to speckle photography. Appl.Opt. 24 (1985), 3838-3841.

5.26. Adrian, R.J.: Image shifting technique to resolve directional amiguity in double-pulsed velocimetry. Appl. Opt. 25 (1986), 3855-3858.

5.27. Hinsch, K.; Schipper, W.; Mach, D.: Fringe visibility in speckle velocimetry and the analysis of random flow components. Appl. Opt. 23 (1984), 4460-4462.

5.28. Genceli, O.F.; Schemm, J.B.; Vest, C.M.: Measurement of size and concentration of scattering particles by speckle photography. J. Opt. Soc. Am. 7o (1980), 1212-1218.

5.29. Meynart, R.: Equal velocity fringes in a Rayleigh-Bénard flow by a speckle method. Appl. Opt. 19 (1980), 1385-1386.

5.3o. Simpkins, P.G.; Dudderar, T.: Laser speckle measurements of transient Bénard convection. J. Fluid Mech. 89 (1978), 665-671.

5.31. Lourenco, L.; Krothapalli, A.; Buchlin, J.M.; Riethmuller, M.L.: Noninvasive experimental technique for the measurement of unsteady velocity fields. AIAA J. 24 (1986), 1715-1717.

5.32. Lourenco, L.; Krothapalli, A.: The role of photographic parameters in laser speckle or particle image displacement velocimetry. Exp. Fluids 5 (1987), 29-32.

5.33. Meynart, R.: Instantaneous velocity field measurements in unsteady gas flow by speckle velocimetry. Appl. Opt. 22 (1983), 535-54o.

5.34. Meynart, R.: Speckle velocimetry study of vortex pairing in a low-Re unexcited jet. Phys. Fluids 26 (1983), 2o74-2o79.

5.35. Hinsch, K.; Mach, D.; Schipper, W.: Air flow analysis by double-exposure speckle photography. In [1.6], pp. 576-58o, 1985.

5.36. Koochesfahani, M.M.; Dimotakis, P.E.: Laser-induced fluorescence measurements of mixed fluid concentration in a liquid plane shear layer. AIAA J. 23 (1985), 17oo-17o7.

5.37. Rapagnani, N.L.; Davis, S.J.: Laser induced $I_2$ fluorescence measurements in a chemical laser flow field. AIAA J. 17 (1979), 14ö2-14o4.

5.38. Cenkner, A.A.; Driscoll, R.J.: Laser-induced fluorescence visualization on supersonic mixing nozzles that employ gas-trips. AIAA J. 2o (1982), 812-819.

5.39. Hiller, W.J.; Hägele, J.: Visualization of hypersonic micro-jets by laser-induced fluorescence. In [1.5], pp. 427-431, 1982.

5.4o. McDaniel, J.C.; Baganoff, D.; Byer, R.L.: Density measurements in compressible flows using off-resonant laser-induced fluorescence. Phys. Fluids 25 (1982), 1105-1107.

5.41. McDaniel, J.C.: Quantitative measurement of density and velocity in compressible flows using laser-induced fluorescence. AIAA Paper 83-0049, 1983.

5.42. Hiller, B.; Hanson, R.K.: Two-frequency laser-induced fluorescence technique for rapid velocity field measurements in gas flows. Opt. Lett. 1o (1985), 2o6-2o9.

5.43. Ackermann, U.; Baganoff, D.; McDaniel, J.C.: Dependence of laser-induced fluorescence on gas-dynamic fluctuations with application to measurements in unsteady flows. Exp. Fluids 3 (1985), 45-51.

5.44. Hassa, C.; Paul, P.H.; Hanson, R.K.: Laser-induced fluorescence modulation techniques for velocity measurements in gas flows. Exp. Fluids 5 (1987), 24o-246.

5.45. Miles, R.B.; Udd, E.; Zimmermann, M.: Quantitative flow visualization in sodium vapor seeded hypersonic helium. Appl. Phys. Lett. 32 (1978), 317-319.

42

5.46. Zimmerman, M.; Miles, R.B.; Hypersonic helium flow field measurements with the resonant Doppler velocimeter. Appl. Phys. Lett. 37 (198o), 885-887.

5.47. Zimmerman, M.; Cheng, S.; Miles, R.B.: Velocity selective flow visualization in a free supersonic nitrogen jet with the resonant Doppler velocimeter. In [1.6], pp. 449-453, 1985.

5.48. Dyer, M.J.; Crosley, D.R.: Two-dimensional imaging of OH laser-induced fluorescence in a flame. Opt. Lett. 7 (1982), 382-384.

5.49. Kychakoff, G.; Howe, R.D.; Hanson, R.K.; Knapp, K.: Flow visualization in combustion gases. AIAA Paper 83-o4o5, 1983.

5.5o. Kychakoff, G.; Howe, R.D.; Hanson, R.K.: Quantitative flow visualization technique for measurements in combustion gases. Appl. Opt. 23 (1984), 7o4-712.

5.51. Cattolica, R.J.; Vosen, S.R.: Fluorescence imaging of a flame-vortex interaction. Comb. Sci. Technol. 48 (1986), 77-88.

5.52. Kychakoff, G.; Knapp, K.; Howe, R.D.; Hanson, R.K.: Flow visualization in combustion gases using nitric oxide fluorescence. AIAA J. 22 (1984), 153-154.

5.53. Allen, M.G.; Hanson, R.K.: Digital imaging of species concentration fields in spray flames. Proceed. 21st Symposium (International) on Combustion (1986).

## 6. METHODS BASED ON REFRACTIVE INDEX MEASUREMENTS

The density of a fluid is a function of the fluid's refractive index. A number of optical methods are known by which variations of the refractive index in a transparent medium can be visualized and/or measured. These methods may be applied to the study of such flows that are associated with density changes caused by either compressibility, thermal effects, or mixing of fluids of different densities. Very common is the use of these methods in high-speed wind tunnels, ballistic ranges, and shock tubes. As a matter of fact, this is historically the first application of such optical methods for flow visualization. Independently of this field of application developed the use of the methods for studying convective heat transfer. Combustion and plasma flows are further fields of application where the three causes of density changes, compressibility, mixing, and high temperatures, may all be present simultaneously.

Refractive index fields are visualized or measured by line- of- sight methods, and the information is integrated along the path of the light through the transparent medium (fluid). When passing through the field, the light is affected with respect to its direction of propagation (refraction) and its optical phase. Either one of these effects is used in the methods to be discussed here. An extensive literature reviewing this field of experimentation is available; see, e.g. [6.1-6.6].

### 6.1 RELATIONSHIP BETWEEN FLUID DENSITY AND REFRACTIVE INDEX

An analysis of interaction of an electromagnetic wave and the molecules of a (transparent) medium delivers the relationship between the density of a fluid, and its refractive index; see, e.g. [1.1]. The general relationship which applies to both gases and liquids, known as the Clausius-Mosotti equation or the Lorenz-Lorentz equation, involves a number of molecular constants of the fluid and is not handy to work with. A simplified form, the Gladstone-Dale equation, applies to gases:

$$n - 1 = K \cdot \rho \tag{6.1}$$

Thus, the refractive index of a gas, $n$, is proportional to the density, $\rho$. The Gladstone-Dale constant $K$, having the dimension $[\rho^{-1}]$, is a characteristic quantity for each gas, and it changes slightly with the light wave length $\lambda$, since the refractive index, too, is known to depend on wavelength. Values of $K$ for a number of gases, and values of $K$ for air at various wavelenths are given in Table 6.1 and 6.2, respectively.

Table 6.1

Gladstone-Dale constants for different gases [1.1]

| gas | K[cm³/g] | wavelength [μm] | temperature [K] |
|---|---|---|---|
| He | 0.196 | o.633 | 295 |
| Ne | 0.075 | 0.633 | 295 |
| Ar | 0.157 | 0.633 | 295 |
| Kr | 0.115 | 0.633 | 295 |
| Xe | 0.119 | 0.633 | 295 |
| $H_2$ | 1.55 | 0.633 | 273 |
| $O_2$ | 0.19o | 0.589 | 273 |
| $N_2$ | 0.238 | 0.589 | 273 |
| $CO_2$ | 0.229 | 0.589 | 273 |
| NO | 0.221 | 0.633 | 295 |
| $H_2O$ (vapor) | 0.31o | 0.633 | 273 |
| $CF_4$ | 0.122 | 0.633 | 3o2 |
| $CH_4$ | 0.617 | 0.633 | 295 |
| $SF_6$ | 0.113 | 0.633 | 295 |

Table 6.2

Gladstone-Dale constant for air (at T = 288 K) [1.1]

| K [cm³/g] | wavelenth [μm] |
|---|---|
| 0.2239 | 0.9125 |
| 0.225o | 0.7o34 |
| 0.2259 | 0.6o74 |
| 0.2274 | 0.5o97 |
| 0.23o4 | 0.4o79 |
| 0.2330 | 0.3562 |

The quantity (n-1) is called the refractivity of a fluid. It is by orders of magnitude larger for liquids than for gases. Therefore, extremely small density differences in a liquid can produce considerably large signals in the optical methods to be discussed. The relationship between the refractive index and the density of water, as the most interesting working liquid, should be derived from the full Clausius-Mosotti equation. But since the necessary molecular data is not completely available, the relationship is usually provided by a calibration. The refractive index then is determined with an interferometer or refractometer. Most common are the two following situations: a) n is calibrated against the temperature of water; a formula describing accurately this relationship in the temperature range between 2o and 34°C has been given by Dobbins and Peck [6.7];b) n is measured for $H_2O$-NaCl solutions against the salinity at constant temperature. These solutions are of interest for performing stratified flow experiments. The relationship is found to be of the form

$$n_{saltwater} = n_o + const \cdot \rho, \qquad\qquad\qquad (6.2)$$

$\rho$ being the density of the solution and $n_o$ a reference value of the refractive index of saltwater; [6.8, 6.9]

The K-values in Table 6.1 are given for pure gases. If the working gas is a mixture

of several components with constant and known concentration (e.g. air), the Gladstone-Dale constant of the mixture can be calculated from the values of the pure components. Let n, K, $\rho$ be the refractive index, Gladstone-Dale constant, and density of the mixture, respectively; then, eq. (6.1) applies to the mixture, and K can be expressed by the values $K_i$ (of the i-th component) through

$$K = \sum_{i=1}^{N} K_i \frac{\rho_i}{\rho} = \sum_{i=1}^{N} K_i c_i \quad , \tag{6.3}$$

where the mixture is assumed to consist of N components of partial density $\rho_i$ or relative mass concentration $c_i$; i.e. $\sum \rho_i = \rho$ and $\sum c_i = 1$. Within sufficient accuracy, the Gladstone-Dale constant of air (Table 6.2) can be determined from the respective K-values for oxygen and nitrogen (Table 6.1).

An example of a gas mixture with unknown and local and/or temporal variation of the concentration values of the components is a flame. This means, that the density of the mixture, $\rho$, cannot be determined from a single optical measurement of the refractive index n, because the Gladstone-Dale constant of the mixture, K, is also variable. Or in other words: the number of unknowns is more that one (it is exactly N, namely $\rho$ and (N-1) values of $c_i$, see eq. (6.3)), and the information from one measurement of n is not sufficient for determining the N unknowns. A possible approach to this problem is to make use of the dispersive nature of n and K, i.e., optical measurements would have to be performed with several wavelenths $\lambda_j$. The number of wavelengths used should then be equal to N, and this would yield a set of N equations of the form

$$n(\lambda_j) - 1 = \sum_{i=1}^{N} K_i(\lambda_j) c_i \rho \quad . \tag{6.4}$$

Unfortunately, the $K_i$-values for most gaseous components are so weakly dispersive, that the optical signals for measuring n, taken at different wavelengths in the visible range, differ not enough for providing independent information.

The principle of taking multiple-wavelengths optical data has been successfully applied to plasma flows, i.e., to the flow of an ionized gas. If one considers a monatomic gas, the ionized gas is a mixture consisting of neutral atoms, ions, and free electrons. The degree of ionization, $\alpha_I$, is the (relative) mass concentration of ions in the mixture. Due to the little mass of an electron, the mass concentration of the electron gas component can be neglected. The Gladstone-Dale equation for this mixture can be written in the form

$$n-1 = \rho[(1-\alpha_I)K_A + \alpha_I K_I] + N_e K_e' \quad , \tag{6.5}$$

where $K_A$ and $K_I$ are the Gladstone-Dale constants of the atom gas and the ion gas, respectively; $N_e$ is the electron number density, i.e., the number of electrons per unit volume, and the Gladstone-Dale constant of the electron gas, $K_e'$, has the dimension $cm^3$, different from the dimension of $K_A$ and $K_I$. For argon, a gas frequently used in plasma experiments, Alpher and White [6.1o] have found $K_I = \frac{2}{3} K_A$. The value of the refractive index of the electron gas, $n_e$, is determined in plasma theory, and it is found to be proportional to the square of the light wavelength. If one measure $\lambda$ in cm, the Gladstone-Dale equation for the electron gas can be written as

$$n_e - 1 = -4.46 \cdot 10^{-14} \cdot \lambda^2 \cdot N_e \quad . \tag{6.6}$$

Thus, $K_e'$ is highly dispersive. The contribution of $K_e'$ at high enough ionization degrees, causes the refractive index n of the ionized gas to depend strongly on the wavelength. Measuring the optical signal at three different wavelengths $\lambda_j$ (see eq. (6.4)) therefore enables one to determine the three unknowns in eq. (6.5), $\rho$, $\alpha_I$, and $N_e$; see, e.g., [6.11].

At a given wavelength, the refractivity (n-1) per electron is by an order of magnitude greater than that per atom. The optical behavior of an ionized gas is therefore dominated by the presence of free electrons, even at a relatively low ionization level. Since the Gladstone-Dale constant of the electron gas is negative, the optical response to density changes is opposite to the respective optical response caused by the neutral or the atom gas. Ionization is often produced through a strong shock wave. The production of free electrons and the simultaneous increase of the neutral gas density cause optical signals of opposite sign, in the worst case just cancelling one another.

A dissociated diatomic gas is a mixture of (neutral) molecules and free atoms. With $\alpha_D$ being the degree of dissociation, the Gladstone-Dale equation for a dissociated gas is

$$n-1 = \rho[(1-\alpha_D)K_M + \alpha_D K_A] \quad , \qquad\qquad (6.7)$$

where $K_M$ and $K_A$ are the Gladstone-Dale constants of the molecule and the atom gas, respectively, Values of $K_A$ for oxygen and nitrogen have been measured in shock tube experiments [6.12, 6.13].

The derivation of the Gladstone-Dale equation (6.1) involves a number of simplifying assumption. One of then is that the wavelength of the light in the measuring system is far from an absorption wavelength of the test gas. This is usually the case for "normal" gases and at "normal" thermodynamic conditions. (For this reason, the gas is invisible.) However, the assumption might be violated for some "unusual" gases or vapors and at high temperatures when the gas is in an excited state. Then, absorption wavelengths may exist in the visible range of the spectrum. Close to such an absorption wavelength, the gas exhibits anomalous dispersive behavior with the refractivity (n-1) being many orders of magnitude greater than in the nonresonant regime. The result is that the same absolute density change $\Delta\rho$ will produce much stronger alterations in the refractive index of the gas, $\Delta n$, or cause much higher signal amplitudes. Enhancement of flow visualization near resonant or absorption wavelengths has been verified by seeding a gas with sodium vapor and operating the light source in the optical system with the sodium $D_2$ wavelength [6.14, 6.15].

## 6.2  DEPENDENCE OF THE VISIBLE SIGNAL ON THE REFRACTIVE INDEX DISTRIBUTION

A light ray tensmitted through a fluid flow of variable refractive index is affected in two different ways: The ray is deflected from its original direction (this is usually understood as "refraction"), and the wave describing this light ray or beam is altered with respect to its optical phase. Both quantities, light deflection and optical phase change, are integrated quantities, i.e., they can be measured after the light is transmitted through the flow, and nothing follows from these measurable quantities on how the light wave was affected at a particular position inside the flow. The optical methods to be discussed depend on one of the two measurable effects. All interferometric methods visualize differences in the optical phases of two (or more) light waves. A number of methods are available whose signal is a measure of the integrated value of the light deflection in the flow field. Most of the latter methods provide qualitative results, i.e. flow picture, while the interferometric methods also allow for a quantitative determination of the refractive index or density distribution.

The dependence of the signal of each method on the refractive index distribution must be found from a detailed analysis of the optical path in the flow (see, e.g., [1.1], also for further references). Tabel 6.3 lists the classes of optical methods, the types of signals available from a record (photograph), and the dependence of this signal on the refractive index distribution $n(x,y,z)$. It is assumed in the table that only the light deflection or the change of n in the y-direction contribute to the signal. The incident light is assumed to be parallel to the z-direction (Fig. 6.1). It is seen that the methods are grouped in the table in a systematic way: The shadowgraph depends on the second derivative of n; schlieren, moiré, speckle and schlieren interference technique on the first derivative; and reference interferometry on the absolute value (zeroth derivative) of n.

Table 6.3

Optical methods for flow visualization, signal pattern, and dependence on the distribution of the refractive index n

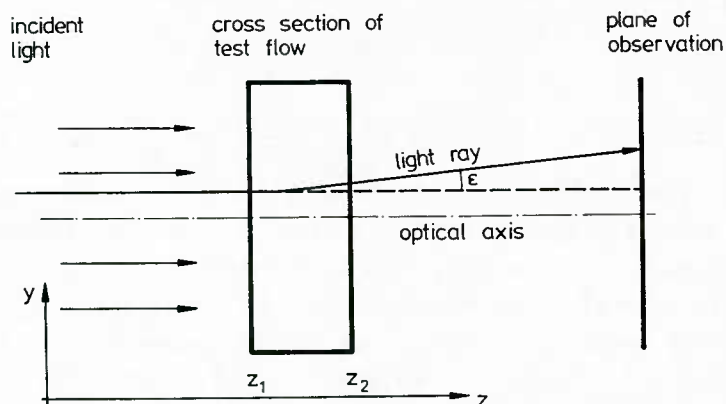| method | measured signal | dependence on n |
|---|---|---|
| shadowgraph | intensity constrast | $\ell \cdot \int_{z_1}^{z_2} \frac{\partial^2 n}{\partial y^2} \, dz$ |
| schlieren | intensity constrast | |
| moiré | moiré fringe shift | |
| speckle photography | displacement of speckles | $\int_{z_1}^{z_2} \frac{\partial n}{\partial y} \, dz$ |
| schlieren interferometer | fringe order or fringe shift | |
| reference beam interferometer | fringe order or fringe shift | |
| phase contrast | fringe order | $\int_{z_1}^{z_2} n \, dz$ |



Fig. 6.1: Deflection of a light ray in an inhomogeneous density field. $z_1$, $z_2$ are entrance and exit coordinates of the ray in the flow field. The ray is deflected by an angle $\varepsilon$.

In the general case, the refractive index is a function of all three space coordinates: $n = n(x,y,z)$. As shown in the 3rd column of Table 6.3, the dependence of n on z is not recovered because of the integration from $z_1$ to $z_2$ in the z-direction. Here, $z_1$

is the coordinate where a particular ray enters the flow field, and $z_2$ is its exit coordinate. The refractive index in the medium outside of the test field is assumed to be homogeneous. Determining the three-dimensional distribution n (x,y,z) requires to take more than one record of the visible signal, each under a different viewing angle. Such a procedure and the involved computer-evaluation of the data is known as tomography.

The results in the third column of Table 6.3 are derived in the respective theory under the simplifying assumption that the light propagates along a straight path, parallel to the z-direction through the flow. This is somewhat contradictory to the fundamental principle of those methods which are based on the deflection of light in the test field. The theory takes into account the finite curvature of the light rays when they leave the field, but it neglects the differences in the heights y of the entrance and exit position (Fig. 6.1). The assumption is very reasonable for the majority of experiments performed in gas flows. Violations of this assumption, referred to as "strong refraction effects", occur in the presence of large gradients of the refractive index or density, and in liquids where the refractivity (n-1) is not very small when compared with one.

In the case of strong refraction one is confronted with the problem that not only the refractive index along the light path is unknown, but also the (geometrical) light path itself. The problem has been investigated for a number of special cases and with a two-dimensional refractive index field, n = n(x,y). Most of the approaches are numerical studies that demonstrate, by means of optical ray tracing, the difference between strong refraction and the refraction-free situation. The thermal boundary layer close to a heated, vertical flat plate is a typical example of such a plane flow with strong refraction in one direction due to a large temperature gradient normal to the plate. The refractive bending of the light may be studied in a plane x = const (the plane of Fig. 6.1). With an exact knowledge of the distribution of the refractive index in this plane, n (y), one could calculate the trajectory of a light ray through the flow. If one can assume, that n is distributed linearly in this plane, it follows that the light trajectory is a parabola; see, e.g. [6.16 - 6.18]. The refractive index field can then be reconstruced from the interferogram by making use of this "correction parabola".

Due to the strong refraction effects, the image of the test field in the recording plane is distorted. This distortion can be minimized by focusing onto the recording plane a plane z = const in the test field situated between the center and a position at one-third the field width away from the exit plane into the test section [6.19].

For the purpose of a comparison of the optical signal, which can be obtained with the various methods, Figs. 6.2 - 6.6 present visualizations of the same test object by different methods. The flow under study is the Rayleigh-Bénard convection in a rectangular enclosure with a slight temperature difference (ΔT ~ 2K) between top and bottom plate. The test fluid is silicon oil. Due to the high refractivity of the liquid, the shadowgraph exhibits a considerable optical distortion. The flow cells are clearly distinguishable. Since the test field is two-dimensional, the fringes in the Mach-Zehnder interferogram are curves of equal temperature. The fringe contours in the schlieren interferogram of Fig. 6.5 coincide with the streamlines. This applies only to the special adjustment of the interferometer in this figure, as it has been verified by Bühler [6.20]. A different adjustment of this instrument (Fig. 6.6) results in a completely different pattern. The generation of the patterns visible in these figures will be explained in the following chapters.
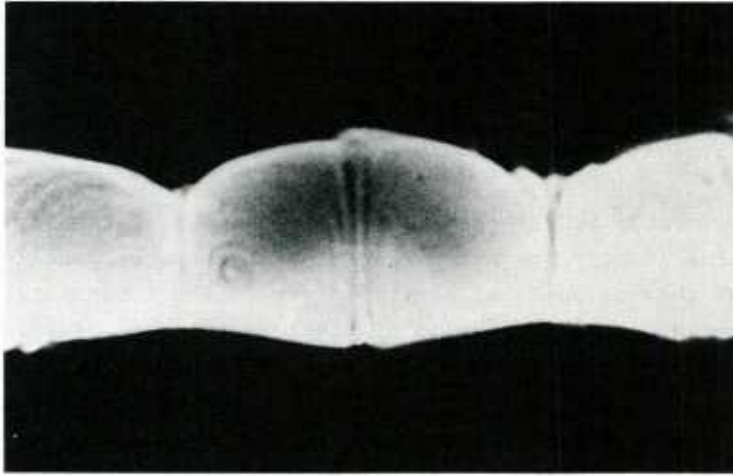
48



Fig. 6.2: Shadowgraph of the Rayleigh-Bénard flow cells in a rectangular enclosure filled with silicon oil. Temperature difference between top and bottom plate is about 2K. The photographic imaging is distorted due to the strong refraction in the test field.
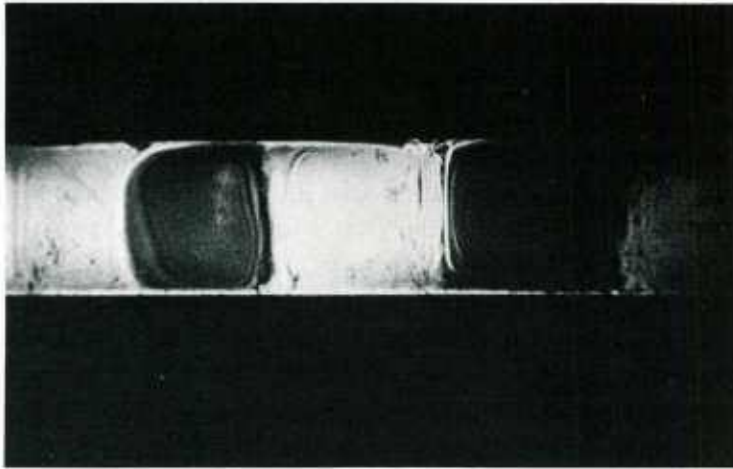


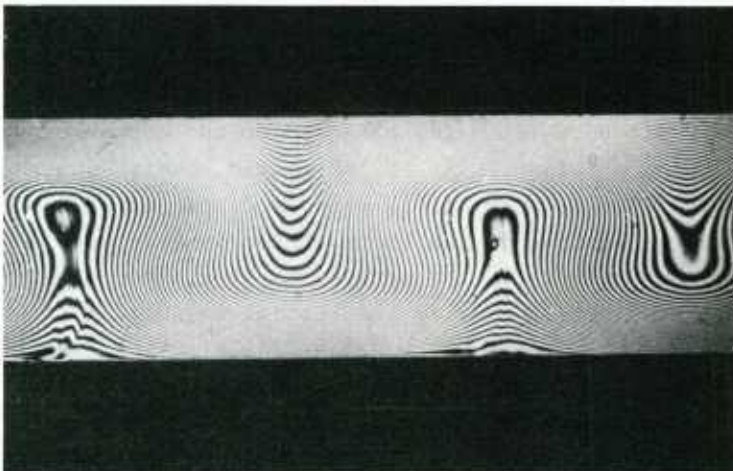Fig. 6.3: Schlieren record of the flow shown in Fig. 6.2. Original is taken in a color schlieren system.



Fig. 6.4: Mach-Zehnder interferogram of the flow shown in Fig. 6.2. The interferometer was aligned to infinite fringe width. The fringes are contours of constant temperature.
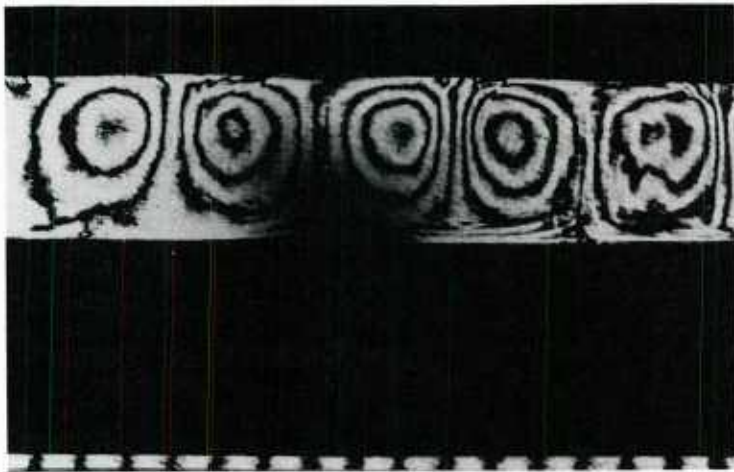
Fig. 6.5: Schlieren interferogram taken with a Wollaston prism interferometer of the flow shown in Fig. 6.2. The interferometer was aligned to finite fringe width with the undisturbed fringes being vertical.
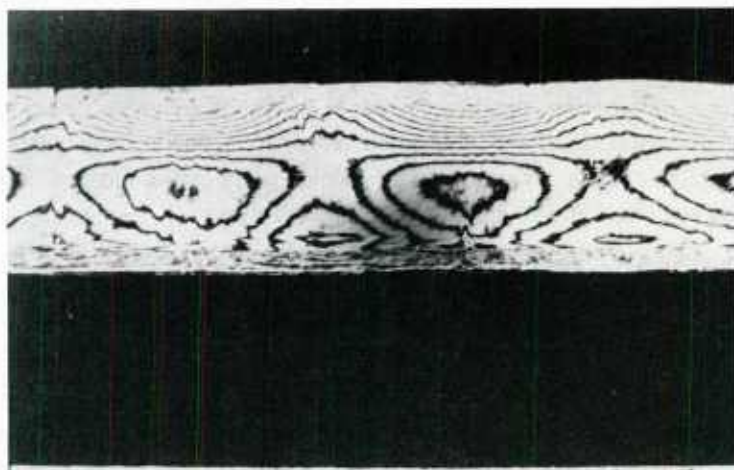


Fig. 6.6: Schlieren interferogram taken with a Wollaston prism interferometer of the flow shown in Fig. 6.2. The interferometer was aligned to infinite fringe width at horizontal undisturbed fringes.

## References

6.1. Weinberg,F.J.: Optics of flames. Butterworth, London, 1963.

6.2. Hauf, W.; Grigull, U.: Optical methods in heat transfer. Adv. Heat Transfer 6 (1970), 131-366.

6.3. Goldstein, R.J.: Optical measurements of temperature. In: Measurement in Heat Transfer (eds. E.R.G. Eckert, R.J. Goldstein), pp. 241-293, Hemisphere, Washington, 1976.

6.4. Merzkirch, W.: Density-sensitive flow visualization. In: Fluid Dynamics (ed. R.J. Emrich), Vol. 18A of Methods in Experimental Physics, pp. 345-4o3, Academic Press, New York, 1981.

6.5. Goldstein, R.J.: Optical systems for flow measurement: shadowgraph, schlieren, and interferometric techniques. In: Fluid Mechanics Measurements (ed. R.J. Goldstein), pp. 377-422, Hemisphere, Washington, 1983.

6.6. Lauterborn, W.; Vogel, A.: Modern optical techniques in fluid mechanics. Ann. Rev. Fluid Mech. 16 (1984), 223-244.

6.7. Dobbins, H.M.; Peck, E.R.: Change of refractive index of water as a function of temperature. J. Opt. Soc. Am. 63 (1973), 318-32o.

6.8. Grange, B.W.; Stevenson, W.H.; Viskanta, R.: Refractive index of liquid solutions at low temperatures: an accurate measurement. Appl. Opt. 15 (1976), 858-859.

6.9. Peters, F.: Schlieren interferometry applied to a gravity wave in a density-stratified liquid. Exp. Fluids 3, 261-269.

6.1o. Alpher, R.A.; White, D.R.: Optical refractivity of high temperature gases. II: Effects resulting from ionization of monatomic gases. Phys. Fluids 2 (1959), 162-169.

6.11. Radley, R.J.: Two-wavelength holography for measuring plasma electron density. Phys. Fluids 18 (1975), 175-179.

6.12. Alpher, R.A.; White, D.R.: Optical refractivity of high temperature gases. I: Effects resulting from dissociation of diatomic gases. Phys. Fluids 2 (1959), 153-161.

6.13. Anderson, J.H.B.: Experimental determination of Gladstone-Dale constants for dissociating oxygen. Phys. Fluids 12 (1969), Suppl. I 57-6o.

6.14. Blendstrup, G.; Bershader, D.; Langhoff, P.W.: Resonance refractivity studies of sodium vapor for enhanced flow visualization. AIAA J. 16 (1978), 1106-1108.

6.15. Kügler, E.; Bershader, D.: Recent high-resolution resonant refractivity studies of a sodium-seeded flame. Exp. Fluids 1 (1983), 51-55.

6.16. Grigull, U.: Einige optische Eigenschaften thermischer Grenzschichten. Int. J. Heat Mass Transfer 6 (1963), 669-679.

6.17. Howes, W.L.; Buchele, D.R.: Optical interferometry of inhomogeneous gases. J. Opt. Soc. Am. 56 (1966), 1517-1528.

6.18. Anderson, E.E.; Stevenson, W.H.; Viskanta, R.: Estimating the refractive error in optical measurements of transport phenomena. Appl. Opt. 14 (1975), 185-188.

6.19. Mehta, J.M.; Worek, W.M.: Analysis of refraction errors for interferometric measurements in multicomponent systems. Appl. Opt. 23 (1984), 928-933.

6.2o. Bühler, K.; Kirchartz, K.R.; Oertel, H.: Steady convection in a horizontal fluid layer. Acta Mech. 31 (1979), 155-171.

## 7. SHADOWGRAPH

The shadowgraph, scientificly explored first by Dvorak [7.1], is the simplest of the optical visualization methods. It does not require any optical element except a light source, and the shadow effect produced by refractive index fields can be observed, therefore, outside a laboratory in the open air where the sun serves as the light source. Examples are the shadow patterns of raising warm air or benzene vapor, projected by the sun light onto a rigid surface. Even projections of shock waves have been observed in the open air, as will be shown below.

In a laboratory experiment, either a divergent or a parallel beam of light is transmitted through the test section of the flow facility (Fig. 7.1). The shadow pattern is observed in a plane, normal to the optical axis, at a distance $\ell$ behind the flow field. Most essential, as for any optical visualization method, is the use of a point source. In order to avoid noise by diffraction, a thermal light source should be used and not a laser source.
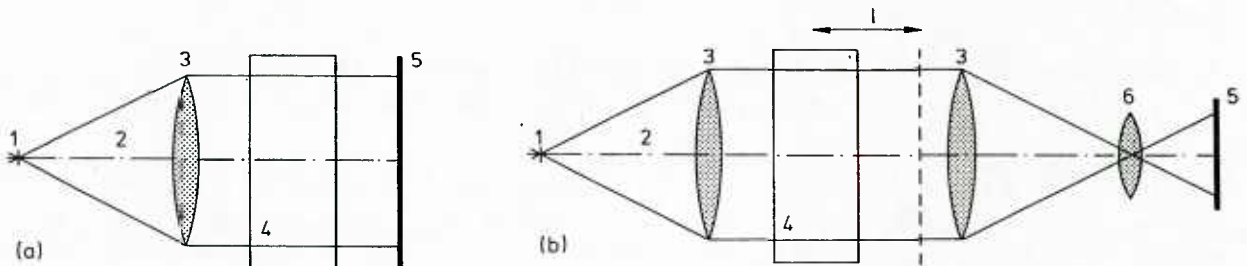


Fig. 7.1: Shadowgraph system without (a) and with (b) camera; 1: point light source; 2: optical axis; 3: collimating lenses; 4: cross section of flow facility test section; 5: recording plane (photographic film); 6: camera objective.

It is of interest to visualize large fields of view. Because it is then impractical to record the shadow on a respectively large photographic plate (Fig. 7.1a), a camera is focused onto the position (plane) at distance $\ell$ from the test field (Fig. 7.1b). The choice of the value of $\ell$ depends on the flow under study. The sensitivity of the method with respect to resolving small density changes increases with $\ell$; however, edges of rigid bodies in the test field, e.g. test models, will be the more out of focus, the larger the value of $\ell$, so that it becomes often necessary to find a compromise between optical sensitivity and local resolution.

Visualization of a flow, which is invisible when viewed without any optical aid, means that the plane of observation (recording plane) contains an information which is perceivable for the eye. Since the eye can perceive information only in the form of changes

of light amplitude or intensity, the optical analysis of the shadowgraph determines the relative changes of light intensity, $\Delta I/I$, which exist in the recording plane due to the shadow effect. I is the uniform light intensity for a homogeneous refractive index field, and $\Delta I$ are the intensity changes caused by variation of the refractive index n in the flow. The result for $\Delta I/I$ (also called the contrast) is (see, e.g. [1.1]):

$$\frac{\Delta I(x,y)}{I} = \ell \cdot \int_{z_1}^{z_2} (\frac{\partial^2}{\partial x^2} + \frac{\partial^2}{\partial y^2}) \ln n(x,y,z) \, dz. \tag{7.1}$$

The information, here: the contrast $\Delta I/I$, is recorded in a x-y plane. The dependence of n on z is not recovered due to the integration in z-direction.

The most dramatic change in the second derivative of n or the density $\rho$ occurs in a shock wave. The shadowgraph is most appropriate for visualizing the geometry of shock patterns, either a steady configuration in supersonic flow (Fig. 7.2), or unsteady shock configurations produced in a shock tube (Fig. 7.3). The shock appears as a dark contour,
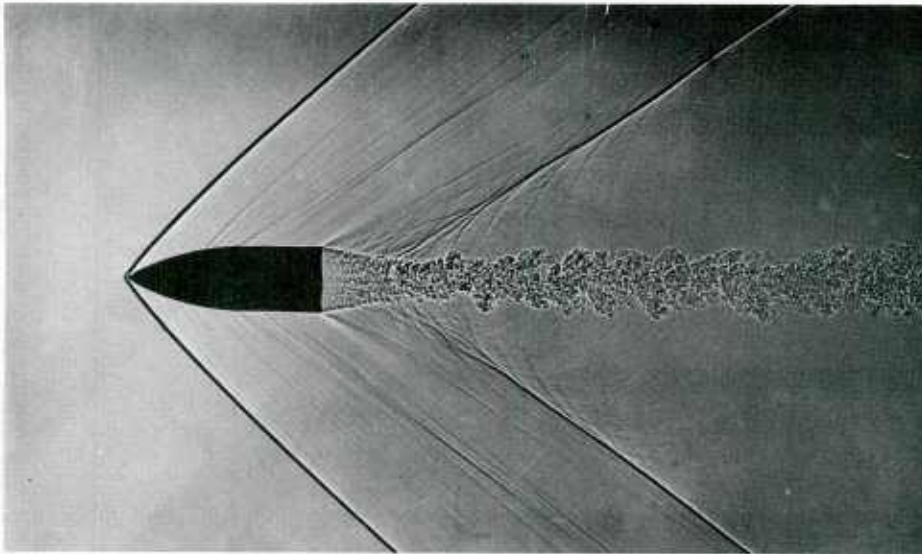


Fig. 7.2: Shadowgraph of a projectile flying at supersonic speed. Clearly seen are the formation of shock waves and the turbulent wake behind the projectile (German-French Research Institute ISL, St. Louis, France).

the "shadow" of the shock. No light is arriving at this contour line because it has been deflected due to the strong density change. In many cases the deflected light is regained in concentrated form as a bright band on the downstream side of the dark shock contour. Shadowgraphs are used for measuring the stand-off distance of the bow shock at a blunt body in supersonic flow. For such a measurement it is important to know that the exact location of the infinitesimally thin shock surface is the upstream edge of the visible dark band. While in conventional systems the recording of these data is performed by photographic means [7.2], modern systems use CCD cameras or linear arrays of photodiodes for this purpose [7.3, 7.4].

Projections by the sunlight of a shock wave onto a surface can be observed in the open air. The shadow of the shock waves giving rise to the buffeting of an airplane at high subsonic Mach numbers can be seen from the inside of the plane on the wing surface if the sun is at an appropriate position [7.5]. The projection of the spherical blast shock generated by a large scale explosion is shown in Fig. 7.4. This photograph has been
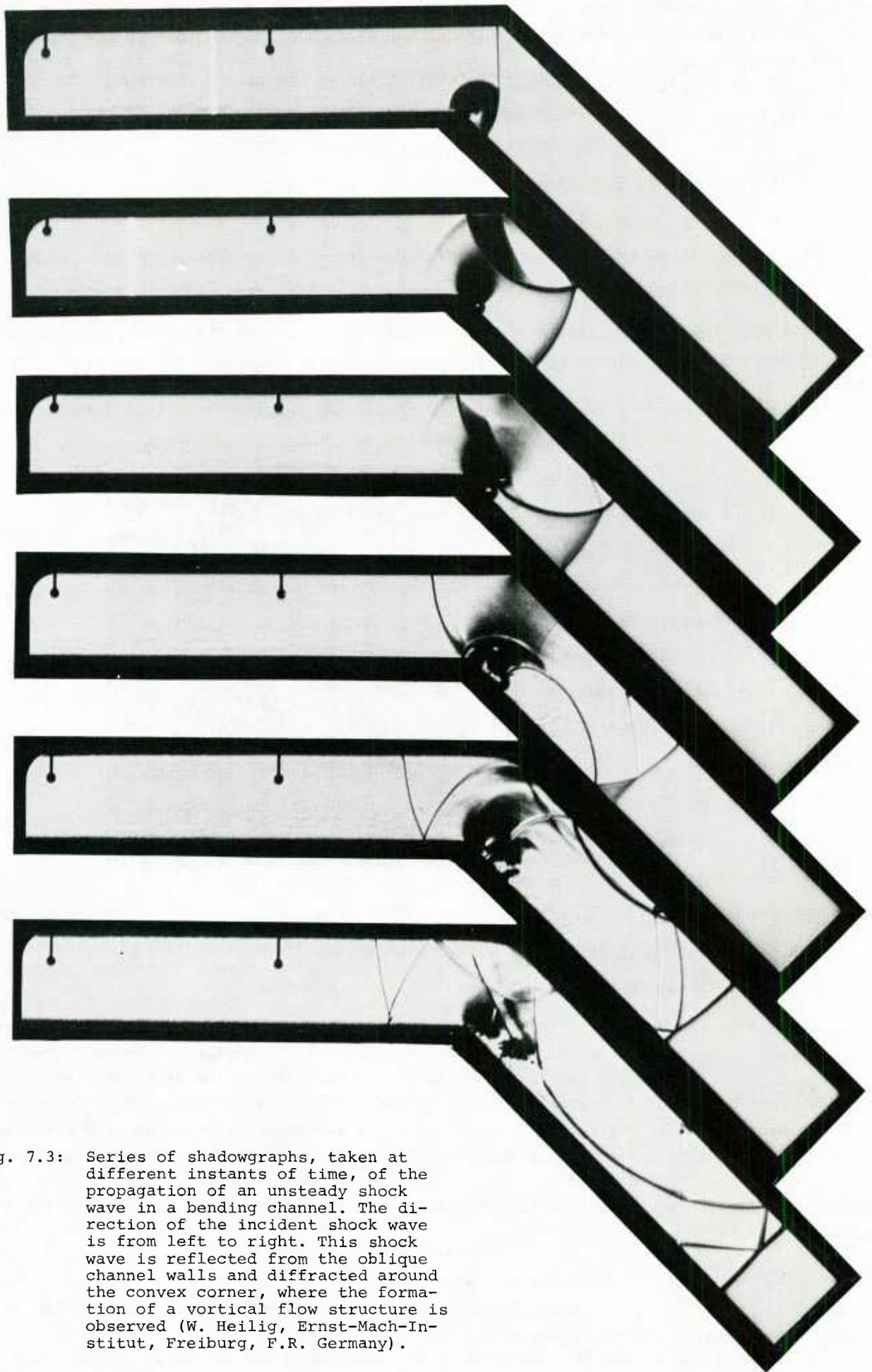
Fig. 7.3:  Series of shadowgraphs, taken at
           different instants of time, of the
           propagation of an unsteady shock
           wave in a bending channel. The di-
           rection of the incident shock wave
           is from left to right. This shock
           wave is reflected from the oblique
           channel walls and diffracted around
           the convex corner, where the forma-
           tion of a vortical flow structure is
           observed (W. Heilig, Ernst-Mach-In-
           stitut, Freiburg, F.R. Germany).

Fig. 7.4.:  Projection by sunlight of a hemispherical shock wave onto the ground surface, as seen from an airplane. The shock originated from a 5oo tons TNT hemispherical explosion (J.M. Dewey, University of Victoria, B.C., Canada)

taken from an airplane. The center of the explosion is in the center of the circular area of which only a part is included in the photograph. Since the projection by the sunlight onto the surface is oblique, the shadow of the shock is an ellipse, and it is not the true, circular position of the shock on the surface. The true position is also visible due to a compression and respective change of the surface (soil) structure.

The light rays bended and deflected in the shadowgraph system may overlap or intersect before reaching the recording plane, sometimes forming a caustic. The density profile in a laminar compressible boundary layer can cause such a concentration of light, forming a bright band parallel to the wall (Fig. 7.5). Shadowgraphs taken of turbulent flow fields
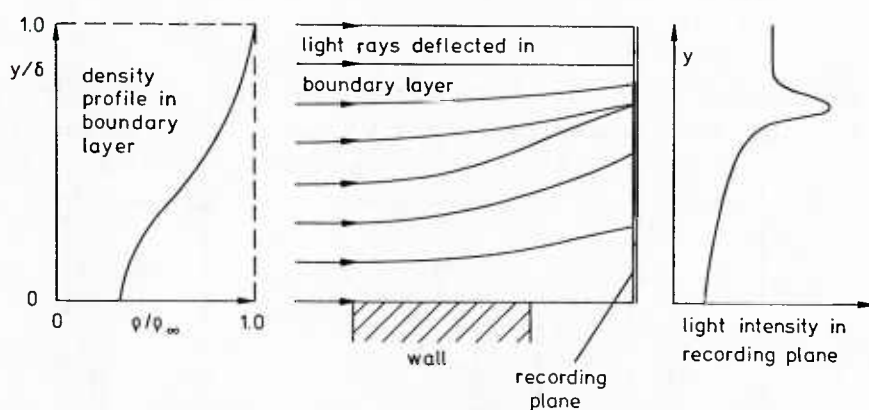


Fig. 7.5:  Bending of light rays as caused by the density profile in a compressible boundary layer. The resulting light intensity in the recording plane has a maximum; correspondingly, the shadowgraph will exhibit a bright band parallel to the wall.

with short enough an exposure time show a granular pattern, which carries information on the structure of turbulence in the fluctuating density field. This pattern which, again, is the result of an integration along the light path, can be analyzed with statistical methods. Uberoi and Kovsznay [7.6] have devised a way which allows, in principle, for de-

riving the statistics of the three-dimensional density field from the statistical analysis of the two-dimensional shadow pattern, provided that the turbulence can be assumed to be isotropically distributed. Although attempts have been made to quantify this process by digital image processing [7.7], the procedure is rather impractical, and the analysis of this problem by speckle photography (see chapter 9) has been shown to deliver more reliable results.

In summary, the shadowgraph is not a method suitable for quantitative measurements of the fluid density. However, it is a convenient method for obtaining a quick survey of flow fields with varying density, particularly shock waves.

References

7.1.   Dvorak, V.: Über eine neue einfache Art der Schlierenbeobachtung. Ann. Phys. Chem. 9 (1880), 502-512.

7.2.   Stilp, A.: Der Freiflugkanal des Ernst-Mach-Instituts. Z. Flugwiss. 16 (1968), 12-16.

7.3.   Sajben, M.; Crites, R.C.: Real-time optical measurement of time-dependent shock position. AIAA J. 17 (1979), 910-912.

7.4.   Roos, F.W.; Bogar, T.J.: Comparison of hot film probe and optical techniques for sensing shock motions. AIAA J. 20 (1982), 1o71-1o76.

7.5.   Larmore, L.; Hall, F.F., Jr.: Optics for the airborne observer. SPIE 9 (1971), 87-94.

7.6.   Uberoi, M.S.; Kovasznay, L.S.G.: Analysis of turbulent density fluctuations by the shadow method. J. Appl. Phys. 26 (1955), 19-24.

7.7.   Hesselink, L.; White, B.S.: Digital image processing of flow visualized photographs. Appl. Opt. 22 (1983), 1454-1461.

8.   SCHLIEREN SYSTEMS

With only a slight modification of its optical arrangement, the shadowgraph can be converted into a system which is much more sensitve with respect to density changes: the schlieren system. It became widely known through the detailed discussion in Toepler's book of 1864 [8.1], and it has since then be named the Toepler method. A great variety of modifications have been described, the newest developments have continuously been surveyed [8.2 - 8.8]. Among these reviews, the survey by Schardin [8.3] has the reputation to be the classical reference work, particularly in the fields of experimental aerodynamics, gasdynamics, and ballistics.

A schlieren system with parallel light through the test field is considered (Fig. 8.1). The parallel light beam is made convergent by a lens or a spherical (parabolic) mirror called the "schlieren head". An image of the light source is formed in the focal point of the schlieren head. At this position, a knife edge (perpendicular to the plane
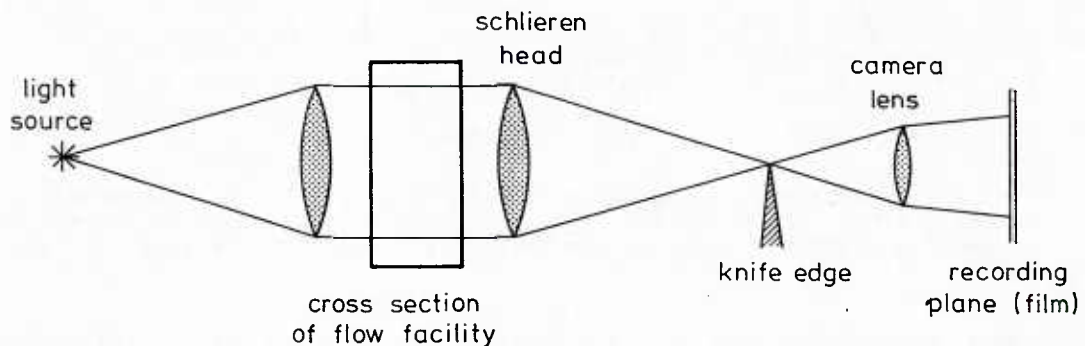


Fig. 8.1:   Toepler schlieren system with parallel light passing through the test section of the flow facility.

of Fig. 8.1) is cutting off a certain portion of the light source image, thereby reducing

the intensity with which the recording plane is illuminated. The camera lens focuses a plane in the flow field onto the recording plane, so that shadow effects are eleminated.

An essential requirement for the schlieren system is the use of a point light source or a slit source, the slit being parallel to the knife edge. The image of the point source is a small circle, of which only a part of height $\underline{a}$ is allowed to pass over the knife edge (Fig. 8.2). With a homogeneous test field, the recording plane is evenly illu-
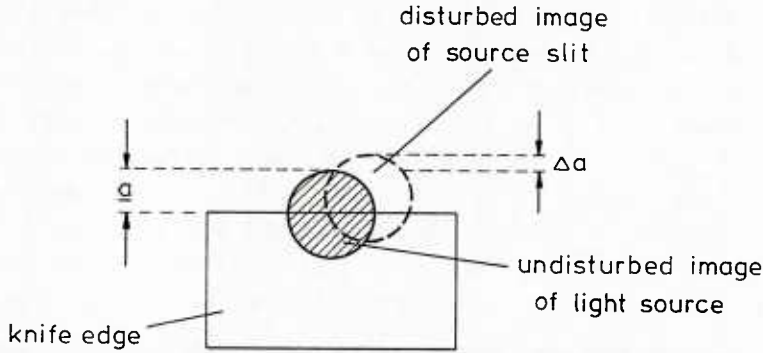


Fig. 8.2: Image of the light source in the plane of the knife edge.

minated with an intensity $I(x,y)$ = const, which is the lower, the smaller the value of $\underline{a}$. Light rays deflected by an angle $\varepsilon_y$ due to a disturbance in the test field cause a (vertical) shift of the light source image by an amount $\Delta a$:

$$\Delta a = f \cdot \tan \varepsilon_y \quad , \tag{8.1}$$

with f being the focal length of the schlieren head. The corresponding image points in the recording plane receive an intensity changed by $\Delta I$; the relative intensity change (contrast) is

$$\frac{\Delta I}{I} = \frac{\Delta a}{\underline{a}} = \frac{f}{\underline{a}} \cdot \tan \varepsilon_y \quad , \tag{8.2}$$

and from the respective optical analysis, which relates the deflection angle to the refractive index variation in the test field, it follows that

$$\frac{\Delta I(x,y)}{I} = \frac{f}{\underline{a}} \cdot \int_{z_1}^{z_2} \frac{1}{n} \frac{\partial n}{\partial y} dz \quad , \tag{8.3}$$

which reduces for a gas flow to

$$\frac{\Delta I(x,y)}{I} = \frac{K \cdot f}{\underline{a}} \cdot \int_{z_1}^{z_2} \frac{\partial \rho}{\partial y} dz \quad . \tag{8.4}$$

If the knife edge is turned by $90°$, the deflection angle $\varepsilon_x$ will be measured, and the recorded relative intensity change then is

$$\frac{\Delta I(x,y)}{I} = \frac{f}{\underline{a}} \int_{z_1}^{z_2} \frac{1}{n} \frac{\partial n}{\partial x} dz \quad . \tag{8.5}$$

This brief analysis of the Toepler system shows that a schlieren photograph exhibits changes of the relative illumination intensity which are a measure of the refractive index or density gradient in the direction normal to the knife edge. Determining the two components $\frac{\partial \rho}{\partial x}$ and $\frac{\partial \rho}{\partial y}$, requires to take two records with the knife edge turned by $90°$ between the two exposures.

For a given density field, the relative change in light intensity or the contrast in the photographic record is the larger, the smaller the ratio ($\underline{a}$/f). If one assumes, that a relative intensity change of $\Delta I/I = 0.1$ is still detectable, the smallest deflection angle that can be measured is $\varepsilon_{min} = 0.1$ ($\underline{a}$/f). While the focal length of the schlieren head, f, usually is a given quantity, one could conclude that the sensitivity of the system could be increased without limitation by decreasing the aperture $\underline{a}$. There are, however, mainly three reasons which limit the possibility of reducing the value of $\underline{a}$: 1. the overall illumination intensity I(x,y) is reduced with $\underline{a}$, and the mean signal amplitude might fall below a minimum determined, e.g., by the film speed; 2. it is desirable to measure positive and negative values of $\varepsilon$ with the same resolution; the greatest possible intensity change for negative $\varepsilon$ (Fig. 8.2) is absolute extinction, i.e. $\Delta I = -I$ for $\varepsilon = -\varepsilon_{max}$, and $(\underline{a}/f)_{min} \leqq \varepsilon_{max}$; 3. diffraction effects become effective at small values of $\underline{a}$, thereby blurring the image of the test field. Since diffraction noise increases with the coherence of the light source, it follows that a laser is not an appropriate source for a schlieren system. The sensitivity of the Toepler system, that obviously depends on a number of different physical phenomena, has extensively been studied in the past [8.9-8.14].
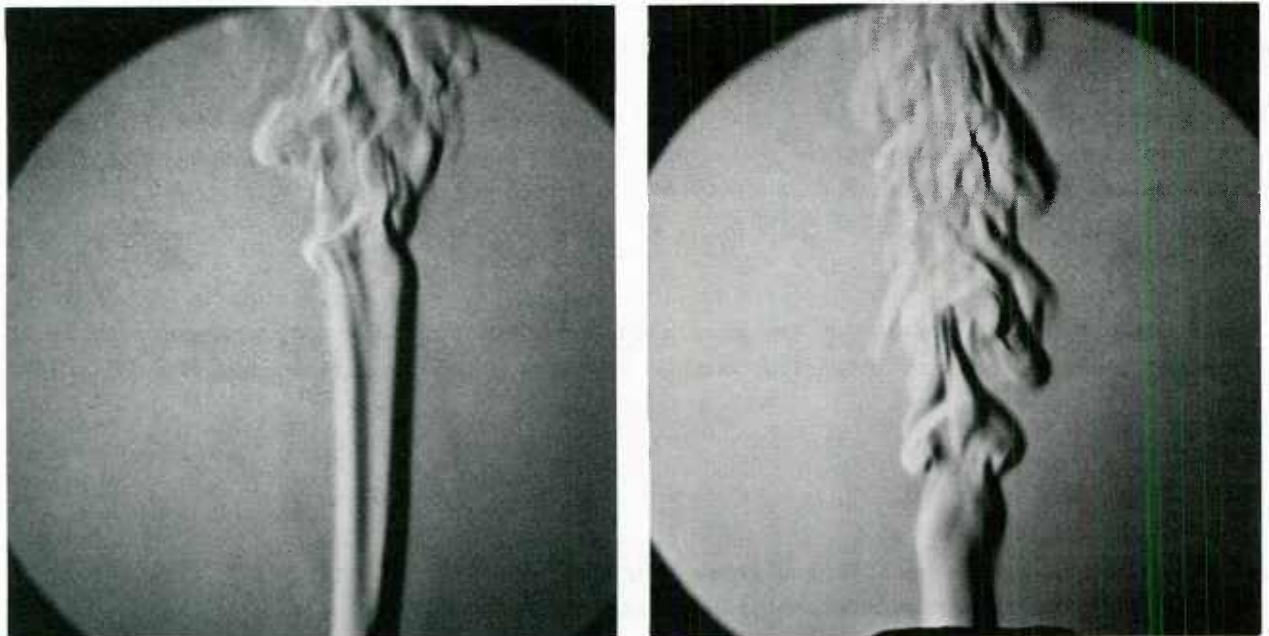


Fig. 8.3:   Toepler schlieren photographs of the unstable jet of a foreign gas (helium) exhausting in the ambient air.

The black-and-white schlieren photograph (Fig. 8.3) can, in principle, be evaluated for determining the distribution of the deflection angle, $\varepsilon$(x,y) or, after a respective integration, the distribution of the fluid density $\rho$(x,y). This evaluation process requires measuring the shades of grey in quantitative form. A serious source of errors is introduced by the photographic recording and development. The use of a television camera for the recording and the subsequent digitization of the image can make this evaluation independent from subjective measurements; see, e.g., [8.15]. However, the determination of gradual intensity changes or contrast remains an unreliable method, and schlieren systems are primarily used for qualitative investigations of density fields, but with a much higher degree of resolution than the shadowgraph. As will be shown in the following sections, a schlieren setup can easily be converted into systems being more appropriate for quantitative measurements of $\partial n/\partial y$.

A number of optical errors are associated with the use of lenses. These errors affect the quality of the light source image in the focal point of the schlieren head, and therefore the precision of the schlieren effect. Astigmatism can be corrected by a system of plano-cylindrical lenses [8.16, 8.17]. Coma is avoided if, in an off-axis configuration

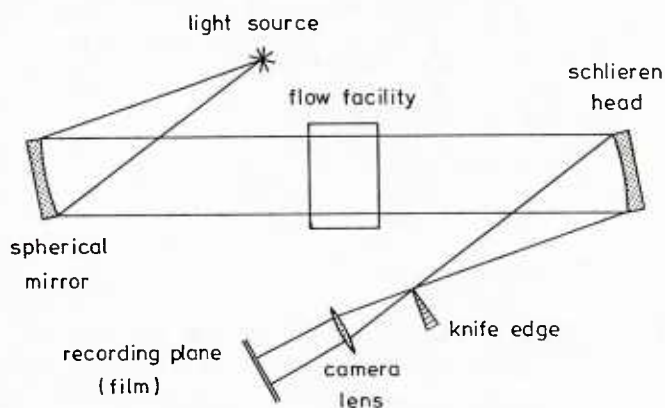with spherical or parabolic mirrors, the optical axis forms a Z (Fig. 8.4).



Fig. 8.4: Z-configuration of a schlieren system with spherical (or parabolic) mirrors

In a "double-pass schlieren system", which serves for increasing the sensitivity towards small density changes, a conical light beam passes twice through the test field. Such a system is often applied in ballistic ranges to study the flow around hypervelocity projectiles under extreme low density conditions [8.18, 8.19]. With the use of a beam splitter, as shown in Fig. 8.5, the system is "on-axis", and one avoids almost totally coma and astigmatism.
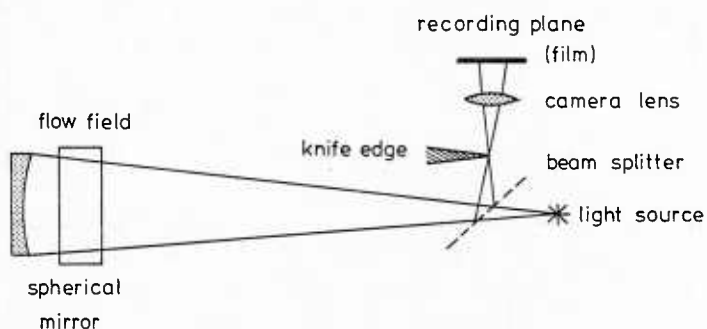


Fig. 8.5: Double-pass schlieren system using a beam splitter

The manipulation of the light in the focal point of the schlieren head could be considered as the essential "schlieren effect". Many alterations of the Toepler method, which uses the knife edge for such a manipulation, have been proposed and realized. In the proposed systems the light wave is manipulated with respect to its intensity (like in the Toepler system), or its phase ("dephasing schlieren systems"), or its color ("color schlieren systems"). The aim of these methods can be: increase of the optical sensitivity in resolving small density changes; visualization of the deflection in different directions; providing a signal which is more suitable for a quantitative measurement.

In the "dark field" system, the conventional knife edge is replaced by an opaque diaphragm or stop cutting off symmetrically all but a very small fraction of the undisturbed light source image. The undisturbed field appears with a very reduced intensity (dark field). When a point source is used, the schlieren stop has to be a small circular diaphragm (Fig. 8.6). All deflection angles of the same absolute value produce the same contrast, regardless of their orientation in the x-y plane. Dark field systems have been studied extensively by Wolter [8.5]. The opaque schlieren stop can be made by taking photographs of the light source image at different exposure times and then using the appropriate negative [8.15]. Since the sharp edge of the stop enhances the diffractive noise, it has been proposed to employ a stop with a gradual variation of its transparency (from 1 to 0); such gradual filters can be fabricated either by coating a piece of glass or by photographic means [8.20].
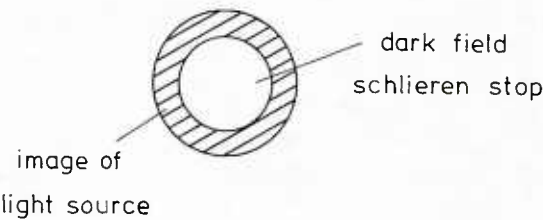
Fig. 8.6:  Dark-field schlieren stop

Probably the most spectacular flow photographs can be obtained with color schlieren systems. These systems require the use of a white light source. Light deflections in the test field are converted into colors by respective elements in the focal plane of the schlieren head. A few of such elements are listed in Table 8.1, together with representative references. Additional possibilities for introducing color in a schlieren system may be found in the reviews of Schardin [8.3] and Settles [8.8]. Colors allow for easily discriminating between positive and negative deflection angles (e.g. with the three-color-filter), or for recognizing the direction of light deflection in the x-y plane (with the multi-color-filter). With a dispersion prism or a diffraction grating one is restricted to the natural sequence of colors in the visible spectrum.

Table 8.1

Color schlieren system

| optical element providing color | visualization of | reference |
|---|---|---|
| tri-color filter | | Kessler and Hill [8.21] |
| dispersion prism | $\frac{\partial \rho}{\partial y}$ | Holder and North [8.22] |
| diffraction grating | | Maddox and Binder [8.23] |
| multi-directional color-filter | | Settles [8.24] |
| rainbow filter ("bull's eye filter") | $\frac{\partial \rho}{\partial x}$ and $\frac{\partial \rho}{\partial y}$ | Howes [8.25] |

A number of modifications of the schlieren system are known, in which a certain portion of the light source image in the focal plane of the schlieren head is shifted in phase. A shift of one-half of this light by an angle of 180°, realized by a respective phase plate, results in a dark field of view due to the interference of the light having passed through the phase plate with the unshifted light [8.26 - 8.28]. The purpose of manipulating the phase in the focal point of the schlieren head is, in most cases, an increase of the optical sensitivity at low density flow conditions. It is not always clear whether one should regard such systems as a schlieren system or an interferometer; see, e.g., [8.29, 8.30].

The latter is particularly true for the phase contrast method. In the focal point of the schlieren head, a minute phase plate that coincides with the zeroth-order diffractive image of the source changes the phase of the zeroth-order light by an angle of 9o°. This technique, originally developed for being used in microscopy of phase objects, re-

solves small changes of the optical phase with much higher contrast than the Toepler schlieren method or any interferometer [8.10, 8.13, 8.31-8.33]. With small optical phase change or at a low density level, a record taken with the phase contrast method has the appearance of a schlieren record (Fig. 8.7). At an elevated density level, fringes appear in the field of view, and the record is equivalent to a reference beam interferogram, the fringes being curves of constant density when the flow is two-dimenstional.
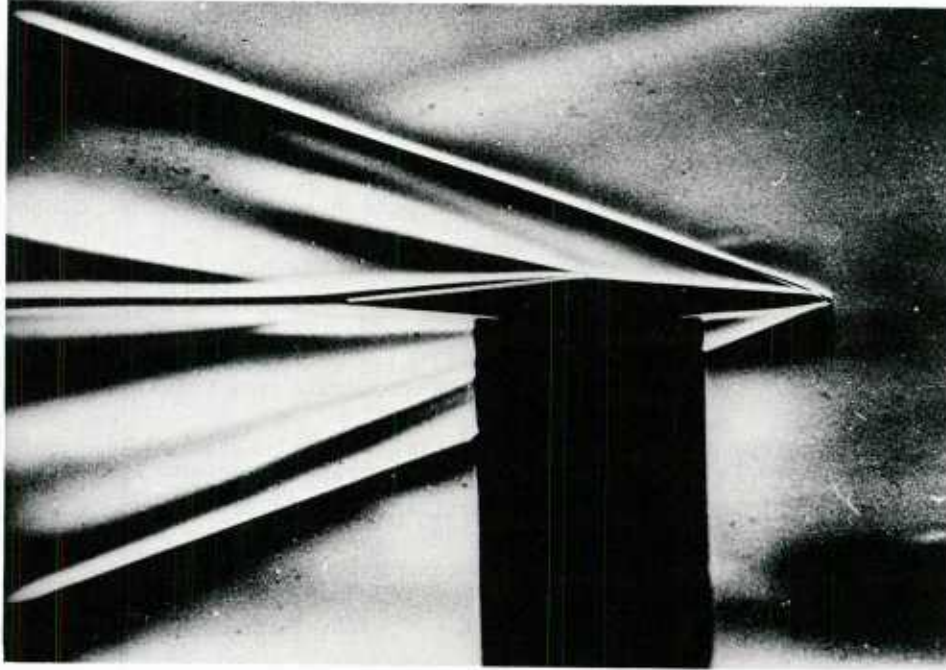


Fig. 8.7: Phase-contrast recording of the supersonic flow (M = 3.74) over a two-dimensional profile (M. Philbert, ONERA, France [8.1o]).
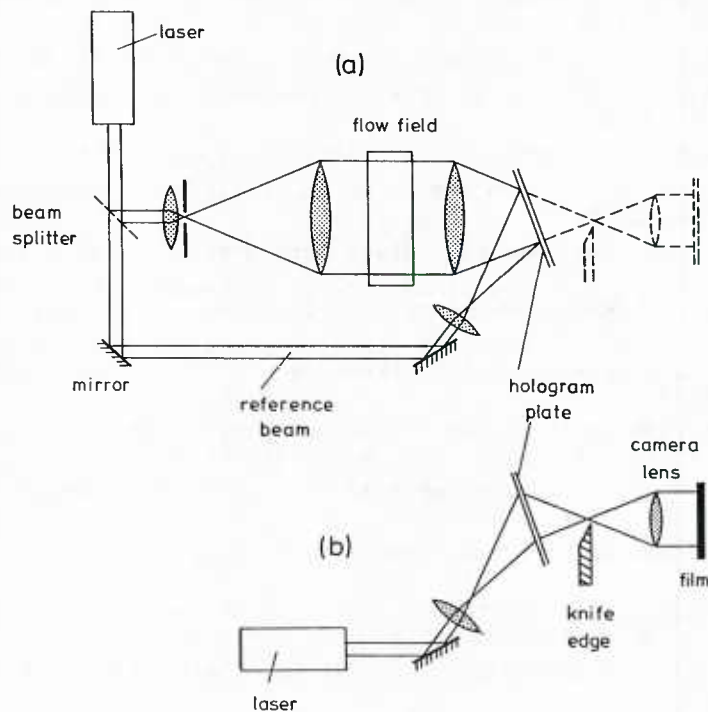


Fig. 8.8: Schlieren system in combination with holographic recording. (a): Recording of the hologram ; (b): reconstruction of the hologram and visualization in a schlieren system. (see also [8.34]).

60

The schlieren method, as any other optical visualization system, can be combined with a holographic set-up. If one takes a hologram through the test field, one may freeze the instantaneous information of the refractive index field. When the test field is reconstructed from the hologram, it may be observed with the suitable optical method. Fig. 8.8 shows the principal arrangement for taking such a hologram, and for observing the reconstructed test field with a schlieren system [8.34]. Such a postponed visualization is of great interest when the test flow is unsteady and does not allow for adjusting the optical system during the exeriment. The reconstruction provides practically unlimited time for choosing the appropriate method and the most suitable adjustment [8.35].

References

8.1. Toepler, A.: Beobachtungen nach einer neuen optischen Methode. Max Cohen & Sohn, Bonn, 1864.

8.2. Schardin, H.: Das Toeplersche Schlierenverfahren. VDI-Forschungsheft No. 367, 1934.

8.3. Schardin, H.: Die Schlierenverfahren und ihre Anwendungen. Ergeb. Exakten Naturwiss. 2o (1942), 3o3-449.

8.4. Beams, J.W.: Shadow and schlieren methods. In: Physical Measurements in Gas Dynamics and Combustion (ed. R.W. Ladenburg), pp. 26-46, Princeton Univ. Press, Princeton, N.J., 1954.

8.5. Wolter, H.: Schlieren, Phasenkontrast und Lichtschnittverfahren. In: Handbuch der Physik (ed. S. Flügge), Vol. 24, pp. 555-645, Springer-Verlag, Berlin, 1956.

8.6. Holder, D.W.; North, R.J.; Wood, G.P.: Optical methods for examing the flow in high-speed wind-tunnels. AGARDograph No. 23, 1956.

8.7. Holder, D.W.; North, R.J.: Schlieren Methods. Notes on Applied Science No. 31, HM Stationary Office, London, 1963.

8.8. Settles, G.S.: Color schlieren optics - A review of techniques and applications. In [1.5], pp. 749-759, 1982.

8.9. North, R.J.; Stuart, C.M.: Flow visualization and high-speed photography in hypersonic aerodynamics. Proceed. 6th Int. Congr. High-Speed Photogr., pp. 470-477, 1963.

8.1o. Philbert, M.: Visualisation des écoulements à basse pression. Rech. Aérosp. No. 99 (1964), 39-48.

8.11. Merzkirch, W.: Sensitivity of flow visualization methods at low-density flow conditions. AIAA J. 3 (1965), 794-795.

8.12. Oudin, L.; Lavirotte, C.: Contribution à l'étude théorique de la sensibilité de la strioscopie. ISL T 58/68, 1968.

8.13. Véret, C.: Visualisation à faible masse volumique. AGARD CP-38 (1970), 257-264.

8.14. Hosch, J.W.; Walters, J.P.: High spatial resolution schlieren photography. Appl. Opt. 16 (1977), 473-482.

8.15. Stanic, S.: Quantitative schlieren visualization. Appl. Opt. 17 (1978), 837-842.

8.16. Prescott, R.; Gayhart, E.L.: A method of correction of astigmatism in schlieren systems. J. Aerospace Sci. 18 (1951), 69.

8.17. Albe, F.: L'astigmatisme dans le montage strioscopique. ISL T 49/68, 1968.

8.18. Slattery, R.E.; Clay, W.G.; Ferdinand, A.P.: High-speed photographic technique in a ballistic range. Proceed. 8th Int. Congr. High-Speed Photogr. pp. 351-356, 1968.

8.19. Royer, H.; Smigielski, P.: Méthodes strioscopiques appliqués à l'étude des sillages hypersoniques à basse pression. Proceed. 8th Int. Congr. High-Speed Photogr., pp. 359-361, 1968.

8.20. Kent, J.C.: Fabrication of graded filters for knife-edge replacement in laser schlieren optical systems. Appl. Opt. 8 (1969), 2148-2149.

8.21. Kessler, T.J.; Hill, W.G.: Schlieren analysis goes to color. Aeronautics and Astronautics 4 (1966), 38-4o.

8.22. Holder, D.W.; North, R.J.: A schlieren apparatus giving an image in color. Nature 169 (1952), 466.

8.23. Maddox, A.R.; Binder, R.C.: A new dimension in the schlieren technique: Flow field analysis using color. Appl. Opt. 1o (1971), 474-481.

8.24. Settles, G.S.: A direction-indicating color schlieren system, AIAA J. 8 (1970), 2282-2284.

8.25. Howes, W.L.: Rainbow schlieren and its applications. Appl. Opt. 23 (1984), 2449-246o.

8.26. Oudin, L.; Smigielski, P.: Strioscopie par soustraction d'amplitudes. Etude mathématique. ISL T 41/69, 1969.

8.27. Royer, H.: Strioscopie par soustraction d'amplitudes. ISL T 36/69, 1969.

8.28. Royer, H.: A new method of visualizing and measuring hypersonic wakes. A schlieren arrangement using amplitude subtraction. Proceed. 9th Int. Congr. High-Speed Photogr., pp. 41o-413, 197o.

8.29. Rowe, A.J.; Khan, G.M.: A comparison of results from phase plate and knife edge diaphragms in conjunction with the schlieren optical system in an MSE analytical ultracentrifuge. Rev. Sci. Instrum. 42 (1971), 1472-1474.

8.30. Prikryl, I.; Vest, C.M.: Hybrid processing for phase measurement in metrology and flow diagnostics. Appl. Opt. 22 (1983), 2844-2849.

8.31. Taylor, M.W.: An application of the method of phase contrast to gas flow visualization. AIAA Paper 8-0865, 1980.

8.32. Anderson, R.C.; Taylor, M.W.: Phase contrast flow visualization. Appl. Opt. 21 (1982), 528-536.

8.33. Anderson, R.C.; Lewis, S.: Flow visualization by dark central ground interferometry. Appl. Opt. 24 (1985), 3687.

8.34. Trolinger, J.D.: Laser instrumentation for flow field diagnostics. AGARDograph No. 186, 1974.

8.35. Smigielski, P.; Hirth, A.: New holographic studies of high-speed phenomena. Proceed. 9th Int. Congr. High-Speed Photogr., pp. 321-326, 197o.

## 9. MOIRÉ METHODS AND SPECKLE PHOTOGRAPHY

Many attempts have been made in modifying a schlieren system such that the form of the signal is more suitable for a quantitative evaluation. A common feature of all these attempts is that one generates, in the undisturbed field of view, a more or less regular reference pattern, which is then disturbed in the presence of the refractively disturbing flow. A comparison of the disturbed pattern with the undisturbed reference pattern allows for measuring and mapping the deflection angles in the whole field of view ("moiré pattern"). The pattern most frequently used is a system of parallel, equidistant fringes produced, e.g., by inserting a grid or a system of equally spaced wires in the path of the light beam.

Holder and North [8.7] have investigated the case when a grid is placed between the schlieren head and its focal point (Fig. 9.1). An imaging lens in or near the focal point
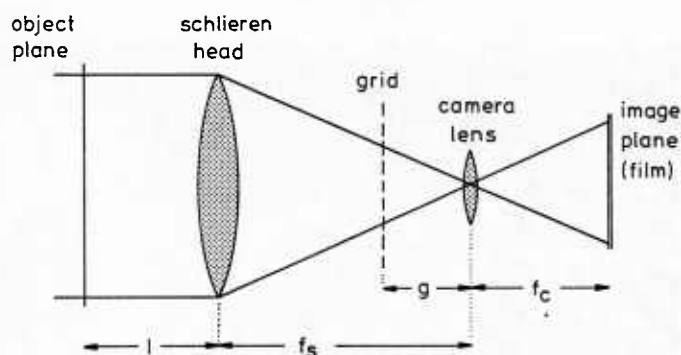


Fig. 9.1.: Deflection mapping system with a grid.

focuses a plane in the flow onto the recording plane. If a density variation is present in the flow, the fringes appearing in the recording plane are not straight but distorted, the distortion (fringe shift) being proportional to the amount of light deflection. Such a fringe pattern is equivalent to the pattern observed with the "finite fringe width alignment" of a shearing or schlieren interferometer (see chapter 1o). If the fringe distortion is measured normal to the direction of the undisturbed fringes, in Fig. 9.1 assumed to be parallel to the x-axis, the absolute fringe shift $\Delta s_y$ is related to the component $\varepsilon_y$ of the deflection angle by (see [8.7])

$$\Delta s_y = \varepsilon_y \left\{ f_s \frac{f_c}{g} + (1-f_s) \frac{g}{f_s} \right\} \qquad . \qquad (9.1)$$

The notation of this equation follows from Fig. 9.1. The fringe shift does not depend on the absolute spacing of the grid. For g → 0 the system approaches the Toepler schlieren set up.

Systems like that in Fig. 9.1 have been applied to flow situations with not too small density variations, e.g. flames (an example is given in Fig. 9.2), shock waves [9.1], or stratified flow in salt water [9.2]. Dewey [9.3] has demonstrated the usefullness of this method for observing large-scale, openair shock configurations (Fig. 9.3).



Fig. 9.2: Deflection mapping in the field of a laminar flame by using a grid of equally spaced wires.
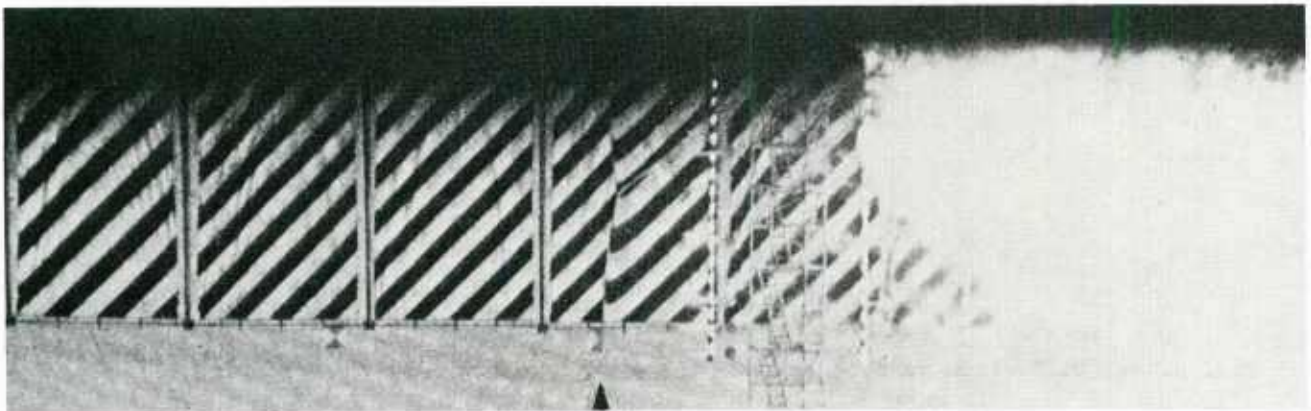


Fig. 9.3: Shock waves produced by the explosion of two 5oo kg charges. The shock wave is seen against a striped background (J.M. Dewey and D.J. McMillin, University of Victoria, B.C., Canada; see also [9.3].

Moiré patterns generated by the superposition of two fine grids of equal spatial frequency, but rotated at a certain angle, have been described and extensively discussed by Kafri and his co-workers; see, e.g., [9.4-9.7]. These systems, which they used mainly for the study of flames, present additional degrees of freedom in alignment in comparison to the set-up with only one simple grid (Fig. 9.1).

The moiré pattern is a large-scale pattern, in contrast to the micro-sized pattern produced by a method based on speckle photography. The principles of speckle photography have been outlined already in chapter 5. Köpf [9.8] and Debrus et al. [9.9] describe the adoption of this principle to the measurement of refractive index fields. The idea is that a microsized reference pattern is produced by illuminating and imaging a plate of ground glass on the recording plane, and that this pattern is distorted due to the presence of the refractively disturbing flow field and can later be analyzed by the respective techniques used in speckle photography. The optical systems used in [9.8] and [9.9] suffer from a possible decorrelation of the two patterns when the deflection angles of the transmitted light exceed a certain value.

An optical set-up which overcomes this defect is shown in Fig. 9.4, see [9.10]. The principle of the method will be explained with this system. The light from a laser source is expanded and transmitted in form of a parallel beam through the flow field. A lens focuses a plane of the test field onto the ground glass plate. A second imaging lens focuses a plane at distance l from the ground glass onto the recording plane (photographic plate). Two exposures are taken on the same plate: First, a reference exposure in the absence of the flow; and a second exposure with the flow to be tested in place, as shown in Fig. 9.4. The first exposure generates on the photographic plate a speckle pattern which is determined by the structure and the scattering characteristics of the ground glass. This pattern is distorted in the second exposure due to the light deflection in the test flow. The displacement of each individual speckle between the two exposures is a measure of the local deflection angle $\varepsilon(x,y)$; x,y being the coordinates in the recording plane (field of view). Due to the imaging of the test field on the ground glass, a light ray, deflected by an angle $\varepsilon$ in the test flow, will arrive at the ground glass at the same point where the corresponding, undisturbed ray of the reference exposure has arrived (see Fig. 9.4). However, the two rays form an angle $\varepsilon$ between each other, if a 1:1 imaging ratio is chosen. In the plane at distance l from the ground glass, the two rays are separated by $ds = \varepsilon \cdot l$. At the same time, ds is the displacement of the recorded speckles
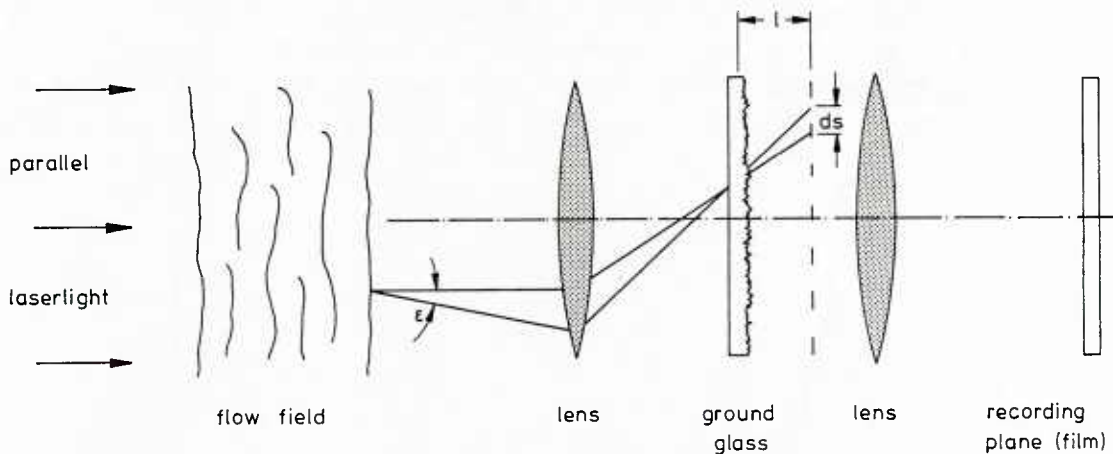


Fig. 9.4: Deflection mapping by speckle photography. Speckles are produced by the ground glass. The plane at distance l from the ground glass is imaged onto the recording plane (see [9.10]).

in the double exposure, and the distribution ds(x,y) can be determined with the point-by-point reconstruction technique via an evaluation of the respective systems of Young's fringes (see chapter 5.2 and Fig. 5.6). The system of Fig. 9.4 is equivalent to the speckle photographic measurement of inclination angles [9.11]. The distance l has to be chosen such that the recorded speckle patterns are always correlated, i.e., l must be decreased if the deflection angle $\varepsilon$ increases, and it is thus possible to investigate extended flow fields producing large values of $\varepsilon$, which was not possible with the original arrangements used by Köpf [9.8] and Debrus et al. [9.9].

In contrast to the schlieren method, this speckle photographic system is a means
for quantitatively measuring the distribution of the deflection angle $\varepsilon(x,y)$. In one ex-
periment, i.e. in one double exposure, the displacement ds is measured as a vector, and
the two components of the deflection angle, $\varepsilon_x$ and $\varepsilon_y$, are therefore measured simultane-
ously. They can be converted into the respective derivatives of the refractive index or
fluid density, see Table 6.3. The quantitative results are comparable to those which can
be obtained from a shearing or schlieren interferogram (see chapter 1o). But the number
of data points obtainable per square unit of the speckle record is much higher than in
the case of an interferogram. For, in the latter case the derivation of data is restric-
ted to the existence of an interference fringe, whereas the micro-sized speckle pattern
allows for a quantitative evaluation in practically any point of the field of view. The
usefulness of the speckle method has been proven with applications to flames [9.12], con-
vective heat transfer [9.13] and mass transfer [9.14].

While the latter references are applications to laminar flow problems, it has been
demonstrated by Wernekinck et al. [9.15], that the method even can be used for resolving
the light deflection in turbulent flow with fluctuating density. The system must then be
operated with a pulsed light source, e.g. a ruby laser. It is thus possible to map the
randomly distributed deflection angles and to provide quantitative information from a
turbulent flow field, which, in most cases, is not possible with an interferometer due
to the usual blurring of the interference fringes. In addition to this principal availa-
bility of quantitative data, a very dense distribution of the information, i.e. values
of the deflection angle $\varepsilon(x,y)$, can be obtained from the micro-sized speckle pattern.
An automated evaluation system as mentioned in chapter 5.2 is of great advantage. It is
therefore possible to analyze the plane distribution $\varepsilon(x,y)$ by means of an appropriate
statistics.

Erbeck [9.16] (see also [9.17]) has determined the correlation function of the de-
flection angles $\varepsilon$ measured in a slightly heated wind tunnel flow with grid turbulence.
Such a flow is assumed to have homogeneous, isotropic turbulence. An interesting result
is, that the correlation coefficient $R_\varepsilon^*$ is always positive when the components of $\varepsilon$,
which are correlated with eachother, are orthogonal to the direction of correlation, while
the correlation coefficient can become negative when two components being parallel to that
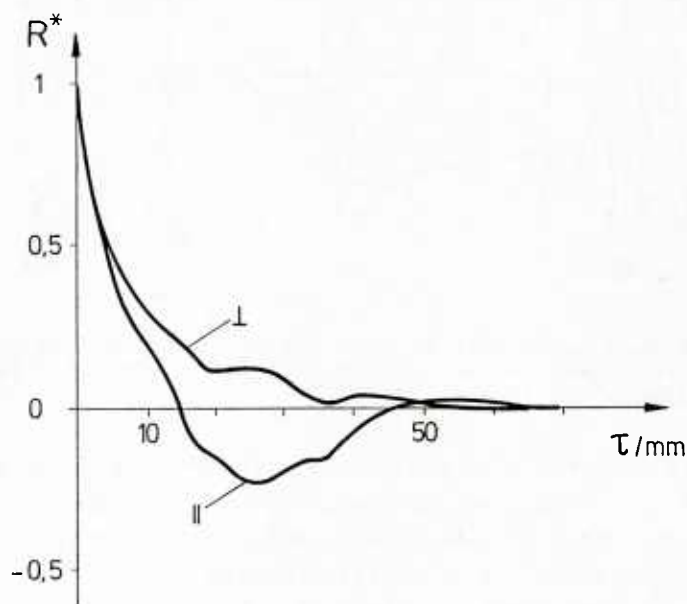direction are correlated (Fig. 9.5). This result is verified with a visualization of this



Fig. 9.5: Spatial correlation coefficient R* of the deflection angle $\varepsilon$ of light passing
through a turbulent flow with temperature fluctuations. The correlation compo-
nents of $\varepsilon$ are parallel ($\|$) or normal ($\perp$) to the direction of correlation.
$\tau$ is the distance of correlation (see [9.16, 9.17]).

flow by spatial filtering (see below). In [9.16, 9.17] it is shown, that the earlier idea of Uberoi and Kovasznay [7.6] for providing statistical information on the three-dimensional density field can be realized. A mathematical algorithm and the assumption of homogeneous, isotropic turbulence allow for determining the spatial correlation of the temperature (or density), $R_T^*$, from $R_\varepsilon^*$ (Fig. 9.6). This result is a true spatial correlation, in contrast to measurements taken with a cold wire probe in the same flow, which need the application of Taylor's hypothesis for the spatial correlation. At the same time, this result is a clear demonstration of the advantages of an optical whole field method in application to a turbulent flow.
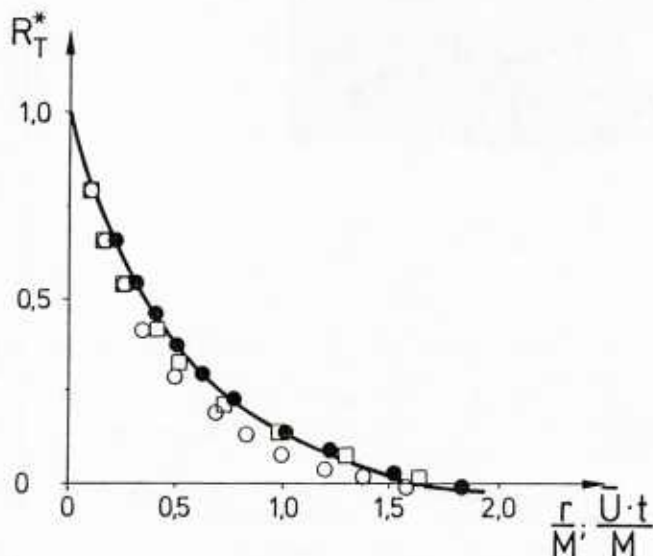


Fig. 9.6: Spatial correlation coefficient of the temperature as calculated from the result shown in Fig. 9.5. M = 4o mm is the mesh size of the grid used for generating grid turbulence. The indicated data points refer to various probe measurements for which it was necessary to assume a constant mean velocity $\bar{U}$ (see [9.16, 9.17]).

The specklegram taken from a refractive index field can also be analyzed with the spatial filtering technique (see chapter 5.2 and Fig. 5.1o). The result compares to a schlieren pattern (Fig. 9.7). The reconstruction of the aforementioned flow of homogeneous, isotropic turbulence by means of spatial filtering in y-direction (Fig. 9.8) verifies the different patterns of the two correlation functions in Fig. 9.5: The figure shows more frequent changes in sign of intensity (dark/bright) when it is traced in vertical direction (symbol || in Fig. 9.5), i.e. possible negative values of R*, while there are only few changes in sign when the figure is traced in horizontal direction (symbol |); again a proof of the possibility of directly visualizing statistical characteristics of a turbulent flow.
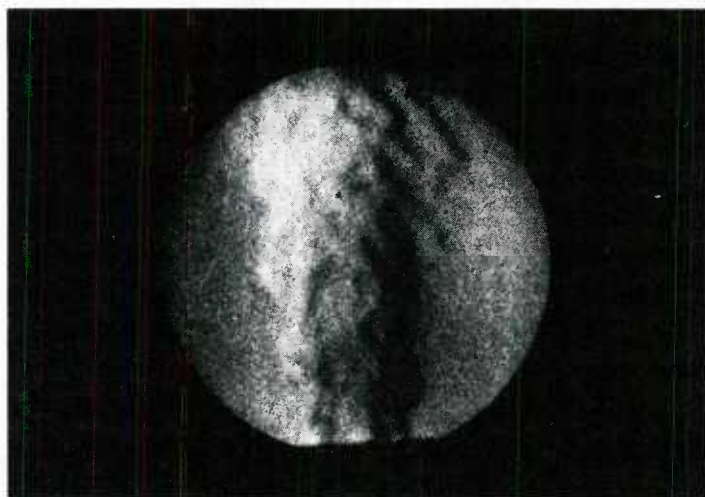


Fig. 9.7: Spatial filtering of a specklegram taken of a turbulent jet of helium exhausting vertically into the ambient air.

Fig. 9.8: Spatial filtering of a specklegram taken of an air flow with fluctuating temperature and homogeneous, isotropic turbulence (grid turbulence) (K.Oberste-Lehn, Universität Essen, F.R. Germany).

References

9.1. Thompson, P.A.; Kim, Y.G.; Meier, G.E.A.: Flow visualization of a shock wave by simple refraction of a background grid. In: Optical Methods in Dynamics of Fluids and Solids (ed. M. Pichal), pp. 225-231, Springer-Verlag, Berlin, 1985.

9.2. Thorpe, S.A.: Experiments on instability and turbulence in a stratified shear flow. J. Fluid Mech. 61 (1973), 731-751.

9.3. Dewey, J.M.;McMillen, D.J.; Classen, D.K.: Photogrammetry of spherical shocks reflected from real and ideal surfaces. J. Fluid Mech. 81 (1977), 7o1-717.

9.4. Kafri, O.: Noncoherent method for mapping phase objects. Optics Letters 5 (1981), 555-557.

9.5. Stricker, J.; Kafri, O.: A new method for density gradient measurements in compressible flows. AIAA J. 2o (1983), 82o-832.

9.6. Bar-Ziv, E.; Sgulim, S.; Kafri, O.; Keren, E.: Temperature mapping in flames by moiré deflectometry. Appl. Opt. 22 (1983), 698-7o5.

9.7. Rau, G.S.; Bar-Ziv, E.: Deflection mapping of flames using the moiré effect. Appl. Opt. 23 (1984), 2686-2692.

9.8. Köpf, U.: Application of speckling for measuring the deflection of laser light by phase objects. Opt. Commun. 5 (1972), 347-35o.

9.9. Debrus, S.; Francon, M.; Grover, C.P.; May, M.; Roblin, M.L.: Groundglass differential interferometer. Appl. Opt. 11 (1972), 853-857.

9.1o. Wernekinck, U.; Merzkirch, W.: Speckle photography of spatially extended refractive-index fields. Appl. Opt. 26 (1987), 31-32.

9.11. Ennos, A.E.: Comparative accuracy of holographic interferometry and speckle photography for out-of-plane deformation measurement. Opt. Commun. 33 (198o), 9-12.

9.12. Farrell, P.V.; Hofeldt, D.L.: Temperature measurement in gases using speckle photography. Appl. Opt. 23 (1984), 1o55-1o59.

9.13. Sivasubramanian, M.S.; Cole, R.; Sukenek, P.C.: Optical temperature gradient measurements using speckle photography. Int. J. Heat Mass Transfer 27 (1984), 773-78o.

9.14. Wernekinck, U.; Merzkirch, W.: Measurement of natural convection by speckle photography. In: Heat Transfer 1986 (eds. C.L. Tien, V.P. Carey, J.K. Ferrell), pp. 531-535, Hemisphere, Washington, 1986.

9.15. Wernekinck, U.; Merzkirch, W.; Fomin, N.A.: Measurement of light deflection in a turbulen density field. Exp. Fluids 3 (1985) 2o6-2o8.

9.16. Erbeck, R.: Die Anwendung der Speckle-Photographie zur statistischen Analyse turbulenter Dichtefelder. VDI-Fortschritt Bericht, Reihe 8, Nr. 112, VDI-Verlag, Düsseldorf, 1986.

9.17. Erbeck, R.; Merzkirch, W.: Speckle photographic measurement of turbulence in an air stream with fluctuatingtemperature. Preprints 1oth Symposium on Turbulence, pp. 2/1 - 2/6, University of Missouri-Rolla, 1986 (to appear in Exp. Fluids).

10. WOLLASTON PRISM SCHLIEREN INTERFEROMETER

Instruments belonging to the class of shearing interferometers provide the same kind

of information on the density field as the methods discussed in the previous sections, i.e., the signal obtained from a shearing interferogram is a function of the refractive index gradient or the density gradient in the test flow. The description of a system is based on the assumption that two slightly sheared light beams are transmitted through the refractive index field (Fig. 1o.1). The optical set-up of many shearing interferometers is similar to that of a schlieren system; therefore, the name "schlieren interferometer" has become popular. Among a great number of interferometric systems (see, e.g., [1o.1, 1o.2], an arrangement with a Wollaston prism as the shearing element is most frequently used in experimental fluid mechanics, gasdynamics, and aerodynamics. Only this system will be discussed in this chapter.
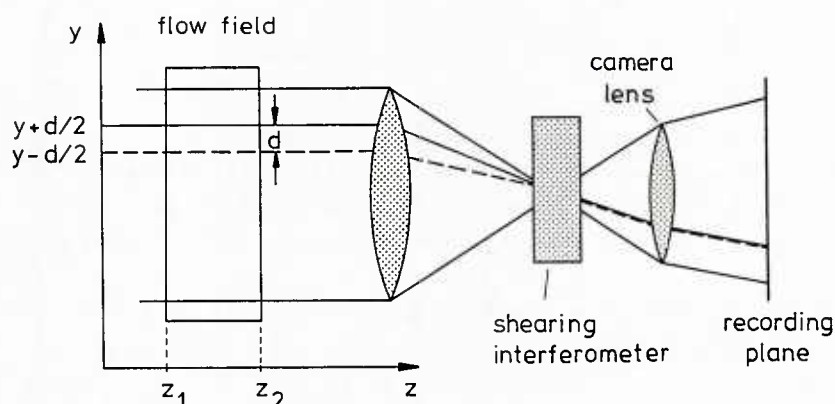


Fig. 1o.1: Principle of a shearing interferometer

In contrast to the methods described in chapter 8 and 9, the signal obtained with a shearing interferometer is caused by the changes of the optical phase of light waves passing through the flow, and not by light deflection. Two parallel, laterally sheared light rays passing through the test flow at positions $(y+\frac{d}{2})$ and $(y-\frac{d}{2})$ are considered (Fig. 1o.1). The "shearing element" positioned in or near the focal point of the schlieren head provides that the two rays coincide after they have passed through this element. Under the assumption that the conditions of optical coherence are fulfilled, the two coinciding light rays can interfere with eachother. If the refractive indices n (or the fluid densities $\rho$) at the coordinates $(y+\frac{d}{2})$ and $(y-\frac{d}{2})$ in the flow are not equal, the two light rays (or waves) exhibit a difference in their optical path, $\Delta l$, given by

$$\Delta l(x,y) = \int_{z_1}^{z_2} n(x,y+\tfrac{d}{2},z)\,dz - \int_{z_1}^{z_2} n(x,y-\tfrac{d}{2},z)\,dz \quad . \tag{1o.1}$$

This equation is derived under two assumptions: First, the coordinates where the rays enter and leave the flow, $z_1$ and $z_2$, are equal for the two rays; i.e., the flow is bounded by plane walls (deviations from this situation are easy to handle). Second and more important: The propagation of light in the flow is straight and undeflected. This assumption is reasonable for most gas flows, but it might be violated in liquid flows and in gases with very strong density gradients (e.g. in a plasma flow). Exceptions from the validity of this assumption, known as "strong refraction effects", will not be discussed here. The situation then is much more complicated, because not only the refractive index or the density, but also the path of the light in the flow is unknown.

In a shearing interferometer, the shear or the separation of the two considered light rays, d, is assumed to be very small, e.g. in comparison to the diameter of the field of view. The right hand side of eq. (1o.1) can be developed into a Taylor series around n(x,y,z). Taking into account only the linear term (the quadratic term vanishes), because d is small, yields

$$\Delta l(x,y) = d \cdot \int_{z_1}^{z_2} \frac{\partial}{\partial y} n(x,y,z) \ dz \qquad\qquad (1o.2)$$

The quantitiy $\Delta l(x,y)$ is measured in the recording plane in form of interference fringes. Bright fringes appear where

$$\frac{1}{\lambda} \cdot \Delta l(x,y) = 0, \ \pm 1, \ \pm 2, \ \ldots, \qquad\qquad (1o.3)$$

with $\lambda$ being the light wave length. The equation of the dark fringes is

$$\frac{1}{\lambda} \cdot \Delta l(x,y) = \pm \frac{1}{2}, \ \pm \frac{3}{2}, \ \ldots \qquad\qquad (1o.4)$$

It is seen that the measured signal, the left hand side of eqs. (1o.3) and (1o.4), is two-dimensional, whereas the quantity to be determined, $n(x,y,z)$, is three-dimensional in the general case. A direct measurement of n is possible for a plane refractive index field, $n(x,y)$. Methods for deriving the three-dimensional distribution of n (or $\rho$) from the plane information (interferogram, specklegram) will be discussed in chapter 12.

The dependence of the measured signal on the gradient of the refractive index, like in the methods which rely on the measurement of the deflection angle $\varepsilon$, is obvious from eq. (10.2). The measurement of $\partial n/\partial x$ is possible by rotating the optical system by $9o°$ around the optical axis (z-axis).

From eq. (1o.2) it follows that an interferogram with $\partial n/\partial y$ = const will appear uniformly illuminated; all light waves arrive in the recording plane with the same optical phase. This case is called the "infinite fringe width" alignment of the interferometer. It can be aligned in a different way, so that a system of equidistant, parallel interference fringes appears for the object with $\partial n/\partial y$ = const. This "finite fringe width" alignment is, in principle, the superposition of an artificial object with $(\partial n/\partial y) = a \cdot x + b \cdot y$ (a,b determine the direction of these fringes in the x-y plane). A density variation in the flow will distort this regular fringe pattern, and the deviation or shift of a fringe from its undisturbed position is a measure of the density disturbance. A fringe shift by one fringe width is equivalent to a difference in optical path length by one wavelength. It follows that a fringe shift $\Delta S$ in a point $(x,y)$, measured in terms of the fringe width S of the undisturbed equidistant pattern, is

$$\frac{1}{S} \cdot \Delta S(x,y) = \frac{d}{\lambda} \int_{z_1}^{z_2} \frac{\partial}{\partial y} n(x,y,z) \ dz \quad . \qquad\qquad (1o.5)$$

The fringe shift $\Delta S(x,y)$ is now the signal to be measured in the interferogram. The curves connecting the points in which the disturbed fringes intersect with the undisturbed fringes of the finite fringe width case are identical with interference fringes of the infinite fringe width alignment.

Which of the two alignments is preferable depends on the particular test situation. For a comparison of the two cases, Fig. 1o.2 to 1o.7 show the same test object, the laminar plume raising from a candle flame, in the infinite and the finite fringe width mode. This flow has a much stronger density (or temperature) gradient in horizontal (radial) direction than in vertical (axial) direction. From these figures it becomes obvious how the different alignments of the interferometer in terms of rotation of the shearing element (Wollaston prism) react to these gradients. In the finite fringe width alignment, the density gradient is always measured in a direction perpendicular to the undisturbed, parallel fringes. The Wollaston prism interferometer was originally developed for use in

Fig. 1o.2:  Schlieren interferogram of a
laminar candle flame; fringes
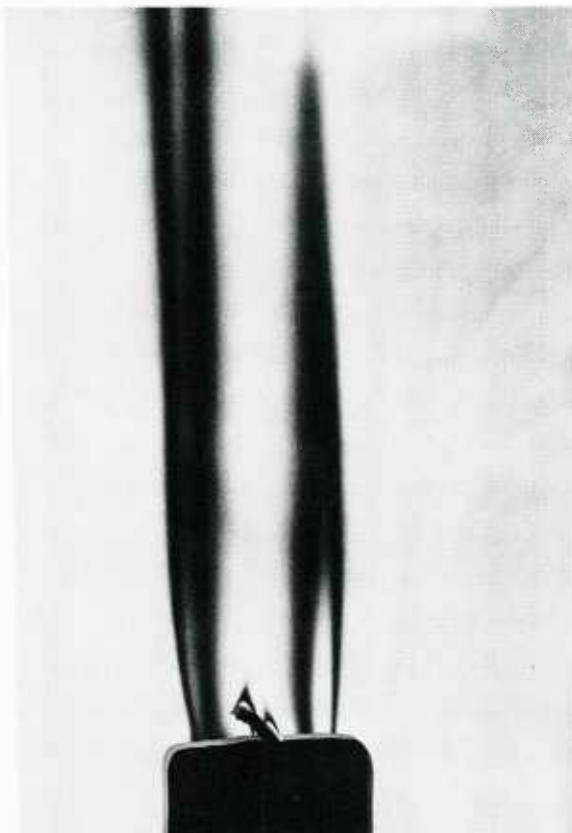oblique finite fringe width.

Fig. 1o.3:  Same as Fig. 1o.2; infinite
fringe width.

Fig. 1o.4:  Laminar candle flame; fringes
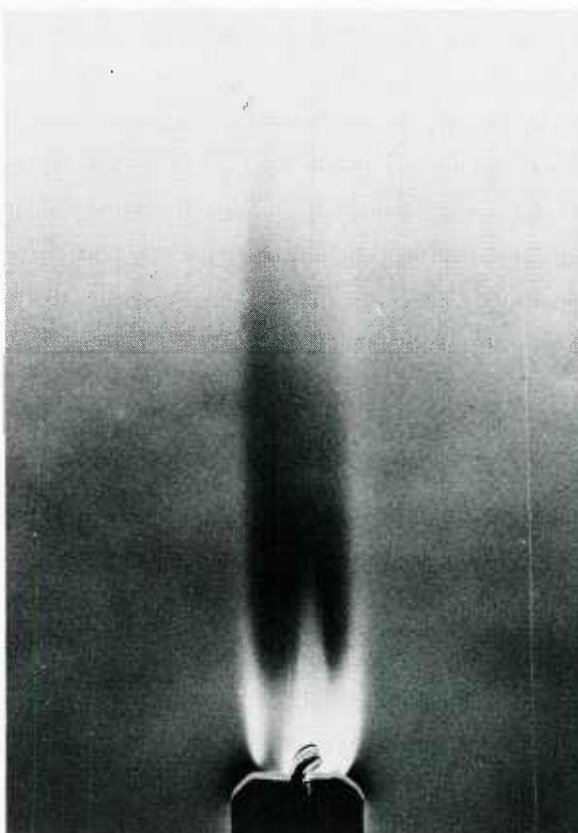horizontal, finite fringe width.
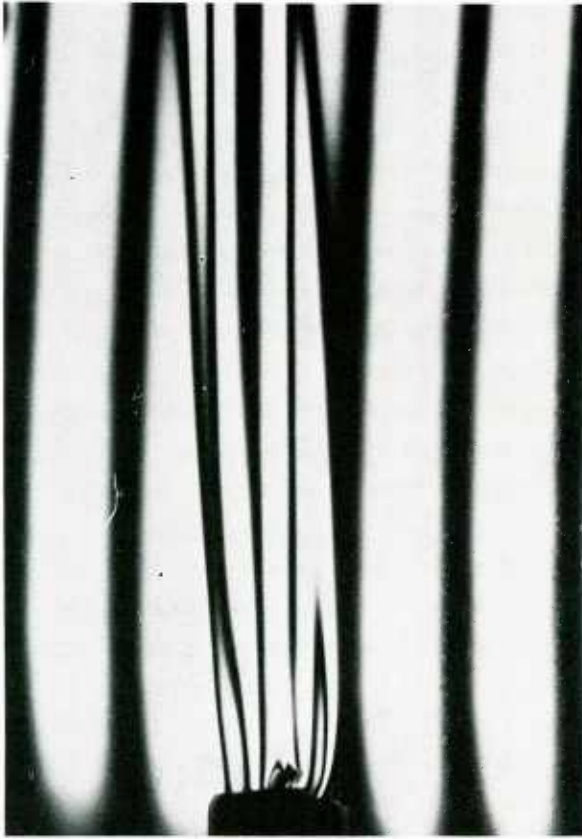
Fig. 1o.5:  Same as Fig. 1o.4; infinite
fringe width.

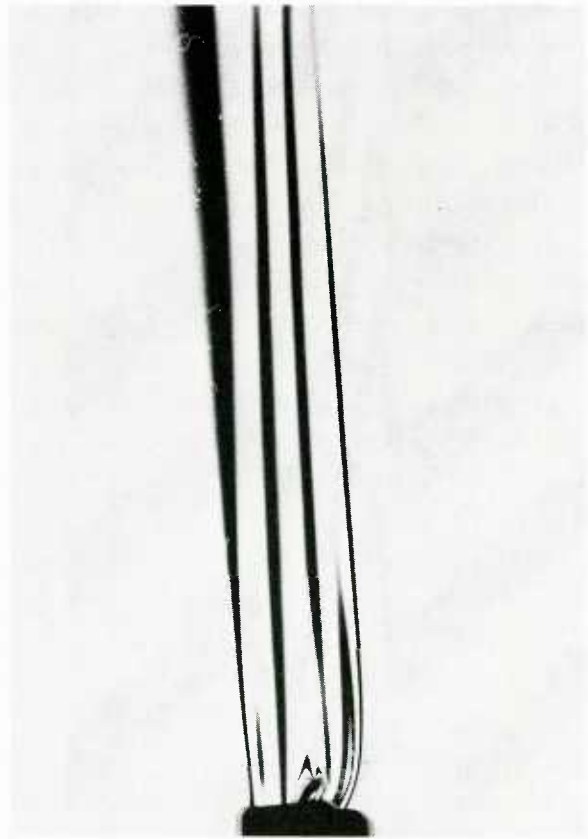Fig. 1o.6: Laminar candle flame; fringes vertical, finite fringe width.

Fig. 1o.7.: Same as Fig. 1o.6, infinite fringe width.

interference microscopes [1o.3]. Various authors have adopted this principle for the visualization of compressible flows and have given extented descriptions of the system, e. g. [1o.4 - 1o.1o]. The optical set-up is very similar to a schlieren system (Fig. 1o.8).
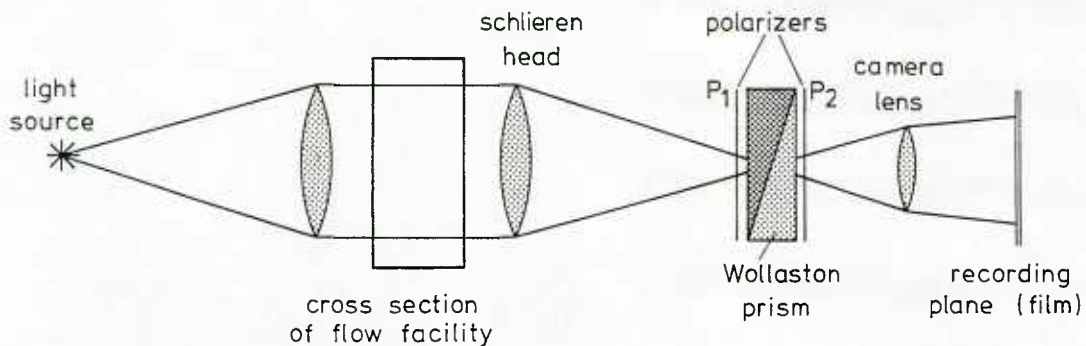


Fig. 1o.8: Schlieren interferometer using Wollaston prism as the shearing element.

The knife edge known from the Toepler system is replaced here by a prism unit consisting of the Wollaston prism and two crossed polarizers. In the fundamental or infinite fringe width alignment, the center of the Wollaston prism coincides with the focal point of the lens or spherical mirror that was previously called the "schlieren head". The role of the Wollaston prism (which actually consists of two prism halfs glued together) as the shearing element is explained with the aid of Fig. 1o.9. A light ray entering the prism is separated into two components forming an angle $\beta$ with eachother. This angle is determined by the characteristics of the prism, and, within the accuracy of a first-order analysis, $\beta$ is independent of the direction of incidence. The two components leaving the prism are linearly polarized, the directions of polarization being perpendicular to eachother. In Fig. 1o.9, the incident ray 1 is separated into the two components 1' and 1°, where the symbols ' and ° indicate a linear polarization in the plane of the figure and normal to this plane, respectively. In the incident converging light beam, there is a
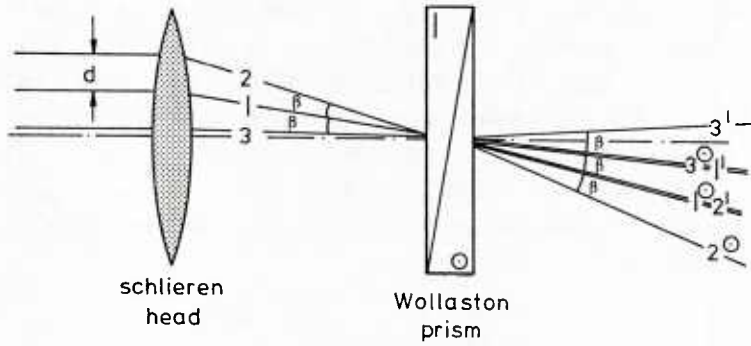
Fig. 1o.9: Separation of incident light rays in the Wollaston prism. The symbols ' and $^o$ designate linear polarization in the plane and normal to the plane of the figure.

ray 2 including the angle $\beta$ with 1, and being separated into 2' and $2^o$. The separated ray 2' coincides with $1^o$, and the two rays could interfere, if they had equal polarization. This requirement is fulfilled by means of the second polarizer $P_2$ of the prism unit (Fig. 1o.8), which provides a polarization under 45° with respect to the directions ' and $^o$. The optical axis of the polarizer $P_1$ is either parallel or rotated at 9o° to the axis of $P_2$, and its purpose is to provide equal intensity to the two interfering components. The same procedure applies to rays 1 and 3; i.e., 1' and $3^o$ can interfere, etc.

The distance d by which conjugate rays are sheared or separated in the test section is $d = \beta \cdot f_s$, with $f_s$ being the focal length of the "schlieren head". The choice of the Wollaston prism, which is commercially available, usually depends on the desired size of the separation d. In many practical applications, a reasonable size range of shear is 1 mm $\leq$ d $\leq$ 3 mm, and with focal lengths of the schlieren head ranging between 1 and 3 m, the prism should provide separation angles of a few minutes only. A number of different criteria determine the choice of d. This quantity should be small enough so that equation (1o.2) applies. On the other hand, if the density gradient to be resolved decreases, the shear d should increase. The edges of rigid bodies, which are normal to the direction of shear d, appear as a double image or gray zone of width d (or d $\cdot$ cos$\alpha$, where $\alpha$ is the angle between the direction of shear and the normal to the wall). The formation of this double image is due to the blocking of one of the two conjugate rays by the wall. The exact position of the wall edge is in the middle of the gray zone.

If the prism unit is displaced, along the optical axis, by a distance w from the focal point of the schlieren head (Fig. 1o.9), parallel, equidistant fringes will appear in the field of view. The fringe width S of this "finite fringe width" mode is inversely proportional to w:

$$S = \frac{\lambda \cdot f_s}{\beta \cdot w} = \frac{\lambda \cdot f_s^2}{d \cdot w}$$

(1o.6)

Rotation of the prism unit around the optical axis rotates the parallel fringe system.

As it was mentioned above, the prism unit can be implanted into an existing schlieren system in place of the knife edge.This allows for producing interferograms in a relatively large field of view (e.g., 0,5 m in diameter as in [1o.7]). If necessary, use can be made of the advantages of a double-pass system (Fig. 8.5). The optical set-up shown in Fig. 1o.8 requires a coherent light source, i.e., a laser whose beam is expanded and spatially filtered. Since, in most cases, the light from a laser has linear polarization, is it necessary either to adjust the direction of this polarization with the axes of the polarizers of the prism unit, or to pass the laser beam through a $\lambda$/4-phase plate to pro-

vide circular polarization to the beam. Many schlieren systems are operated with a white source. In converting such a system, a second Wollaston prism (with the same separation angle β) must be used on the side of the light source for improving the spatial coherence of the light (Fig. 1o.1o). The fringes of higher order now appear colored, and only the fringe of zeroth order is either white, if the axes of the two polarizers are parallel, or black, if the two polarizers are rotated at 9o°. In earlier descriptions of the interferometer, the role of this second Wollaston prism was interpreted as to give to the light beam the necessary shear.
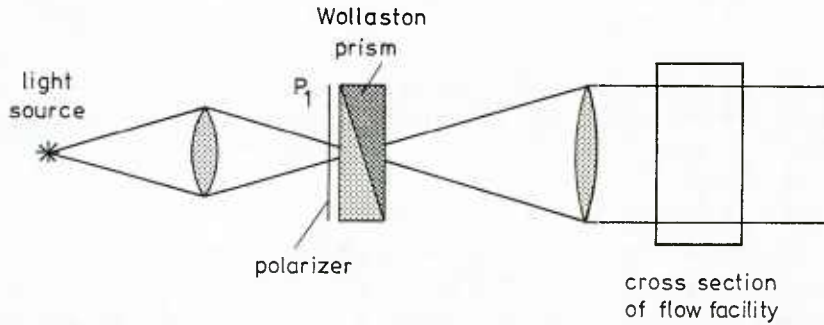


Fig. 1o.1o:  Operation of the schlieren interferometer with two Wollaston prisms; here: left (light-source) side of the system. The right side is as in Fig. 1o.8, but without the polarizer $P_1$.

A great number of compressible flow situations have been made visible with the Wollaston prism interferometer; see, e.g., [1o.11]. Of particular interest is the visualization or measurement of a shock wave. Since the density gradient through the shock is infinite, the linearized equation (1o.2) cannot describe the fringe pattern in this case. Instead, the complete equation (1o.1) must be considered. Only those pairs of conjugate rays, which have one ray passing behind, and the second ray passing in front of the shock wave can contribute to the formation of the respective pattern (Fig. 1o.11). The infinitesimally thin shock surface appears with finite thickness d or d · cosα, in analogy to the formation of a double image of the edges of rigid bodies (see above). In the finite fringe width mode, the shock cannot be visualized when the fringes are normal to the shock (one has then α = 9o°!). Also it is not appropriate to have the fringes parallel to the shock surface (Fig. 1o.1). If the fringes are oriented oblique to the shock, one measures a relative fringe shift, ΔS/S, which is given by

$$\left(\frac{\Delta S}{S}\right)_{shock} = \frac{K}{\lambda} \int_{z_1}^{z_2} \Delta\rho \; dz \quad , \tag{1o.7}$$

where K is the Gladstone-Dale constant, and Δρ the density jump across the shock. This relationship is identical with that derived for a reference beam interferometer (see chapter 11), however, the respective patterns are quite different, and the sensitivity of the two methods in resolving the density change through a shock wave, therefore, is not the same.
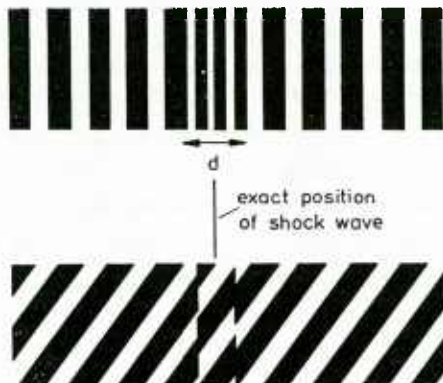


Fig. 1o.11:  Visualization of a (plane) shock front with the schlieren interferometer aligned at finite fringe width; above: fringes parallel to shock front; below: fringes oblique to shock front.

The Wollaston prism interferometer is particularly attractive for heat transfer studies, because the heat transfer coefficient, e.g. in natural convective flow, is proportional to the temperature gradient, and this quantity can be measured directly from the fringe shift, provided that the pressure can be taken as constant. The principles of this interferometer have been revised several times under the particular aspects of determining heat transfer rates, [1o.12 - 1o.15]. The numerous reported applications refer, e.g., to the measurement of convective heat transfer [1o.16 -1o.19], mass transfer in free jet flows [1o.2o, 1o.21], plasma flows [1o.22], or stratified flow in liquids [6.9, 1o.23].

## References

1o.1.   Malacara, D.; Cornejo, A.; Murty, M.V.R.K.: Bibliography of various optical testing methods. Appl. Opt. 14 (1975), 1o65-1o8o.

1o.2.   Merzkirch, W.: Generalized analysis of shearing interferometers as applied for gas dynamic studies. Appl. Opt. 13 (1974), 4o9-413.

1o.3.   Françon, M.: Interférometrie par double réfraction en lumière blanche. Rev. Opt. No. 31 (1952), 65-8o.

1o.4.   Chevalerias, R.; Latron, Y.; Véret, C.: Methods of flow interferometry applied to the visualization of flows in wind tunnels. J. Opt. Soc. Am. 47 (1957), 7o3-7o6.

1o.5.   Gontier, G.: Contribution à l'étude de l'interféromètre différentiel à biprisme de Wollaston. Publ. Sci. Tech. Minist. Air (France), No. 338, 1957.

1o.6.   Philbert, M.: Emploie de la strioscopie interférentielle en aérodynamique. Rech. Aérosp. No. 65 (1958), 19-27.

1o.7.   Merzkirch, W.: A simple schlieren interferometer system. AIAA J. 3 (1965), 1974-1976.

1o.8.   Oertel, H.: Messungen im Hyperschallstoßrohr. In: Kurzzeitphysik (eds. K. Vollrath, G. Thomer), pp. 758-848, Springer-Verlag, Berlin, 1967.

1o.9.   Smeets, G.: Aufnahmen mit dem Differential-Interferometer und ihre Auswertung. Proceed. 8th Int. Congr. High-Speed Photogr. pp. 374-378. 1968.

1o.1o.  Branston, D.W.; Mentel, J.: Beugungstheoretische Behandlung eines Differential-interferometers für ausgedehnte Phasenobjekte. Appl. Phys. 11 (1976), 241-246.

1o.11.  Page, R.H.; Sernas, V.: Apparent reverse transition in an expansion fan. AIAA J. 8 (197o), 189-19o.

1o.12.  Sernas, V.; Fletcher, L.S.: A schlieren interferometer method for heat transfer studies. J. Heat Transfer 92 (197o), 2o2-2o4.

1o.13.  Black, W.Z.; Carr, W.W.: Application of differential interferometer to the measurement of heat transfer coefficients. Rev. Sci. Instrum. 42 (1971), 337-34o.

1o.14.  Small, R.D.; Sernas, V.A.; Page, R.H.: Single beam schlieren interferometer using a Wollaston prism. Appl. Opt. 11 (1972), 858-862.

1o.15.  Flack, R.D.: Shearing interferometer inaccuracies due to a misaligned test section. Appl. Opt. 17 (1978), 2873-2875.

1o.16.  Aung, W.; Fletcher, L.S.; Sernas, V.: Developing laminar free convection between vertical flat plates with asymmetric heating. Int. J. Heat Mass Transfer 15 (1972), 2293-23o8.

1o.17.  Black, W.Z.; Norris, J.K.: Interferometric measurement of fully turbulent free convective heat transfer coefficients. Rev. Sci. Instrum. 45 (1974), 216-218.

1o.18.  Miller, R.M.; Gebhart, B.: An experimental study of the natural convection flow over a heated ridge in air. Int. J. Heat Mass Transfer 21 (1978), 1229-1239.

1o.19.  Bühler, K.; Oertel, H.: Thermal cellular convection in rotating rectangular boxes. J. Fluid Mech. 114 (1982),261-282.

1o.2o.  Stirnberg, D.; Ronkholz, E.; Merzkirch, W.: Der vertikale, laminare, isotherme Freistrahl mit Auftrieb und Diffusion. Z. Flugwiss. Weltraumforsch. 7 (1983), 31o-315.

1o.21.  Carlomagno, G.M.: Schlieren interferometry in the mass diffusion of a two-dimensional jet. Exp. Fluids 3 (1985), 137-141.

1o.22.  Kogelschatz, U.: Application of a simple differential interferometer to high current arc discharges. Appl. Opt. 13 (1974), 1749-1752.

1o.23.  Merzkirch, W.; Gärtner, U.; Wernekinck, U.: Invisible results of disturbed particles: Internal gravity waves in Fluids. Research 3/86 - Reports of the DFG (Deutsche Forschungsgemeinschaft), pp. 24-25, 1986.

## 11. REFERENCE-BEAM-INTERFEROMETER

In a reference beam interferometer, a light wave passing through the test flow interferes with a second, undisturbed wave, the reference wave. In analyzing the principle of this interferometer, one can make use of eq. (1o.1) if one assumes that the separation between two conjugate rays, d, is so large, that one of the two rays passes outside of the test section in a uniform environment with constant refractive index, $n_\infty$. All light rays in this beam (the reference beam) are propagating along optical paths of equal lengths, so that eq. (1o.1) now becomes

$$\Delta l(x,y) = \int_{z_1}^{z_2} [n(x,y,z) - n_\infty] \, dz \quad . \tag{11.1}$$

The equations for the bright and dark interference fringes, eqs. (1o.3), (1o.4), also hold in this case, and it becomes evident, that the measured signal, either in form of the fringe order or a fringe shift, is directly related to the absolute value of the refractive index n (or density $\rho$); see Table 6.3.

The two modes, "infinite fringe width" and "finite fringe width" are known also for the reference beam interferometer. The latter situation is realized by the superposition of an artificial density field described by n (x,y) = ax + by (a,b, = const.).

Among the many possible arrangements of a reference beam interferometer, only two will be discussed in this context. An important criterion for the application of such an interferometer to aerodynamic testing is, that the two beams, test beam and reference beam, be widely separated, so that the required form of the instrument is consistent with the geometry of the test facility.

### 11.1 MACH-ZEHNDER-INTERFEROMETER

This instrument, originally designed by Ernst Mach's son Ludwig and L. Zehnder, combines a wide separation of the test beam and the reference beam with a relatively large field of view (up to 25 cm in diameter). Theory and practice of the Mach-Zehnder-interferometer (MZI) have been reviewed several times; see [11.1 - 11.4]. In its basic arrangement (Fig. 11.1), light from a point source is made parallel with a lens or spherical (parabolic) mirror $L_1$. The essential components of the interferometer are the plane, fully reflecting mirrors $M_1$ and $M_2$, and the plane, semi-reflecting mirrors (beam splitters) $M_1'$ and $M_2'$. These four mirrors are arranged so that their centers form the four corners of either a rectangle (like in Fig. 11.1) or a parallelogram. In the latter case, a larger
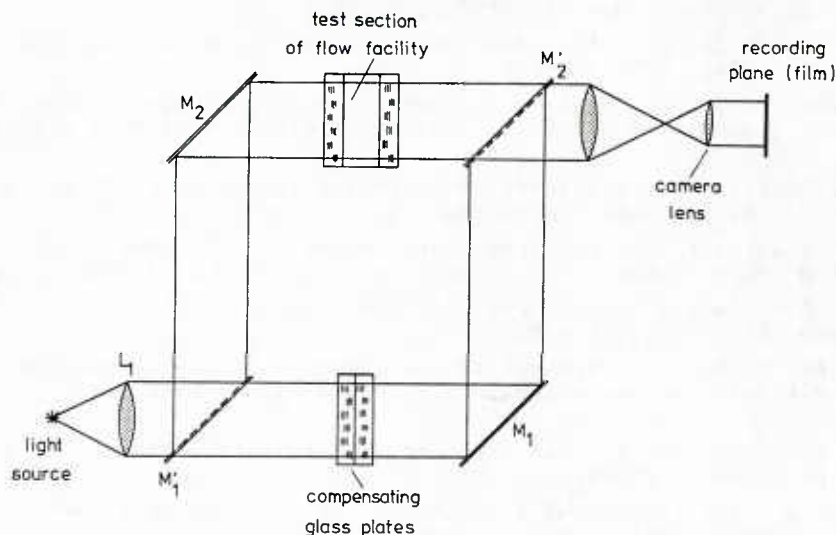


Fig. 11.1: Basic arrangement of a Mach-Zehnder interferometer. $M_1$, $M_2$ are fully reflecting mirrors, $M_1'$, $M_2'$ beam splitters.

percentage of the mirror surface is effectively used in the optical set-up; or: the parallelogram requires smaller mirrors for the same diameter of the field of view. The test sec-

tion of a flow facility is brought in the path of the test beam. If this test section is
bounded by viewing windows, it is advisable to insert two identical glass plates into the
path of the reference beam, in order to compensate for the large optical path length tra-
velled by the test beam in the glass. The beam splitter $M_2'$ plays the role for the "shearing
element" in Fig. 1o.1, providing, however, a large amount of shear or separation. A plane
in the test section is focused onto the recording plane (film) by means of the camera ob-
jective.

Each of the four mirrors is required to permit rotation around a horizontal and a
vertical axis for the basic adjustment of the interferometer, in which all mirrors are
parallel. This is the "infinite fringe width" alignment, i.e., in the absence of a test
flow and with all optical components being of perfect quality, the light rays arriving in
the recording plane are in phase. The "finite fringe width" mode can be realized by til-
ting one plate or mirror by a small angle γ. The resulting width of the parallel, undis-
turbed fringe system is

$$S = \frac{\lambda}{2\gamma}$$ (11.2)

Certain problems arise here in having both the fringe system and the test object in fo-
cus. Kinder [11.2] has developed an arrangement that fulfills this requirement and can be
adjusted by controlling only one mirror.

ded for constructing a MZI. Tolerances of surface flatness, surface parallelism, trans-
lational and rotational displacement, control of tilt must be in the order of one tenth
of a wavelength. The same applies to the optical homogeneity of the beam splitters and
the windowsof the test section. The instrument is, therefore, expensive, the costs growing
rapidly with the desired diameter of the field of view. The mirrors and plates are moun-
ted on a U-shaped steel frame. The fourth side of the frame is open for inserting the
test section of a flow facility. The required mechanical stability of the frame limits the
size of the U and thereby the possible separation of test and reference beam. It will be
shown below that many of these requirements of mechanical precision do not exist for a
holographic interferometer, which has replaced the MZI in many fields of application.

Modifications of the MZI have been described, which try to combine a large diame-
ter of the test beam, i.e. a large field of view, with a reduction of the reference
beam's dimensions, in order to minimize the mechanical complexity of the instrument. The-
se modifications require the use of a coherent laser source. In the arrangement proposed
by Grigull and Rottenkolber [11.5], the reference beam is simply the thin, collimated la-
ser beam, which is only expanded in the immediate vicinity of the second beam splitter
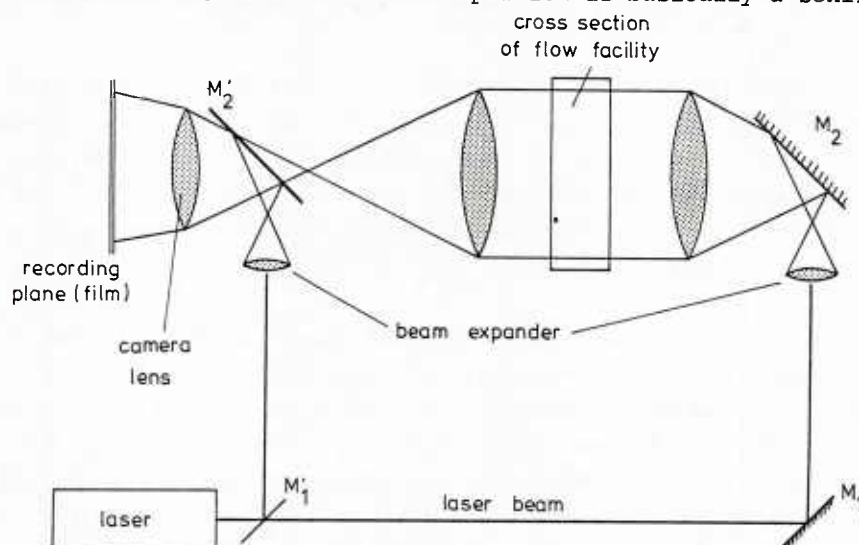$M_2'$ (Fig. 11.2). Howes [11.6] describes a set-up which is basically a schlieren system of



Fig. 11.2: Mach-Zehnder interferometer with laser light source. The major parts of the
reference beam and the test beam are fed as thin laser beams (from [11.5]).

large aperture followed by a relatively small MZI-like arrangement. The reference beam is fed through a spatial filter, where all the phase information from the schlieren field is removed.

It is difficult to oversee the large number of reported applications of Mach-Zehnder interferometry to the study of compressible flows, and a list of references would in any case remain incomplete. Two interferograms are included here as typical examples for the visualization of the flow pattern in a supersonic cascade wind tunnel (Fig. 11.3), and the diffraction and reflection of an air shock wave in a shock tube (Fig. 11.4). In
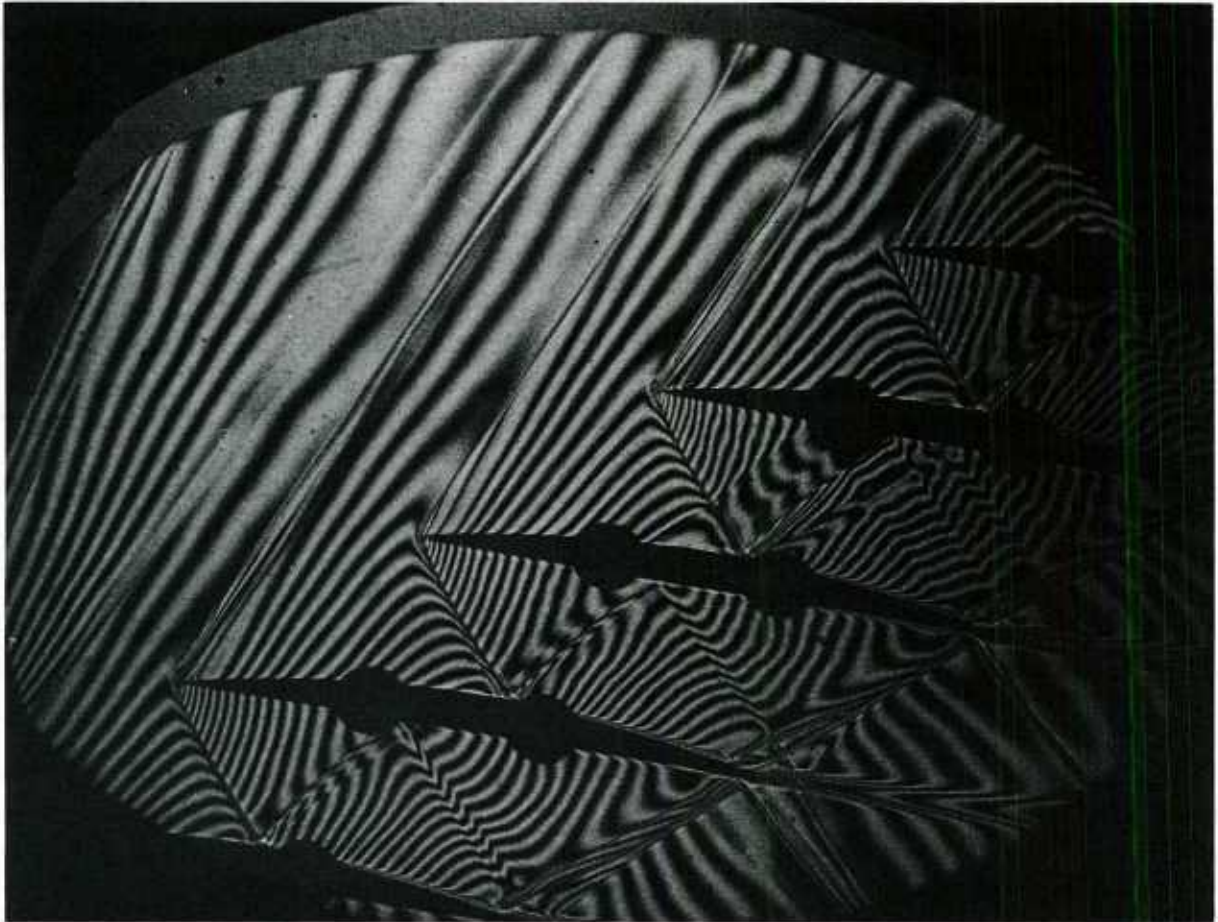


Fig. 11.3: Mach-Zehnder interferogram of the supersonic flow in a cascade wind tunnel. Mach number of incident flow is $M_\infty = 1.24$ (DFVLR-Institut for Antriebstechnik, Köln, F.R. Germany).

these applications there is a particular interest in determining the density jump across a shock front.These quantity is directly available from the fringe shift measured in a finite fringe width interferogram and the application of eq. (1o.7), which also holds for reference beam interferometry. The two sample figures make evident, that the fringe pattern across a shock front is different here from the pattern obtained with a schlieren interferometer (see Fig. 1o.12).

Analyzing a turbulent flow with density fluctuations by means of interferometry is difficult, if not impossible, because the interference fringes are blurred and lose their identity. Flow instabilities can be observed and evaluated up to a certain degree, as verified by Anderson et al. [11.7]. An extended literature is available on the use of the MZI for convective heat transfer studies and the investigation of flames; for an overview see [6.1] and [6.2]. A few representative applications are included in the list of references [11.8 - 11.12]. Error sources arising from the special situation of heat transfer measurements have been particularly investigated [11.3, 11.14]. A modification of the MZI has been used for measurements in a spacelab environment [11.15].
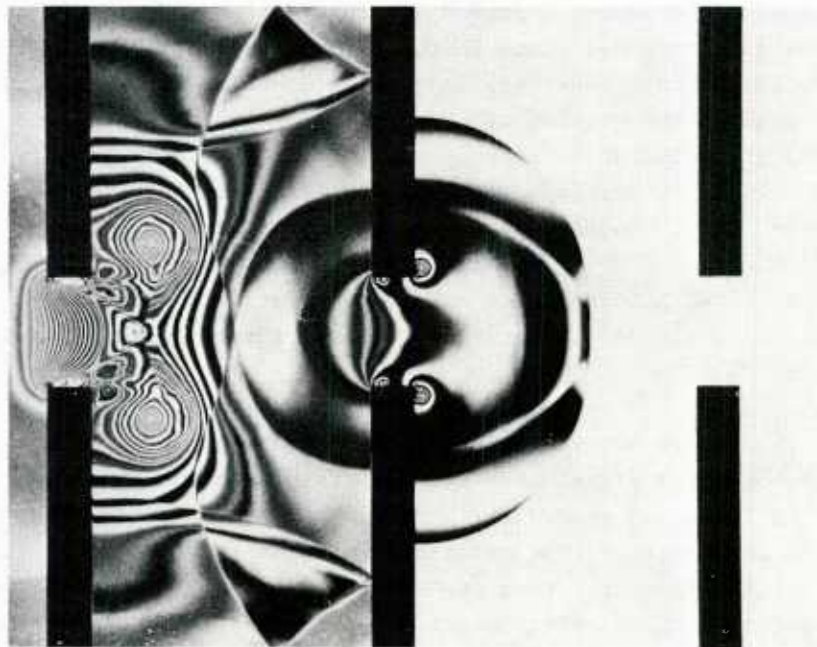
Fig. 11.4: Mach-Zehnder interferogram of the diffraction of a shock wave. Shock wave propagation is from left to right. Compressible vortices separate from the edges of the vertical walls (H. Reichenbach, Ernst-Mach-Institut, Freiburg, F.R. Germany)

## 11.2 HOLOGRAPHIC INTERFEROMETER

Holography is a means for freezing all the information contained in a light wave, and for reconstructing this wave at any desired, later instant of time. In contrast to normal photography, which gives information only on the amplitude pattern of a wave, holography also provides the complete phase information of such a light wave. It was, therefore, a consequent step to make use of this principle in the field of interferometry where two (or more) light waves are made to interfere with oneanother. The result is known as holographic interferometry [11.16], and, as noted already in the previous paragraph, this relatively new technique is taking over the role that the "classical" Mach-Zehnder interferometry has played over several decades of testing flows with varying fluid density.

A holographic interferometer is operated with a laser light source whose beam is separated by a beam splitter into two beams. The principal set-up (Fig. 11.5) shows that
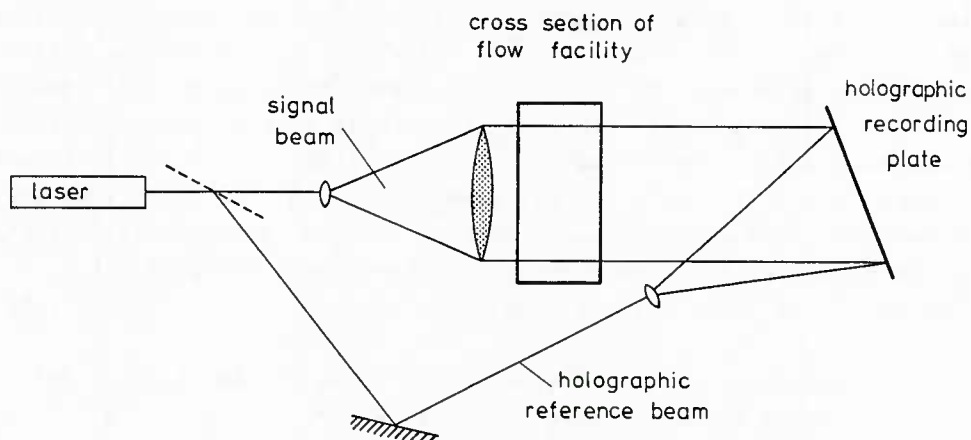


Fig. 11.5: Principal arrangement for taking a holographic interferogram with a double exposure.

one of the two beams, after beeing expanded and then collimated, passes through the test flow and arrives at a holographic plate in the recording plane. This beam will be called the signal beam or holographic test beam (not to be confused with the test beam of a MZI!). The second beam is fed outside of the test object where it remains undisturbed. This beam is called the holographic reference beam. It is also expanded and arrives at the recording plane where it overlaps with the signal beam. The result is a fine-scale interference pattern, the "hologram", which allows for reconstructing the light wave that has passed through the test flow, i.e., the signal beam. The reconstruction consists of illuminating the developed hologram with only the holographic reference beam, i.e., the hologram, after being developed, is returned in its original position, and the signal beam is blocked off.

So far, the system does not yet allow for seeing a flow, because the reconstructed wave as well as the original signal wave are not visible to the naked eye. Interferometry is achieved with the following procedure: A first hologram is produced as described above with no flow in the test section. The developed hologram is replaced in its original position, the compressible flow is turned on, and the hologram illuminated with both the signal beam and the holographic reference beam. Due to the existence of the latter beam, the signal wave or beam of the first exposure is reconstructed. This wave can interfere with the now existing signal wave that carries information on the existing refractive index field. It is obvious that the first exposure is equivalent to the reference beam of a MZI, while the signal beam with the flow being turned on is equivalent to the test beam of a MZI. The result is a reference beam pattern in the infinite fringe mode, which becomes visible, if one views from behind through the holographic plate.

When such a system is operated as it has been described, i.e. with the first hologram developed and replaced in its original position, it is possible to observe the interference pattern during the experiment. It is said that the interferometer is operated in "real time". A time-dependent flow could then be recorded with a movie camera, as it can be done with a MZI. The technical problem here is that the developed hologram has to be returned exactly in its original position, i.e. with a precision of a small fraction of a wave length. Since this is difficult to realize, holographic plate holders have been developed in which the plate can be developed in place, i.e. without removing it from the holder. An alternative is to record two exposures in the system, one without flow and the second with flow, on the same holographic plate ("holographic double exposure"). When the plate is developed, the interference pattern becomes visible. However, this operation does not allow for a direct or "real time" observation of the flow.

From this description of the method, the differences between holographic and Mach-Zehnder interferometry become obvious: In the MZI, the test beam and the reference beam exist simultaneously, but they are separated in space. In a holographic interferometer, the test beam (or wave) and the reference beam (wave) exist at different instants of time, but they coincide spatially. This spatial coincidence of the signal beams in the two holographic exposures (without and with flow) results in an important technical advantage, which makes the holographic interferometer superior to the MZI: The optical paths of the two signal beams differ only due to the difference in fluid density between the flow and the no-flow situation. Optical disturbances or impurities in the glass of test section windows or in any other optical component of the system are cancelled out, and a holographic interferogram can be taken through glass windows of relatively low quality.

Holographic interferometry was first applied for flow visualization and the measurement of density fields by Heflinger et al. [11.17] and Tanner [11.18]. When the many advantages over Mach-Zehnder interferometry became evident, the new method was soon picked up by a number of laboratories [11.19 - 11.21]. The further development is well reflected in the book of Vest [11.16]. Today, holographic interferometers are commercially available,

but an engineer who is not totally unfamiliar with the practice of optics can well build his own system. A practical realization of such a system is shown in Fig. 11.6. While many systems are built flat on a socalled holographic table (a heavy, plane granite plate protecting the system against mechanical vibrations), this system is mounted vertical on an optical bench. The beam expander included in the set-up of Fig. 11.6 provides an expansion of the thin laser beam. Such a unit consist of an objective of short focal length (microscope objective) and a small pinhole placed in the focal point of the objective (Fig. 11.7). The diameter of this pinhole is of the size of the zeroth diffraction order of the light in the focal point, and it serves for cleaning the expanding beam from diffractive noise.
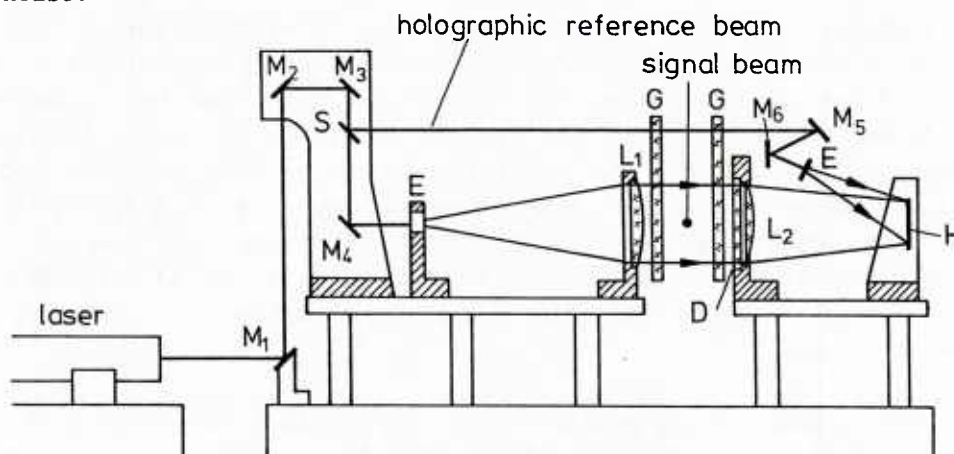


Fig. 11.6: Set-up of a holographic interferometer; $M_i$: mirrors; S: beam splitter; E: beam expander; $L_i$: lenses; G: glass windows of test section; D: diffuser glass; H: holographic plate (after [11.22]).
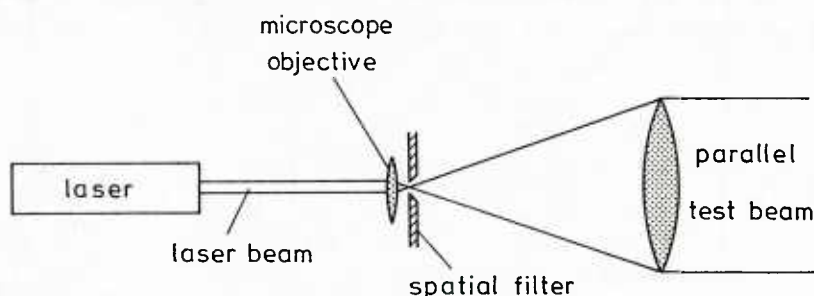


Fig. 11.7: Optical element for expanding and spatial-filtering of a laser beam.

The signal beam in the arrangement of Fig. 11.6 is passed through two test section windows. The mentioned compensation of window imperfections in the holographic double exposure is achieved only when the state of the glass does not change between the two exposures. A deviation from this situation has been described by Koster [11.14]. He shows that, in performing heat transfer measurements, a temperature field may build up in the test section windows, thereby causing a time change in the refractive index distribution in the windows. A similar problem may arise when an optical method is applied to a cryogenic wind tunnel. Snow et al. [11.23] report on the observation of a tremendous loss of signal quality when optical diagnostic techniques are used with such a facility. The explanation are refractive index variations induced by strong temperature gradients in the environment of the (cool) test section windows. This refractive index disturbance outside of the test section would, of course, not be compensated for in a holographic double exposure.

The arrangement shown in Fig. 11.6 includes a diffuser plate or ground glass in the path of the signal beam. With this element one introduces a certain kind of spatial (three-dimensional) information in the interferogram. Since the diffuser scatters the light in various directions, light beams are traversing the test field in a variety of

directions, and the reconstructed scene may be examined under different viewing angles.
In order to observe interference fringes it is necessary that the optical path lengths of
all rays passing with different direction through the same image point are independent of
the viewing angle. The respective formulation of this condition (see, e.g., [11.16],[1.1])
defines a surface in the test field onto which the recording plane (camera) has to be fo-
cused for obtaining fringes. If these requirements are fulfilled, interferograms can be
taken in various directions from the same holographic double exposure, the possible vie-
wing directions covering an angle in the order of $-2o° \leq \alpha \leq + 2o°$. Problems of fringe
clarity arising from this arrangement have been discussed by Tanner [11.24].

Several technical solutions exist for producing a holographic interferogram in the
finite fringe width mode. When the system is operated in real time, fringes of finite
fringe width will appear with an undisturbed test field, if the developed first hologra-
phic exposure is not replaced precisely in its original position. A more accurate control
of fringe spacing and direction of the undisturbed fringe pattern is possible with the
dual-plate holder: Reference (first) and test (second) hologram are taken on two separate
plates, which, after being developed, can be rotated and sheared with respect to each
other in the holder during the simultaneous reconstruction [11.25, 11.26]. The same result
is obtained by a small change in the adjustment of the holographic reference  beam between
the two exposures [11.27].

Several authors describe the realization of the finite fringe width mode by utili-
zing in the system two separate holographic reference beams [11.28 - 11.31], see Fig.
11.8. One reference beam serves for taking the reference (first) exposure, the second
beam is used for the test exposure. In the reconstruction process, the hologram is illu-
minated by the two holographic reference beams simultaneously, and the interferogram ap-
pears in the desired fringe mode. The appropriate fringe pattern is selected by control-
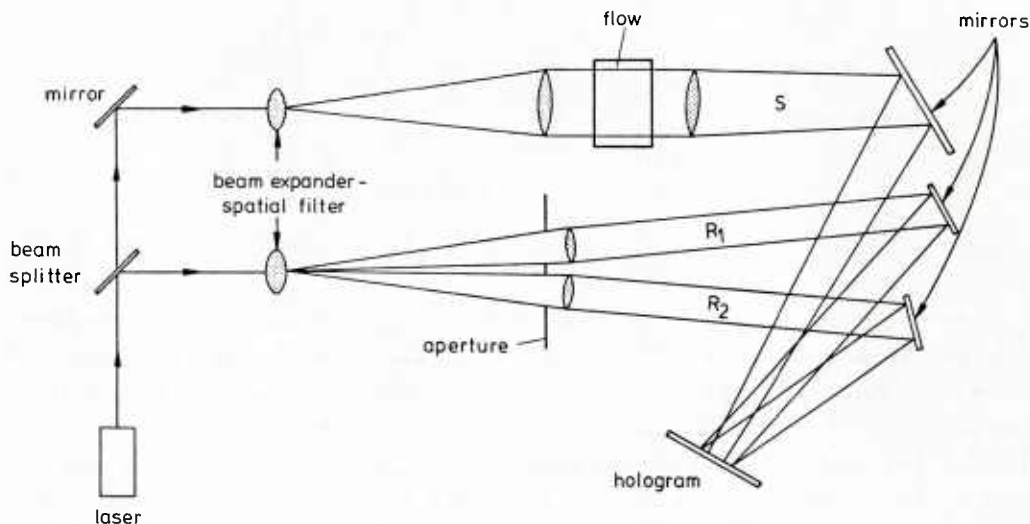ling the angle between the two beams.



Fig. 11.8:  Holographic interferometer with two reference beams (after [11.3o]).

Since about 197o, the number of applications of holographic interferometry has ex-
ploded. Many laboratories have taken over the new technique for experiments with compres-
sible flows in wind tunnels, ballistic ranges, shock tubes (Fig. 11.9) or for heat trans-
fer studies, and laboratory reports describing details of the new technique have been pro-
duced; see, e.g., [11.32 - 11.34]. Only a few representative references, which stand for
many others, can be given [11.35 - 11.41]. The resolution of three-dimensional density
fields requires taking more than only one holographic interferogram, because the recon-
struction of such a field needs a total viewing angle greater than the mentioned range

of $\bar{+}$ 2o° (see chapter 12).



Fig. 11.9: Holographic interferogram of a focusing shock wave taken in a shock tube. The focusing shock wave is seen in the center in form of a small triangle. Initial shock Mach number $M_s$ = 1.26 in nitrogen at a pressure of 1 bar (H. Grönig, RWTH Aachen, F.R. Germany).

REFERENCES

11.1.  Schardin, H.: Theorie und Anwendungen des Mach-Zehnder Interferenz-Refraktometers. Z. Instrumentenkunde 53 (1933), 396-4o3.

11.2.  Kinder, W.: Theorie des Mach-Zehnder-Interferometers und Beschreibung eines Gerätes mit Einspiegeleinstellung. Optik 1 (1946), 413-448.

11.3.  Winckler, J.: The Mach interferometer applied to studying an axially symmetric supersonic air jet. Rev. Sci. Instrum. 19 (1948), 3o7-322.

11.4.  Ladenburg, R.; Bershader, D.: Interferometry. In: Physical measurements in Gas Dynamics and Combustion (ed. R.W. Ladenburg), pp. 47-78, Princeton University Press, 1954.

11.5.  Grigull, U.; Rottenkolber, H.: Two-beam interferometer using a laser. J.Opt. Soc. Am. 57 (1967), 149-155.

11.6.  Howes, W.L.: Large-aperture interferometer with local reference beam. Appl. Opt. 23 (1984), 1467-1473.

11.7.  Anderson, J.S.; Jungowski, W.M.; Hiller, W.J.; Meier, G.E.A.: Flow oscillations in a duct with a rectangular cross-section. J. Fluid Mech. 79 (1977), 769-784.

11.8.  Van Buren, P.D.; Viskanta, R.: Interferometric measurement of heat transfer during melting from a vertical surface. Int. J. Heat Mass Transfer 23 (198o), 568-571.

11.9.  Yousef, W.W.; Tarasuk, J.D.: An interferometric study of combined free and forced convection in a horizontal isothermal tube. J. Heat Transfer 1o3 (1981), 249-256.

11.1o. Shlien, D.J.; Boxman, R.L.: Laminar starting plume temperature field measurement. Int. J. Heat Mass Transfer 24 (1981), 919-931.

11.11. Aung, W.: An interferometric investigation of separated forced convection in laminar flow past cavities. J. Heat Transfer 1o5 (1983), 5o5-512.

11.12. Liu, K.V.; Lloyd, J.R.; Yang, K.T.: An investigation of a laminar diffusion flame adjacent to a vertical flat plate burner. Int. J. Heat Mass Transfer 24 (1981), 1959-197o.

11.13. Flack, R.D.: Mach-Zehnder interferometer errors resulting from test section misalignment. Appl. Opt. 17 (1978), 985-987.

11.14. Koster, J.N.: Interferometric investigation of convection in plexiglas boxes. Exp. Fluids 1 (1983), 121-128.

82

11.15. Owen, R.B.: Interferometry and holography in a low-gravity environment. Appl. Opt. 21 (1982), 1349-1355.

11.16. Vest, C.M.: Holographic Interferometry. Wiley, New York, 1979.

11.17. Heflinger, L.O.; Wuerker, R.F.; Brooks, R.E.: Holographic interferometry. J. Appl. Phys. 37 (1966), 642-649.

11.18. Tanner, L.H.: Some applications of holography in fluid mechanics. J. Sci. Instrum. 43 (1966), 81-83.

11.19. Philbert, M.; Surget, J.: Application de l'interférométrie holographique en soufflerie. Rech. Aérosp. no. 122 (1968), 55-6o.

11.2o. Smigielski, P.; Royer, H.: Applications de l'holographie à l'aérodynamique. L'Onde Electrique 48 (1968), 223-225.

11.21. Beamish, J.K.; Gibson, D.M.; Sumner, R.H.; Zivi, S.M.; Humberstone, G.H.: Wind-tunnel diagnostics by holographic interferometry. AIAA J. 7 (1969), 2o41-2o43.

11.22. Délery, J.; Surget, J.; Lacharme, J.P.: Interférométrie holographique quantitative en écoulement transsonique bidimensionel. Rech. Aérosp. 1977-2 (1977), 89-1o1.

11.23. Snow, W.L.; Burner, A.W.; Goad, W.K.: Improvement in the quality of flow visualization in the Langley o.3-meter transonic cryogenic tunnel. NASA TM 8773o, 1986.

11.24. Tanner, L.H.: A study of fringe clarity in laser interferometry and holography. J. Phys. E: Sci. Instrum. 1 (1968), 517-522.

11.25. Hannah, B.W.; Havener, A.G.: Applications of automated holographic interferometry. ICIASF '75 Record, IEEE Publication CHO 993-6 AES (1975), 237-246.

11.26. Dunagen, S.E.; Brown, J.L.; Miles, J.B.: Holographic interferometry study of an axisymmetric shock-wave/boundary-layer strong interaction flow. AIAA J. 25 (1987), 294-299.

11.27. Burner, A.W.; Goad, W.K.: Phase control during reconstruction of holographically recorded flow fields using real-time holographic interferometry. NASA TM 81953,1981.

11.28. Surget, J.: Schéma d'holographie à deux sources de référence. Nouv. Rev. Opt. 5 (1974), 2o1-217.

11.29. Dändliker, R.; Marom, E.; Mottier, F.M.: Two reference-beam holographic interferometry. J. Opt. Soc. Am. 66 (1976), 23-3o.

11.3o. Trolinger, J.D.: Application of generalized phase control during reconstruction of flow visualization holography. Appl. Opt. 18 (1979), 766-774.

11.31. Farrell, P.V.; Springer, G.S.; Vest, C.M.: Heterodyne holographic interferometry: concentration and temperature measurements in gas mixtures. Appl. Opt. 21 (1982), 1624-1627.

11.32. Havener, A.G.: A users guide on pulse laser holography for wind tunnel testing. ARL TR 75-o213, 1975.

11.33. Faw, R.E.; Dullforce, T.A.: Holographic interferometry-Principles and procedures. Report CLM-RR/S2/19, Culham Lab., Abingdon, England, 1977.

11.34. Walklate, P.J.: A holographic technique for the study of heat transfer from a rib-roughened surface. Report AERE-R 1o172, A.E.R.E. Harwell, England 1981.

11.35. Witte, A.B.; Fox, J.; Rungaldier, H.: Localized measurements of wake density fluctuations using pulsed laser holographic interferometry. AIAA J. 1o (1972), 481-487.

11.36. Radley, R.J.; Havener, A.G.: Application of dual hologram interferometry to wind-tunnel testing. AIAA J. 11 (1973), 1332-1333.

11.37. Ozkul, A.: Investigation of acoustic radiation from supersonic jets by double-pulse holographic interferometry. AIAA J. 17 (1979), 1o68-1o75.

11.38. Decker, A.J.: Holographic flow visualization of time varying shock waves. Appl. Opt. 2o (1981), 312o-3127.

11.39. Bryanston-Cross, P.J.; Lang, T.; Oldfield, M.L.G.; Norton, R.J.G.: Interferometric measurements in a turbine cascade using image-plane holography. J. Eng. Power 1o3 (1981), 124-13o.

11.4o. Lee, G.; Buell, D.A.; Licursi, J.P.; Craig, J.E.: Laser holographic interferometry for an unsteady airfoil undergoing dynamic stall. AIAA J. 22 (1984), 5o4-511.

11.41. Bryanston-Cross, P.J.; Dawes, W.N.: Comparison of inviscid and viscous transonic flow. AIAA J. 23 (1985), 834-839.

## 12. AXISYMMETRIC AND 3-D FLOW FIELDS

Due to the integration along the light path, the signal obtained by the optical visualization methods from a three-dimensional flow is plane or two-dimensional. This is obvious, e.g. from the equations (1o.2) or (11.1) where the signal $\Delta l$ is given as a function of x,y, whereas the refractive index n depends on the three Carthesian coordinates x,y,z.

In order to resolve the dependence of n on z, it is necessary to direct the optical light beam in different directions through the flow ("tomography"). As it will be discussed below, the number of necessary viewing directions is reduced if the flow has some kind of symmetry. In the case of rotational symmetry, one projection or viewing direction is sufficient for determining n(x,r), where it is assumed that the x-direction is the axis of rotational symmetry.

## 12.1 AXISYMMETRIC FLOW

The light propagates again in z-direction, and the refractive index depends on the two coordinates x and $r=(y^2+z^2)^{1/2}$, see Fig. 12.1. The equations relating the optical signal with the refractive index distribution must be transformed accordingly. These equations have on their left side a signal or data function, D (x,y), with x,y being the coordinates in the recording plane. D(x,y) stands for either the fringe order or the relative fringe shift in interferograms, or the light deflection angle $\varepsilon$(x,y) as measured with speckle photography or moiré. The right side is a refractive index function R(x,y,z), whose form follows from the respective equations in chapters 8, 1o and 11. After transfor-
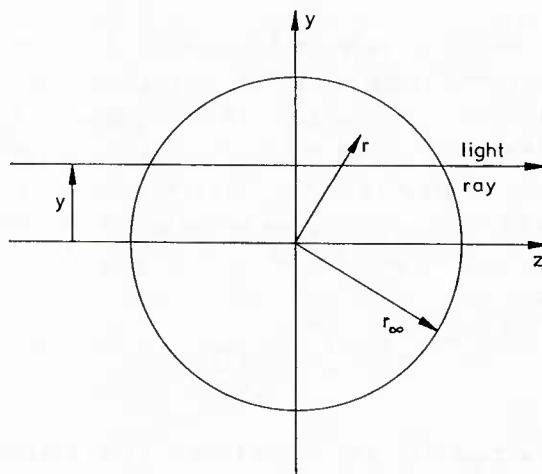


Fig. 12.1: Cross-section of axisymmetric flow field with outer radius $r_\infty$. The light propagates in the z-direction.

mation, the fundamental equation for the axisymmtric case is

$$D(x,y) = \int_{r=y}^{r_\infty} R(x,r) \ (r^2-y^2)^{-\frac{1}{2}} \cdot d(r^2).$$  (12.1)

The axisymmetric flow field is bounded by the outer radius $r_\infty$. The forms of D and R for the three quantitative methods, schlieren interferometry, reference beam interferometry, and speckle photography, are given in Table 12.1.

Eq. (12.1) is an integral equation of the classical Abel type and it can be directly inverted, yielding

$$R(x,r) = -\frac{1}{\pi} \frac{d}{d(r^2)} \int_{r}^{r_\infty} D(x,y) \cdot (y^2-r^2)^{-\frac{1}{2}} d(y^2).$$  (12.2)

Usually, D(x,y) is not available as a continuous function but in form of a set of discrete data points. Solignac [12.1] and South [12.2] have described schemes for approximating the set of discrete data by appropriate analytic expressions. Computer programs and algorithms for solving the Avel inversion (12.2) have been presented in various laboratory reports, e.g. [12.3, 12.4].

## Table 12.1

Data function D and refractive index function R in the evaluation of axissymmetric refractive index fields.

| | reference beam interferometer | shearing interferometer | speckle photography | |
|---|---|---|---|---|
| infinite fringe width alignment | $D = \frac{\Delta l(x,y)}{\lambda}$ | $D = \frac{1}{y \cdot d} \cdot \frac{\Delta l(x,y)}{\lambda}$ | $D_x = \varepsilon_x$ | |
| | $R = \frac{1}{\lambda}\{n(x,r) - n_\infty\}$ | $R = \frac{1}{\lambda} \cdot \frac{\partial n(x,r)}{\partial(r^2)}$ | $D_y = \varepsilon_y$ | |
| finite fringe width alignment | $D = \frac{\Delta S(x,y)}{S}$ | $D = \frac{1}{y \cdot d} \cdot \frac{\Delta S(x,y)}{S}$ | $R_x = \frac{\partial n}{\partial x}$ | |
| | $R = \frac{1}{\lambda}\{n(x,r) - n_\infty\}$ | $R = \frac{1}{\lambda} \cdot \frac{\partial n(x,r)}{\partial(r^2)}$ | $R_y = \frac{\partial n}{\partial y}$ | |

A disadvantage of the Abel inversion is the needed differentiation, $d/d(r^2)$, of the experimental data $D(x,y)$, as shown in eq. (12.2). Such a differentiation is associated with the generation of errors. The disadvantage is avoided with optical methods depending on the measurement of the refractive index gradient, like schlieren method, deflection mapping by speckle photography or moiré, and schlieren interferometry. The two differentiations $d/d(r^2)$ on both sides of the respective equations are then eliminated by a simple integration, and the result, written for the case of deflectometry, where the deflection angel $\varepsilon_y$ is measured, becomes

$$n(x,r) - n(x,r_\infty) = -\frac{1}{\pi} \cdot \int_r^{r_\infty} \frac{\varepsilon_y(x,y)}{y} \cdot \frac{d(y^2)}{\sqrt{y^2 - r^2}} \ . \tag{12.3}$$

This result is surprising, because eq. (12.3) states that the methods, whose signal delends on the refractive index gradient, deliver the absolute value of the refractive index or density when they are applied to an axisymmetric field [1o.2o, 12.3, 12.5 - 12.7].

Eq. (12.1) and Fig. 12.1 show that all refractive index values with $r > y$ contribute to the variation in optical phase of a ray propagating at position y. This fact has been used by Schardin [8.3] for developing a scheme for the approximation and evaluation of the integral in eq. (12.1). At the same time, this scheme clearly visualizes that one projection is sufficient for measuring an axisymmetric refractive index field. The principle of the scheme is explained with Fig. 12.2. A circular cross-section of the flow is subdivided into N annular zones of width h. The refractive index function R is assumed to be constant within each zone. The integral is solved in a step-wise procedure starting with a ray that passes through the most outer zone (in Fig. 12.2 ray no. 1). The optical signal generated by this ray is sufficient for determining the respective value of $R_N$, N being the number of the most outer zone. With $R_N$ being determined, ray no. 2 in the next step also passes through only one zone of unknown value of R, namely $R_{N-1}$. An equation can be written relating the optical signal of ray no. 2 to the known contribution of $R_N$ and the contribution of $R_{N-1}$, which can now be determined. The procedure continues until one arrivesat the ray through the center of the circular field. Computer algorithms for this procedure have been described in laboratory reports [12.4, 12.8].

Of particular interest for supersonic aerodynamic studies is the treatment of a discontinuity in the refractive index distribution, as caused, e.g., by the shock around a cone without angle of attack. The data function is then split into two portions, one

taking account of the continuous density field and the second of the density discontinuity. The problem has been discussed, e.g., by Bennett et al. [12.9], Solignac [12.1o], and Maruyama et al. [12.11].
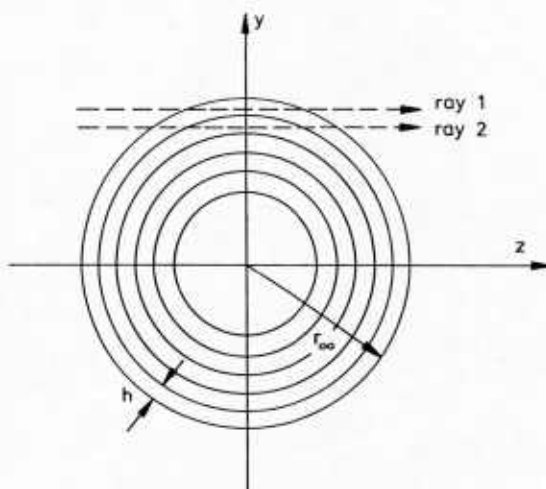


Fig. 12.2: Subdivision of the axisymmetric flow field in annular zones of width h.


## 12.2. TOMOGRAPHY

The problem of reconstructing a three-dimensional object field from a set of two-dimensional (plane) projections arises in various areas of experimentation, besides flow visualization also in X-ray diagnostics, electron microscopy or radio astronomy. A mathematical formulation of the problem was given already by Radon in 1917. A great amount of special literature of this aspect is available, as well as reviews and discussions of the general aspects [12.12 - 12.14]. As in the axisymmetric case, there are , in principle, two ways of reconstructing the three-dimensional density field without symmetry: inversion schemes and discretization of the problem.

Projections are taken in a number of different directions $\zeta_i$, where $\zeta_i$ forms the angle $\alpha_i$ with the z-axis (Fig. 12.3). The projection generates the plane data field $D(x,y,\alpha_i)$. The equation to be inverted is

$$D(x,y,\alpha_i) = \int_{\zeta_{i1}}^{\zeta_{i2}} R(x,y,z)\,d\zeta_i \quad , \qquad (12.4)$$

where $\zeta_{i1}$ and $\zeta_{i2}$ are the entrance and exit coordinates of the light rays at the test field in the i-th projection. The refractive index function $R(x,y,z)$ must be presented by series of generating functions which allow for inverting this integral equation. Inversion schemes with appropriate functional series have been described by Matulka and Collins [12.15] and Sweeney and Vest [12.16]. Applications of these schemes include the supersonic flow over circular cones at angle of attack [12.17], transonic corner flow [12.18], mixing in a buoyant plume [12.19], or the transonic flow near the tips of a rotor blade [12.2o, 12.21]. The referred applications are all based on holographic interferometry. It has been mentioned in chapter 11 that the spatial information obtainable from one holographic interferogram is not sufficient for the reconstruction of an arbitrary 3-D density field. The analysis shows that it is necessary to use projections covering an angular range of $-9o° \leq \alpha_i \leq + 9o°$.

Inversion schemes which are based on Fourier transforms have been described by Rowley [12.22] and by Junginger and van Haeringen [12.23]. Zien et al. [12.24] applied this method to the supersonic flow over a cone at angle of attack. They also discuss the pro-

86

blem that arises when part of the test beam is blocked off by the model in the wind tunnel, i.e. when the projections are incomplete;see also [12.25].
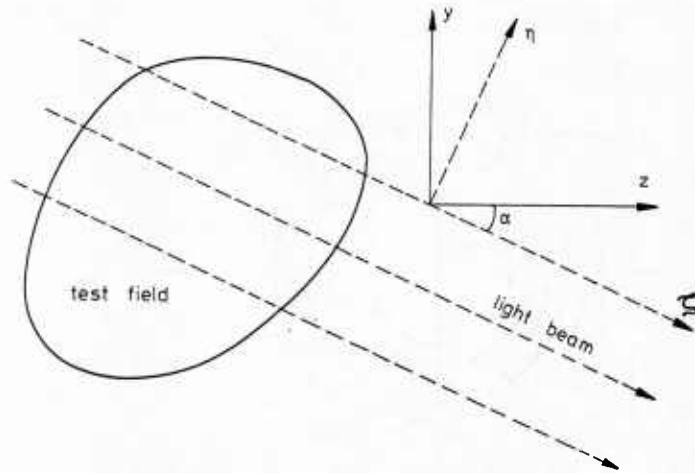


Fig. 12.3:  Projection of light in $\zeta$-direction through a three-dimensional flow field.

Only a few applications of discretisized methods for reconstructing a three-dimensional flow field have been reported [12.26 - 12.28]. The situation is represented in Fig. 12.4, and this figure may also serve for providing an easy description of the general problems of reconstructing a 3-D field from plane projections. The figure shows a cross-sec-
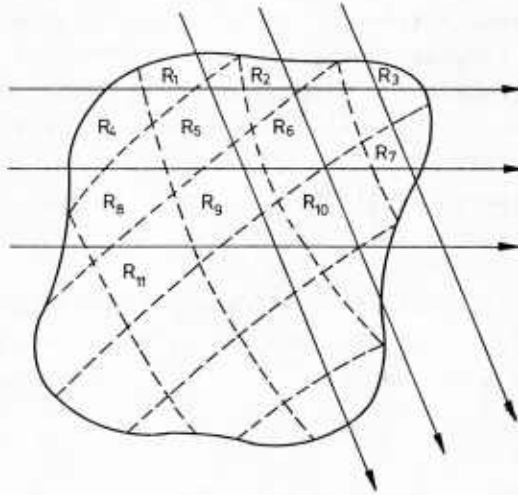


Fig. 12.4:  Subdivision of a cross-section of the three-dimensional flow field into elements, in each of which the refractive index function is assigned a constant value $R_i$. Different projections of the light through the field.

tion of the flow in the y-z plane (see also Fig. 12.3), which is subdivided into N segments, in each of which the refractive index function R assumes a constant value $R_j$, with $1 \leq j \leq N$. The problem is to determine N unknown quantities in this particular cross-section, $R_1 \ldots R_N$, and this requires defining and solving a set of N independent equations. A light ray in the i-th direction carries information on the $R_j$-values of m segments, with $m < N$. This information is expressed by a respective value $D_i$ of the data function $D(x,y,\alpha_i)$. The equation relating $D_i$ to the m values $R_j$,

$$D_i = \sum R_j s_{ji}$$

is just one equation of the mentioned set. $s_{ji}$ is the length covered by the light ray within the j-th segment in the i-th direction, and the equation is seen to be linear. The light beam in the i-th direction cannot provide enough equations, and it becomes necessary

to direct the light in different directions through the refractive index field, until a sufficient number (N) of independent, linear equations has been generated.

The number of necessary viewing directions or projections increases, the finer the subdivision of the respective cross-section, i.e. the higher the number N. The question then is, whether the visual pattern of each projection is sufficiently different from its neighbouring projection, or: whether the signal $D_i$ is sufficiently sensitive to changesof the directional angle $\alpha_i$ (Fig. 12.3). Fig. 12.4 also gives an indication of how the situation is simplified by a certain degree of symmetry of the flow: Such a symmetry simply reduces the number of unknowns to be determined. This discussion of the problem with considering only one cross-section requires that the light rays are not bent out of the y-z plane, an assumption which has been made already in chapter 6.

## REFERENCES

12.1. Solignac, J.-L.: Méthode de dépouillement des interférogrammes en écoulement de révolution. Rech. Aérosp. no. 1o4 (1965), 12-13.

12.2. South, R.: An extension to existing methods of determining refractive indices from axisymmetric interferograms. AIAA J. 8 (197o), 2o57-2o59.

12.3. Kean, L.: Coefficients for axisymmetric schlieren evaluation. ASD TN 61-56, Wright-Patterson AFB, 1961.

12.4. Oudin, L.; Jeanmaire, M.: La transformation d'Abel. Application à la mésure des masses volumiques dans les sillages. ISL Report no. 21/7o, 197o.

12.5. Kogelschatz, U.; Schneider, W.R.: Quantitative schlieren techniques applied to high current arc investigations. Appl. Opt. 11 (1972), 1822-1832.

12.6. Stricker, J.: Analysis of 3-D phase objects by moiré deflectometry. Appl. Opt. 23 (1984), 3657-3659.

12.7. Noll, R.; Haas, C.R.; Weikl, B.; Herziger, G.: Computer simulation of schlieren images of rotationally symmetric plasma systems: a simple method. Appl. Opt. 25 (1986), 769-774.

12.8. Gorenflo, R.: Numerische Methoden zur Lösung einer Abelschen Differentialgleichung. Report no. IPP/6/19, Institut für Plasmaphysik, Garching, F.R. Germany, 1964.

12.9. Bennett, F.D.; Carter, W.C.; Bergdolt, V.E.: Interferometric analysis of air flow about projectiles in free flight. J. Appl. Phys. 23 (1952), 453-469.

12.1o. Solignac, J.L.: Étude interférométrique de l'écoulement à Mach 5 autour d'une sphère. Rech. Aérosp. no. 125 (1968), 31-39.

12.11. Maruyama, Y.; Iwata, K.; Nagata, R.: Effect of refractive index discontinuity on the reconstruction of the refractive index field. Appl. Opt. 16 (1977), 2o34-2o35.

12.12. Herman, G.T.: Image Reconstruction from Projections. Implementation and Applications. Vol. 32 of Topics in Applied Physics, Springer-Verlag, Berlin, 1979.

12.13. Swindell, W.; Barrett, H.H.: Computerized tomography: Taking sectional X-rays. Physics Today 3o (Dec. 1977), 32-41.

12.14. Santoro, R.J.; Semerjian, H.G.; Emmerman, P.J.; Goulard, R.: Optical tomography for flow field diagnostics. Int. J. Heat Mass Transfer 24 (1981), 1139-115o.

12.15. Matulka, R.D.; Collins, D.J.: Determination of three-dimensional density fields from holographic interferograms. J. Appl. Phys. 42 (1971), 11o9-1119.

12.16. Sweeney, D.W.; Vest, C.M.: Reconstruction of three-dimensional refractive index fields from multi-directional interferometric data. Appl. Opt. 12 (1973), 2649 - 2664.

12.17. Jagota, R.C.; Collins, D.J.: Finite fringe holographic interferometry applied to a right circular cone at angle of attack. J. Appl. Mech. 39 (1972), 897-9o3.

12.18. Kosakoski, R.A.; Collins, D.J.: Application of holographic interferometry to density field determination in transonic corner flow. AIAA J. 12 (1974), 767-77o.

12.19. Witte, A.B.; Mantrom, D.D.: Interferometric technique for measuring mixing of a buoyant plume. AIAA J. 13 (1975), 535-536.

12.2o. Snyder, R.; Hesselink, L.: Optical tomography for flow visualization of the density field around a revolving helicopter rotor blade. Appl. Opt. 23 (1984), 365o-3656.

12.21. Yu, Y.H.; Kittleson, J.K.: Reconstruction of a three-dimensional, transonic rotor flowfield from holographic interferograms. AIAA J. 25 (1987), 3oo-3o5.

12.22. Rowley, P.D.: Quantitative interpretation of three-dimensional weakly refractive phase objects using holographic interferometry. J. Opt. Soc. Am. 59 (1969),1496-1498.

12.23. Junginger, H.G.; van Haeringen, W.: Calculation of three-dimensional refractive index field using phase integrals. Opt. Commun. 5 (1972), 1-4.

12.24. Zien, T.F.; Ragsdale, W.C.; Spring, W.C.: Quantitative determination of three-dimensional density field of a circular cone by holographic interferometry. AIAA Paper 74-636, 1974.

12.25. Vest, C.M.; Prikryl, I.: Tomography by iterative convolution: empirical study and application to interferometry. Appl. Opt. 23 (1984), 2433-244o.

12.26. Belotserkovsky, S.M.: Anwendungsmöglichkeiten und Perspektiven optischer Methoden in der Gasdynamik. Proceed. 8th Int. Congr. High-Speed Photogr., pp. 41o-414, 1968.

12.27. Knauss, H.: Ein Auswerteverfahren für allgemeine dreidimensionale Dichtefelder mit Hilfe der Interferenzmethode. Dissertation, Univ. Stuttgart, 1977.

12.28. Schwarz, G.; Knauss, H.: Quantitative experimental investigation of three-dimensional flow fields around bodies of arbitrary shapes in supersonic flow with optical methods. In [1.5], pp. 737-741, 1982.

## 13.   VISUALIZATION OF LOW-DENSITY FLOWS

The optical visualization methods discussed in chapters 7 to 11 have a lower sensitivity limit in resolving changes of the fluid density. It is somewhat difficult to give general number values for these limitations in sensitivity, because such numbers are dependent on the particular flow conditions. There is, however, a class of fluid flows whose density level is in any case below the range of sensitivity of the optical (refractive index) methods. These flows are, in most cases, governed by supersonic or hypersonic speeds at low average density, sometimes referred to as "low-density gas dynamics". Experimental means for visualizing these flows have been developed already in the early stages of this field. These methods are based on the collision of electrons with the molecules in these flows. The colliding electrons are provided either by an electron beam or by an electric discharge. The collision causes a luminous reaction, with the intensity of the luminous signal depending on the local gas density.

### 13.1  ELECTRON BEAM FLOW VISUALIZATION

A narrow beam of high-energy electrons (as generated, e.g., in a TV tube) is directed through the gas flow under study. Due to inelastic collisions between the fast electrons and the gas molecules, a certain portion of the gas molecules are excited. Subsequently they return to the ground state with emission of a characteristic radiation. If this returning to the ground state is prompt ("spontaneous"), the radiation is emitted more or less at the same position where the gas is excited, i.e. at the position of the electron beam, which appears, therefore, as a column of bright fluorescent light, sometimes called a "fluorescence probe". Under certain conditions, the intensity of this direct radiation is proportional to the local gas density. By moving the electron beam with constant speed in a particular plane through the flow, and by taking a photographic time exposure (with open shutter) while the beam is moving, one obtains a representation to the local distribution of the gas density in this plane. The visible signal (Fig.13.1) is similar to the pattern of a schlieren record, however, its physical information is quite different, because the information on the density distribution is local (one observes the scattered radiation!) and not integrated. There is a closer analogy to the methods of laser induced fluorescence (chapter 5).

The emission of the visible radiation may also occur from an excited metastable state whose lifetime is relatively long. The light emission then takes place after the molecule is swept a certain distance with the flow, i.e. radiation is emitted at a position downstream of the original beam position ("afterglow radiation"). For utilizing this afterglow radiation, which is also appropriate for visualizing density differences in the flow, it is not necessary to move the electron beam as for visualization by the direct radiation, but the intensity of the afterglow is much lower than that of the former.
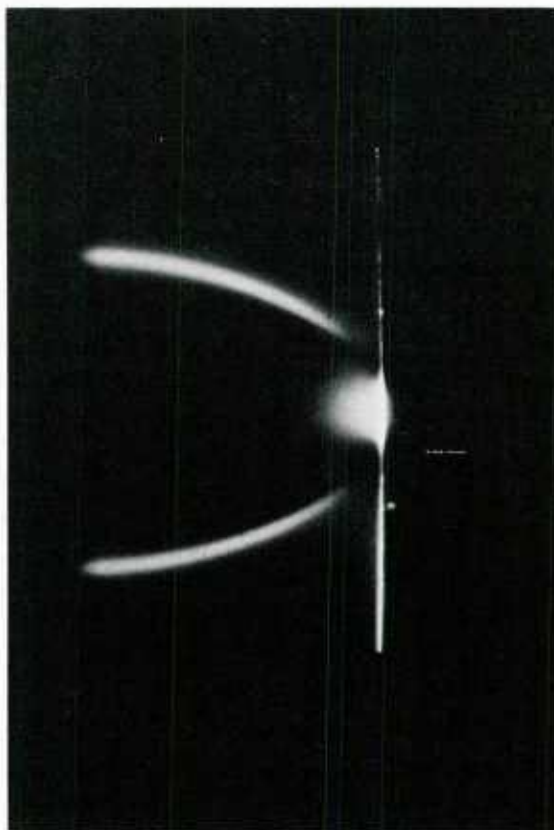
Fig. 13.1: Electron beam visualization of a supersonic nitrogen jet (K.A. Bütefisch, DFVLR Göttingen, F.R. Germany).

Experiments on flow visualization by electron beams have been reported first by Schumacher in 1953 [13.1, 13.2]. It became a frequently used technique in the 196o's when hypersonic flow research had its first boom. Many details of the method have been described by Léwy [13.3]. In addition to qualitative visualization of the flow, the electron beam, in combination with a spectroscopic analysis, may serve for quantitative measurements of flow temperature and density; see, e.g. [13.4]. This application is beyond the scope of the present discussion.

An electron beam of approximately 1 mm in diameter is generated by an electron gun which is operated at voltages of about 2o kV and 1 mA current. For making use of the direct radiation, the beam is either moved mechanically parallel to itself [13.5], or deflected over a certain angular section by means of deflection coils [13.3, 13.6]. When applied to the flow of air or nitrogen, the direct radiation is due to a transition of the $N_2$ molecule resulting in the emission of light at a wavelength of 391,4 nm. The proportionality between the observed radiation intensity and the local gas density is only the result of a simplified analysis, in which a number of real effects have been neglected. The sensitivity of the method with respect to resolving density variations at a reduced level of the average density is about one order of magnitude better than a schlieren system.

The afterglow radiation is less intense than the direct radiation. It can be observed in the flow of nitrogen and noble gases, or mixtures of both, but it disappears almost completely in air due to collisional quenching between excited $N_2$ and nonexited $O_2$ molecules [13.7].

## 13.2  GLOW-DISCHARGE FLOW VISUALIZATION

The electric discharge at several hundred volts applied between two electrodes in a low-density gas produces a plasma column in the gas volume between the two electrodes. The free electrons and ions in the plasma are accellerated by the external electric field, and, upon collisions with the neutral gas molecules, they can excite these molecules, which subsequently emit radiation due to a spontaneous transition into the ground state. This regime of visible radiation is called the positive column. Within a certain range of the gas density, usually at values of about $10^{-3}$ to $10^{-4}$ of the density at normal conditions, the intensity of the positive column is a direct function of the gas density.

The visible radiation emitted from the positive column has been used for visualizing the flow in low-density wind-tunnels, particularly at hypersonic speeds. The potentials of this technique have been reviewed by Fisher and Bharathan [13.8]. The flow in the wind-tunnel test section is passed through the volume between two electrodes to which voltages of 3oo to 1ooo V ac are applied. By a suitable choice of the geometry of the electrodes, the field of the positive column can be varied so as to cover the desired portion of the flow field. In some cases, the test model itself can be made one of the electrodes.

Density changes in the flow, e.g. produced by a shock wave, appear as a change in intensity and sometimes in color of the emitted radiation (Fig. 13.2). The technique has been applied to the visualization of flows of nitrogen [13.9], helium [13.1o], and air [13.11]. The information on the density distribution is not local, as from the electron beam method, but it is to a certain degree integrated, because the visible signal originates from a particular volume in the flow (the positive column).
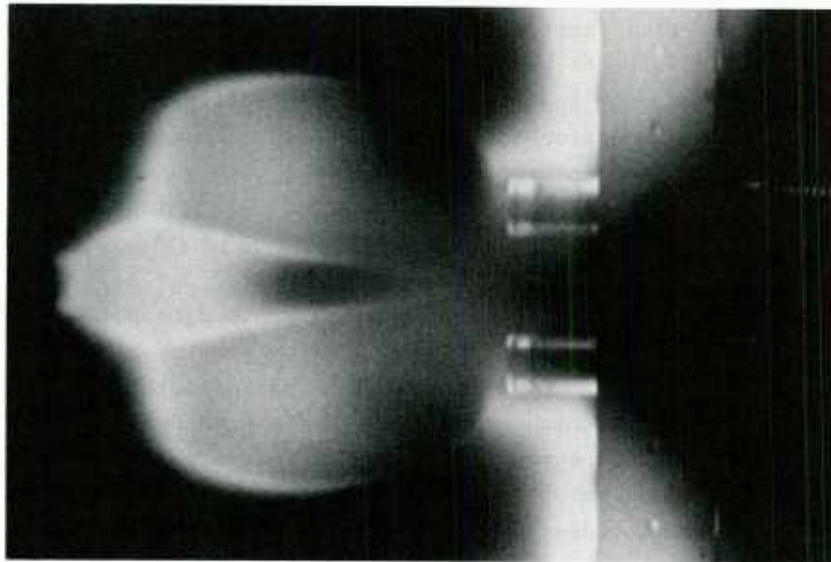


Fig. 13.2:  Glow discharge visualization of the flow interference between two free jets expanding into a vacuum chamber; chamber pressure is 0.18 mbar (G. Koppenwallner, DFVLR Göttingen, F.R. Germany).

REFERENCES

13.1.  Schumacher, B.: Abbildung von Gasströmungen mit Elektronenstrahlen. Ann. Physik 6 (1953), 4o4-42o.

13.2.  Grün, A.E.; Schopper, E.; Schumacher, B.: Electron shadowgraph and afterglow pictures of gas jets at low densities. J. Appl. Phys. 24 (1953), 1527-1528.

13.3.  Lêwy, S.: Visualizations d'écoulements en soufflerie à l'aide d'un faisceau d'électrons. Rech. Aérosp. no. 197o-3, 155-166, 197o.

13.4.  Muntz, E.P.: Measurement of density by analysis of electron beam excited radiation. In: Fluid Dynamics (ed. R.J. Emrich), vol. 18 of Methods of Experimental Physics, pp. 434-455, Academic Press, New York, 1981.

13.5.  Rothe, D.E.: Flow visualization using a traversing electron beam. AIAA J. 3 (1965), 1945-1946.

13.6.  Weinstein, L.M.; Wagner, R.D.; Ocheltree, S.L.: Electron beam flow visualization in hypersonic helium flow. AIAA J. 6 (1968), 1623-1625.

13.7.  Sebacher, D.J.: Flow visualization using an electron beam afterglow in $N_2$ and air. AIAA J. 4 (1966), 1858-1859.

13.8.  Fisher, S.S.; Bharathan, D.: Glow-discharge flow visualization in low-density free jets. J. Spacecraft 1o (1973), 658-662.

13.9.  McCroskey, W.J.; Bogdonoff, S.M.; McDougall, J.G.: An experimental model for the sharp flat plate in rarefied hypersonic flow. AIAA J. 4 (1966), 158o-1587.

13.1o. Horstman, C.C.; Kussoy, M.I.: Hypersonic viscous interaction on slender cones. AIAA J. 6 (1968), 2364-2371.

13.11. San, W.; Ge, Y.: Two methods for low density flow visualization. In [1.5], pp. 421-425, 1982.

## 14.   IMAGE PROCESSING AND THE GENERATION OF DIGITAL FLOW PICTURES

In this context, image processing is the evaluation of a flow picture by means of a computer. For this purpose, the visual record obtained with one of the visualization methods must be digitized. Such a record is a plane distribution of certain visible structures, which can be expressed in form of a data function $D(x,y)$, with $x,y$ being the coordinates in the image plane. The aim of image processing is to identify these structures, to store the values of $D(x,y)$ in the memory of the computer, and then to determine the relevant flow parameters from the data; e.g. the flow velocity field from the visualized time line pattern, or the fluid density distribution from the pattern of interference fringes. The visible data or signal is often superimposed by high-amplitude noise. Computer programs are available which serve to separate the signal from the noise, i.e. to recognize the desired pattern in a noisy environment. It follows that image processing is not a visualization method but a means for making an evaluation procedure independent of the subjective decisions of an operator.

An abundance of literature exists on the general aspects of image processing and on the development of special computer programs. The main purpose of this chapter is to give a number of relevant references which describe the adaption of image processing methods to flow visualization. The essential step for this adaption is the digitization of the visual record. A visualization experiment may result directly in a digital image when an appropriate recording system is applied. In the simplest case, this is a TV camera, whose output is digitized, and which allows for taking a movie picture of a time-dependent flow. Winter et al. [14.1] discuss the use of vidicon-based imaging systems and systems of photodiode arays for flow visualization and the recognition of large-scale structures in the flow. Even in their finest form, i.e. with the maximum of pixels now available per square unit, these systems cannot yet reach the resolution of photographic film (several hundred lines per mm). This limits their application to the recording of fine-scale patterns, e.g. in speckle photography. However, it is expected that the rapid technical development will change the situation in the near future.

When the flow picture is digitized, it can be subjected to a computer analysis in which the specific structures of the pattern are identified, e.g. the interference fringes, time lines, or the images of tracer particles. The recognition and identification usually is based on a spectral analysis of the digital pattern. The coordinates of the structures or of their edges are determined, and the structures may be approximated by geometrical curves, which finally describe the data distribution $D(x,y)$.

The automatic evaluation of interferograms has been described for the various fields

of application of interferometry, not only flow visualization; see, e.g. [14.2 - 14.4]. Kim [14.5] reports on the approximation of the fringe contours by polynomial fits. Once such curves have been determined, it is possible to interpolate the data in between these curves in order to obtain a higher density of the data per square unit and improve the resolution of the data distribution D(x,y). Since optical interferometry is applied often to gas dynamic problems, particular attention has to be paid to the abrupt changes of a fringe contour as caused by a shock wave [14.6]. Among all applications to the flow visualization records, image processing is best developed for interferometry, because interference fringes, particularly those of a laminar flow, make a well defined pattern.

Time lines which can be produced by various visualization techniques (see chapter 4) are contours that can be subjected to an analysis similar to that used for interference fringes. Image processing of hydrogen-bubble time lines recorded with a video camera has been described by Lu and Smith [14.7] and Ongoren et al. [14.8], in both cases with the particular emphasis of identifying particular structures in a turbulent flow. Nagib et al. [14.9] report on the analysis of time lines generated with the smoke-wire technique.

The streaks generated by tracer particles in a photographic time exposure from a pattern that is more difficult to be analyzed by a computer than the aforementioned time lines and interference fringes. Therefore, some systems for the processing of these patterns are interactive, i.e. identification of the streaks is performed by an operator [14.1o]. A number of fully automated systems and procedures have been described, e.g. [14.11 - 14.13]. A major problem in the analysis of the streak pattern is the identification of the flow direction. The final result of the processing is the display of a field of velocity vectors or isovelocity contours. When these processing methods are applied to turbulent flows, it is of interest to identify large scale structures, sometimes called "coherent structures", which are masked by small-scale turbulent noise. These structures, characterized by low wave numbers in a respective Fourier transform, can be recognized when the digitized image is filtered with a 2-D low-pass filter function [14.14]. The pattern recognition thus is made independent of a subjective interpretation.

Digital flow pictures can be generated easily as the result of a computation or a survey of the flow field with a measuring probe.These pictures can be compared with the patterns obtained from a flow visualization experiment, and conclusions my be drawn, e.g., on the quality of a computation. Flow visualization by means of computer graphics, however, is beyond the definition of the term "flow visualization" in this review.

## REFERENCES

14.1.   Winter, M; Lamm, J.K.; Long, M.B.: Techniques of high-speed digital imaging of gas concentrations in turbulent flows. Exp. Fluids 5 (1987), 177-183.

14.2.   Boxman, R.L.; Sloan, M.L.: Scanning technique for obtaining linear fringe shift readout from a high resolution interferometer. Appl. Opt. 17 (1978), 2794-2797.

14.3.   Robinson, D.W.: Automatic fringe analysis with a computer image-processing system. Appl. Opt. 22 (1983), 2169-2176.

14.4.   Boyd, R.D.; Miller, D.J.; Ghiglia, D.C.: Automated data reduction for optical interferometric data. In [1.6], pp. 14o-144, 1985.

14.5.   Kim, C.-J.: Polynomial fit of interferograms. Appl. Opt. 21 (1982), 4521-4525.

14.6.   Ben-Dor, G.; Whitten, B.T.; Glass, I.I.: Evaluation of perfect and imperfect-gas interferograms by computer. Int. J. Heat Fluid Flow 1 (1979), 77-91.

14.7.   Lu, L.J.; Smith, C.R.: Image processing of hydrogen bubble flow visualization for determination of turbulence statistics and bursting characteristics. Exp. Fluids 3 (1985), 349-356.

14.8.   Ongoren, A.; Chen, J.; Rockwell, D.: Multiple time-surface characterization of time-dependent, three-dimensional flows. Exp. Fluids 5 (1987), 418-422.

14.9.   Nagib, H.M.; Corke, T.C.; Way, J.L.; Helland, K.N.: Computer analysis of flow vi-
        sualization records obtained by the smoke-wire technique. Paper presented at the
        Dynamics Flow Conference, Baltimore, MD, 1978.

14.1o.  Utami, T.; Ueno, T.: Visualization and picture processing of turbulent flow. Exp.
        Fluids 2 (1984), 25-32.

14.11.  Kobayashi, T.; Ishihara, T.; Sasaki, N.: Automatic analysis of photographs of tra-
        ce particles by microcomputer-system. In [1.6], pp. 231-235, 1985.

14.12.  Balint, J.L.; Ayrault, M.; Schon, J.P.: Quantitative investigation of the velocity
        and concentration fields of turbulent flows combining visualization and image pro-
        cessing. In [1.6], pp. 254-258, 1985.

14.13.  Racca, R.G.; Dewey, J.M.: A method for automatic particle tracking in a three-di-
        mensional flow field. Exp. Fluids 5 (1987).

14.14.  Corke, T.C.: Digital image filtering in visualized boundary layers. AIAA J. 22
        (1984), 1124-1131.

| AGARDograph No.302<br>Advisory Group for Aerospace Research and Development, NATO<br>TECHNIQUES OF FLOW VISUALIZATION<br>by W.Merzkirch and edited by K.Gersten<br>Published December 1987<br>98 pages<br><br>The techniques of flow visualization and their application in wind tunnels, water channels, and experiments related to propulsion research are reviewed. These techniques can be classified roughly into three major groups: Surface flow visualization, scattering from flow tracers, and density sensitive flow visualization. The progress in laser optics and the wide-spread use of computers has led to the development of novel techniques and evaluation<br><br>P.T.O. | AGARD-AG-302<br><br>Flow visualization<br>Wind tunnels<br>Water flow<br>Propulsion<br>Evaluation | AGARDograph No.302<br>Advisory Group for Aerospace Research and Development, NATO<br>TECHNIQUES OF FLOW VISUALIZATION<br>by W.Merzkirch and edited by K.Gersten<br>Published December 1987<br>98 pages<br><br>The techniques of flow visualization and their application in wind tunnels, water channels, and experiments related to propulsion research are reviewed. These techniques can be classified roughly into three major groups: Surface flow visualization, scattering from flow tracers, and density sensitive flow visualization. The progress in laser optics and the wide-spread use of computers has led to the development of novel techniques and evaluation<br><br>P.T.O. | AGARD-AG-302<br><br>Flow visualization<br>Wind tunnels<br>Water flow<br>Propulsion<br>Evaluation |
|---|---|---|---|
| AGARDograph No.302<br>Advisory Group for Aerospace Research and Development, NATO<br>TECHNIQUES OF FLOW VISUALIZATION<br>by W.Merzkirch and edited by K.Gersten<br>Published December 1987<br>98 pages<br><br>The techniques of flow visualization and their application in wind tunnels, water channels, and experiments related to propulsion research are reviewed. These techniques can be classified roughly into three major groups: Surface flow visualization, scattering from flow tracers, and density sensitive flow visualization. The progress in laser optics and the wide-spread use of computers has led to the development of novel techniques and evaluation<br><br>P.T.O. | AGARD-AG-302<br><br>Flow visualization<br>Wind tunnels<br>Water flow<br>Propulsion<br>Evaluation | AGARDograph No.302<br>Advisory Group for Aerospace Research and Development, NATO<br>TECHNIQUES OF FLOW VISUALIZATION<br>by W.Merzkirch and edited by K.Gersten<br>Published December 1987<br>98 pages<br><br>The techniques of flow visualization and their application in wind tunnels, water channels, and experiments related to propulsion research are reviewed. These techniques can be classified roughly into three major groups: Surface flow visualization, scattering from flow tracers, and density sensitive flow visualization. The progress in laser optics and the wide-spread use of computers has led to the development of novel techniques and evaluation<br><br>P.T.O. | AGARD-AG-302<br><br>Flow visualization<br>Wind tunnels<br>Water flow<br>Propulsion<br>Evaluation |

procedures, which are included in the review; e.g. laser-induced fluorescence, speckle photography, image processing, and optical tomography. Emphasis is given to the discussion of the physical background of the methods. Information on technical details is provided by means of a number of sample photographs and by respective references.

This AGARDograph has been produced at the request of the Fluid Dynamics Panel of AGARD.

ISBN 92-835-0438-0

AGARD

NATO ✈ OTAN

7 rue Ancelle · 92200 NEUILLY-SUR-SEINE

FRANCE

Telephone (1)47.38.57.00 · Telex 610 176

**DISTRIBUTION OF UNCLASSIFIED
AGARD PUBLICATIONS**

AGARD does NOT hold stocks of AGARD publications at the above address for general distribution. Initial distribution of AGARD publications is made to AGARD Member Nations through the following National Distribution Centres.Further copies are sometimes available from these Centres, but if not may be purchased in Microfiche or Photocopy form from the Purchase Agencies listed below.

### NATIONAL DISTRIBUTION CENTRES

**BELGIUM**
Coordonnateur AGARD — VSL
Etat-Major de la Force Aérienne
Quartier Reine Elisabeth
Rue d'Evere, 1140 Bruxelles

**CANADA**
Defence Scientific Information S~
Dept of Natic
Ottawa, Onta

**DENMARK**
Danish Defen
Ved Idraetspa
2100 Copenh

**FRANCE**
O.N.E.R.A. (D
29 Avenue de
92320 Châtill

**GERMANY**
Fachinformatic
Physik, Mather
Kernforschung
D-7514 Eggen:

**GREECE**
Hellenic Air Fo
Research and D
Holargos, Ather

**ICELAND**
Director of Aviation
c/o Flugrad
Reyjavik

**ITALY**
Aeronautica Militare
Ufficio del Delegato Nazionale all'AGARD
3 Piazzale Adenauer
00144 Roma/EUR

**LUXEMBOURG**

**UNITED KINGDOM**
Defence Research Information Centre
Kentigern House
65 Brown Street
Glasgow G2 8EX

**UNITED STATES**
National Aeronautics and Space Administration (NASA)
Langley Research Center
M/S 180
Hampton, Virginia 23665

THE UNITED STATES NATIONAL DISTRIBUTION CENTRE (NASA) DOES NOT HOLD
STOCKS OF AGARD PUBLICATIONS, AND APPLICATIONS FOR COPIES SHOULD BE MADE
DIRECT TO THE NATIONAL TECHNICAL INFORMATION SERVICE (NTIS) AT THE ADDRESS BELOW.

### PURCHASE AGENCIES

National Technical
Information Service (NTIS)
5285 Port Royal Road
Springfield
Virginia 22161, USA

ESA/Information Retrieval Service
European Space Agency
10, rue Mario Nikis
75015 Paris, France

The British Library
Document Supply Division
Boston Spa, Wetherby
West Yorkshire LS23 7BQ
England

Requests for microfiche or photocopies of AGARD documents should include the AGARD serial number, title, author or editor, and publication date. Requests to NTIS should include the NASA accession report number. Full bibliographical references and abstracts of AGARD publications are given in the following journals:

Scientific and Technical Aerospace Reports (STAR)
published by NASA Scientific and Technical
Information Branch
NASA Headquarters (NIT-40)
Washington D.C. 20546, USA

Government Reports Announcements (GRA)
published by the National Technical
Information Services, Springfield
Virginia 22161, USA

SPS

*Printed by Specialised Printing Services Limited
40 Chigwell Lane, Loughton, Essex IG10 3TZ*

ISBN 92-835-0438-0